

THERMODYNAMICS OF IONIC LIQUID SOLVENTS IN GAS PURIFICATION
AND EXFOLIATION MECHANISMS: MOLECULAR DYNAMICS SIMULATION AND
MONTE CARLO CALCULATIONS

by

ASGHAR ABEDINI

C. HEATH TURNER, COMMITTEE CHAIR

YUPING BAO, COMMITTEE CO-CHAIR

JASON E. BARA

VINU UNNIKRISHNAN

EVAN K. WUJCIK

A DISSERTATION

Submitted in partial fulfillment of the requirements
for the degree of Doctor of Philosophy
in the Department of Chemical and Biological Engineering
in the Graduate School of
The University of Alabama

TUSCALOOSA, ALABAMA

2018

Copyright Asghar Abedini 2018
ALL RIGHTS RESERVED

ABSTRACT

Demand for green sources of energy is increasing due to the critical need to decrease greenhouse gas emissions. This research involved different approaches for reducing CO₂ emission to the atmosphere. In the first study, the exfoliation of bismuth telluride (Bi₂Te₃) as a well-know thermoelectric (TE) material was investigated. In the literature, it has been experimentally and computationally proven that producing a thinner layer of Bi₂Te₃ increases the “figure of merit” by reducing the thermal conductivity and enhancing the electrical conductivity.

A liquid-phase exfoliation technique is one of the potential approaches to exfoliate Bi₂Te₃. In my simulation work, different types of imidazolium-based ionic liquids (ILs) were screened to find the most efficient exfoliant, by first considering the value of the solid surface energy and surface tension of the applied liquids. We found that [Tf₂N⁻]-based ionic liquids are relatively effective at enhancing the exfoliation, and this performance can be correlated to the unique molecular-level solvation structures developed at the Bi₂Te₃ surfaces.

In the second study, I modeled CO₂ separation during typical pre-combustion and post-combustion condition using a novel IL + polymer membrane material. This work was inspired by recent experimental findings from the Bara group at UA. The new class of materials was generated by adding ionic liquid molecules to the backbone of polymers while using (pyromellitic dianhydride) PMDA as an organic ligand. For the first time, these polymers, “ionic polyimides” (i-IPs), were computationally investigated as a potential membrane for CO₂ separation.

The presence of the IL significantly displaces the CO₂ molecules from the ligand nitrogen sites in the neat i-IP to the imidazolium rings in the i-IP + IL composite. These molecular details can provide critical information for the experimental design of highly selective i-IP materials, as well as provide additional guidance for the interpretation of simulated adsorption systems. It is found that the 50% IL addition can increase CO₂/CH₄ selectivity by 16% in [BF₄⁻]-based and by 36% in [PF₆⁻]-based structures. While the [BF₄⁻]-based system shows higher CO₂/CH₄ selectivity, the [Tf₂N⁻]-based system shows higher CO₂/N₂ gas separation performance. These findings are exemplified by high gas solubility of [PF₆⁻]-based structures, which also compensate to a correlated larger theoretical surface area.

DEDICATION

This dissertation is dedicated to everyone who guided me, helped me, and encouraged me throughout my PhD. In particular, I am the most grateful to my advisor, Dr. C. Heath Turner, my committee members, my group members, and our group alumnus.

LIST OF ABBREVIATIONS AND SYMBOLS

Bi_2Te_3	Bismuth telluride
TE	Thermoelectric
ILs	Ionic liquids
PILs	Polymerized ionic liquids
i-IP	Ionic polyimide
$[\text{C}_4\text{mim}^+]$	1-n-butyl-3-methylimidazolium
$[\text{Tf}_2\text{N}^-]$	bis(trifluoromethylsulfonyl)imide
$[\text{BF}_4^-]$	tetrafluoroborate
$[\text{PF}_6^-]$	hexafluorophosphate
T_d	Decomposition temperature
T_m	Melting temperature
$[\text{C}_2\text{mim}^+]$	1-ethyl-3-methylimidazolium
zT	Thermoelectric figure of merit
FFV	Fractional free volume
MD	Molecular dynamics
GCMC	Grand canonical Monte Carlo
C_H	Head Carbon
C_T	Tail Carbon
DFT	Density functional theory
MC	Monte Carlo

NPT	isothermal-isobaric ensemble
SMD	steered molecular dynamics
SPME	smooth particle mesh Ewald sum
PMF	potential of mean force
NVT	Canonical ensemble
F_{SMD}	force
NMP	N-methyl-2-pyrrolidone
2D	two-dimensional
h-BN	hexagonal boron nitride
ABF-MD	adaptive bias force-molecular dynamics
UFF	United force field
MEA	monoethanolamine
MOFs	metal organic frameworks
PIMs	polymers of intrinsic microporosity
COF	covalent organic framework
RDFs	radial distribution functions
SILMs	Supported ionic liquid membranes
AMPs	amorphous microporous polymers
PILs	poly(ionic liquids)s
PMDA	pyromellitic dianhydride
PSD	pore size distribution
6-FDA	hexafluoroisopropylidene-diphthalic anhydride
ρ	Density
α	Seebeck coefficient

σ	electrical conductivity
κ_e	Electronic contributions to the total thermal conductivity
κ_L	lattice contributions to the total thermal conductivity
v	velocity
K	stiffness of the spring

ACKNOWLEDGMENTS

I would like to thank my advisor, C. Heath Turner, for all of his help and guidance in my research during My PhD including all technical and non-technical aspects of study, teaching, and research. I truly appreciate his quick and comprehensive feedback on my writings and reviewing manuscripts. I enjoyed my research experience as a PhD student in Dr. Turner's lab.

I would like to acknowledge my dissertation committee members: Yuping Bao, Jason E. Bara, Vinu Unnikrishnan, and Evan K. Wujcik for their valuable technical questions and suggestions. I wish to thank our research group members: Zhongtao Zhang, Thomas Ludwig, Ryan Hamilton, Ellis Crabtree, Henry Atkinson, and Jingjing Ji. I was so happy to be part of a diverse research team with: Brian Flowers, John W. Whitley, Grayson Dennis, Katie O'Harra, W. Jeffrey Horne, and Jason M. Tedstone, which was a memorable experience. I need to thank graduate students: Shelby Brooks, Brandon Boyd, Seungjo Park, Jennifer Sherwood, Ursula Triantafillu, and Alexandra Wrist in Chemical and Biological engineering. I would like to thank Dr. Ken Hinton for all of his help and support on my language mentoring and valuable guidance, which was a memorable experience in Tuscaloosa.

I certainly thank the faculty, staff, and graduate students of the Department of Chemical and Biological Engineering, at the University of Alabama, for their support and generosity. The financial support from The University of Alabama Research Grants, National Science Foundation, and DOE was appreciated. I would like to thank Alabama Supercomputer Center for allowing me to use their facilities during my research.

Finally, I would like to thank my parents, sisters and my brother for their encouragement and support during my education.

CONTENTS

ABSTRACT.....	ii
DEDICATION.....	iv
LIST OF ABBREVIATIONS AND SYMBOLS	v
ACKNOWLEDGMENTS	viii
LIST OF TABLES.....	xiii
LIST OF FIGURES	xiv
1. INTRODUCTION	1
1.1 Motivation.....	1
1.2 Objectives	5
1.3 Overview of computational methods.....	6
1.3.1 Density functional theory.....	7
1.3.2 Molecular dynamics and Monte Carlo simulations	8
1.4 Overview of our work.....	10
References.....	12
2. MOLECULAR DYNAMICS SIMULATION OF BISMUTH TELLURIDE EXFOLIATION MECHANISMS IN DIFFERENT IONIC LIQUID SOLVENTS	15
2.1 Introduction.....	15
2.2 Simulation Methods.....	18
2.3 Results and Discussion	19
2.3.1 Steered Molecular Dynamics Simulations.....	20

2.3.2 Potential of Mean Force.....	23
2.4 Density Profile	26
2.5 Molecular Structure	30
2.6 Conclusions.....	36
Acknowledgements.....	37
Supporting Information.....	37
Appendix A, Supporting Information for Chapter 2.....	38
References.....	48
3. MOLECULAR SIMULATION OF GAS SOLUBILITY CAPACITY IN IONIC POLYIMIDES AND COMPOSITES WITH IONIC LIQUIDS	53
3.1 Introduction.....	53
3.2 Simulation Details.....	57
3.3 Results and Discussion	64
3.3.1.1 Structural Optimization.....	64
3.4 Structural Analysis.....	67
3.5 Gas Solubility.....	70
3.6 Analysis of Adsorbate Interactions.....	72
3.7 Conclusion	77
Acknowledgements.....	78
Supporting Information.....	78
Appendix B, Supporting Information for Chapter 3.....	79
References.....	83
4. MOLECULAR ANALYSIS OF SELECTIVE GAS ADSORPTION WITHIN COMPOSITES OF IONIC POLYIMIDES AND IONIC LIQUIDS AS GAS SEPARATION MEMBRANES	87
4.1 Introduction.....	87

4.2 Simulation Details.....	91
4.3 Results and Discussion	97
4.3.1 Gas Solubility.....	97
4.3.2 Gas Selectivity	98
4.3.3 Structural Analysis.....	101
4.3.4 Adsorbate/Adsorbent Interaction Analysis	107
4.4 Conclusion	111
Acknowledgements.....	112
Supporting Information.....	112
Appendix C, Supporting Information for Chapter 4.....	113
References.....	122
5. SUMMARY	128
5.1 Bismuth telluride exfoliation	128
5.2 CO ₂ capture.....	129
6. FUTURE WORK.....	131
References.....	136

LIST OF TABLES

Table A2.1. Physical properties of ionic liquids: density (ρ) at corresponding temperature indicated in parenthesis, onset temperature of decomposition (T_d), melting temperature (T_m), and surface tension.....	38
Table 3.1. Summary of different i-IP systems simulated, with densities corresponding to conditions of 1 bar and 294 K.....	62
Table B3.2. Henry's law constant for different IL and polymer structures (mol/(L·atm)).	81
Table B3.3. Solubility values for CO ₂ and CH ₄ from Figure 3.6.....	82
Table 4.1. Summary of different i-IP systems (a → h) simulated.	94
Table 4.2. Density (g/cm ³) of neat i-IP and composite of i-IP + IL samples at 1 bar and 294 K. The columns #1 to #5 indicate different independent replicates.	95
Table C4.3 Solubility (g/L) and selectivity for more comparison.	117
Table C4.4 Solubility (mg/g) and selectivity for more comparison.	118

LIST OF FIGURES

Figure 1.1. a) The polymer structure after relaxation..	10
Figure 2.1. Illustration of the exfoliation mechanisms simulated for the bilayer Bi_2Te_3 system: (a) peeling, (b) pulling, and (c) shearing.	18
Figure 2.2. Maximum applied force for exfoliation of Bi_2Te_3 via the a) pulling, b) shearing, and c) peeling mechanisms.	23
Figure 2.3. PMF results for Bi_2Te_3 exfoliation at 550 K for: (a) pulling and (b) peeling process.....	26
Figure 2.4. Cross-sectional analysis of a $[\text{C}_4\text{mim}^+][\text{Tf}_2\text{N}^-]$ solvent at 450 K for different COM distances between Bi_2Te_3 layers: (a) cross-sectional simulation view, (b) $[\text{C}_4\text{mim}^+]$ and $[\text{Tf}_2\text{N}^-]$ concentrations, and (c) $[\text{C}_4\text{mim}^+][\text{Tf}_2\text{N}^-]$ charge distribution.	29
Figure 2.5. Normalized number density of long chain terminal carbon (C_2 , C_4) in different ILs at 450 K: (a) $[\text{C}_4\text{mim}^+]$ and (b) $[\text{C}_2\text{mim}^+]$	30
Figure 2.6. Normalized number density of short chain (C_M) carbon in different ILs at 450 K: (a) $[\text{C}_4\text{mim}^+]$ and (b) $[\text{C}_2\text{mim}^+]$	31
Figure 2.7. Normalized number density of imidazolium ring in different ILs at 450 K.....	31
Figure 2.8. Ring angle distribution for $[\text{C}_4\text{mim}^+]$ -based ILs..	33
Figure 2.9. Normalized number density of anions in different ILs at 450 K.....	34
Figure 2.10. Charge distribution of ILs solvent at 450 K: (a,b) $[\text{C}_4\text{mim}^+]$ (c,d) $[\text{C}_2\text{mim}^+]$	35
Figure A2.11. Chemical structure of 1-butyl-3-methylimidazolium $[\text{C}_4\text{mim}^+]$, 1-ethyl-3-methylimidazolium $[\text{C}_2\text{mim}^+]$, bis(trifluoromethylsulfonyl)imide $[\text{Tf}_2\text{N}^-]$, hexafluorophosphate $[\text{PF}_6^-]$, bromide $[\text{Br}^-]$, and chloride $[\text{Cl}^-]$ ions (N = navy, O = red, S = yellow, C = grey, F = light blue, P = orange, Br = dark red, Cl = green, and hydrogen atoms are omitted for clarity).....	38
Figure A2.12. Force versus time for Bi_2Te_3 exfoliation in $[\text{C}_4\text{mim}^+][\text{Tf}_2\text{N}^-]$ solution at 550 K via the pulling process.....	39
Figure A2.13. Force versus time for Bi_2Te_3 exfoliation in a $[\text{C}_4\text{mim}^+][\text{Tf}_2\text{N}^-]$ solvent at 550 K via the pulling mechanism..	40

Figure A2.14. Force versus distance for the Bi ₂ Te ₃ pulling mechanism in a [C ₄ mim ⁺][Tf ₂ N ⁻] solvent at 450 K.	41
Figure A2.15. Force versus distance for the Bi ₂ Te ₃ peeling mechanism in a [C ₄ mim ⁺][Tf ₂ N ⁻] solvent at 450 K.	42
Figure A2.16. Force versus distance for the Bi ₂ Te ₃ peeling mechanism in a [C ₄ mim ⁺][Cl ⁻] solvent at 450 K.	43
Figure A2.17. Force versus separation distance for the peeling mechanism in four different [C ₄ mim ⁺]-based solvents at 450 K.	43
Figure A2.18. Normalized number density for selected atoms of: a) [C ₄ mim ⁺][Tf ₂ N ⁻], b) [C ₄ mim ⁺][PF ₆ ⁻], c) [C ₄ mim ⁺][Br ⁻], d) [C ₄ mim ⁺][Cl ⁻].	44
Figure A2.19. Calculated densities of ILs versus experiments at: (a) 304 K for [C ₄ mim ⁺][Tf ₂ N ⁻], (b) 298 K for [C ₄ mim ⁺][Cl ⁻], (c) 304 K for [C ₂ mim ⁺][Tf ₂ N ⁻], and (d) 353 K for [C ₂ mim ⁺][Cl ⁻]. The dashed lines represent the experimental data.	45
Figure A2.20. Calculated density profiles of different ILs at the Bi ₂ Te ₃ interface vs.	46
Figure A2.21. Normalized number density of C ₂ carbon in [C ₄ mim ⁺] structure at 450 K.	47
Figure 3.1. Representative overview of the simulation models: a) i-IP monomer, atoms are colored according to their type (N = navy, O = red, C = grey, and H = white).	58
Figure 3.2. CO ₂ solubility during densification and relaxation for: a) 55 monomers; b) 110 monomers; c) 200 monomers; and d) 200 monomers in 200 [C ₄ mim][Tf ₂ N].	66
Figure 3.3. CO ₂ solubility versus surface area for: a) 55 monomers; b) 110 monomers; c) 200 monomers; and d) 200 monomers in 200 [C ₄ mim ⁺][Tf ₂ N ⁻].	68
Figure 3.4. CO ₂ solubility versus FFV for: a) 55 monomers; b) 110 monomers; c) 200 monomers; and d) 200 monomers in 200 [C ₄ mim][Tf ₂ N].	69
Figure 3.5. Pore size distribution of initial structures (solid lines) and optimized, compressed structure (dashed lines) at 294 K. Colors represent different polymer systems.	70
Figure 3.6. Adsorption isotherms at 294 K of: a) CO ₂ , b) CH ₄ (gas solubility values are provided in Table B3.3).	71
Figure 3.7. Radial distribution function between the carbon atom of CO ₂ and the i-IP sites: a) N1; b) N2; c) N3; d) N4; e) N5; and f) N6 (see Figure 3.1 for site labels).	75
Figure 3.8. Radial distribution functions of the carbon atom of CH ₄ with the i-IP sites: a) N1; b) N2; c) N3; d) N4; e) N5; and f) N6 (see Figure 3.1 for site labels).	76
Figure 3.9. Radial distribution function of the oxygen atoms of the [Tf ₂ N ⁻] anions with the carbon atoms of: a) CO ₂ ; and b) CH ₄ (see Figure 3.1 for site labels).	77

Figure B3.10. Radial distribution function of i-IP monomers for different box sizes and 10 ns of runtime at 550 K and 1 bar: a) head-head, b) head-tail c) all box sizes of 50 ns runtime.....	80
Figure B3.11. Illustration of: a) i-IP monomer; b) [Tf ₂ N ⁻] molecules (2 per i-IP monomer); c) [C ₄ mim ⁺]; and d) NMP structures. Atoms are colored according to their type (N = navy, O = red, S = yellow, C = grey, H = white, and F = light blue).....	80
Figure B3.12. Gas solubility comparison for structure preparing without NMP (hollow symbols) and with NMP (filled symbols) in polymerization.	81
Figure 4.1. Representative monomer structure of a neat i-IP.	92
Figure 4.2. Calculated pure gas solubility at 294 K and 1 bar within neat i-IP and i-IP+IL composites.....	98
Figure 4.3. Predicted CO ₂ /CH ₄ selectivity for: a) [Tf ₂ N ⁻], b) [BF ₄ ⁻], and c) [PF ₆ ⁻] at 294 K and 1 bar.....	100
Figure 4.4. Predicted CO ₂ /N ₂ selectivity for: a) [Tf ₂ N ⁻], b) [BF ₄ ⁻], and c) [PF ₆ ⁻] at 294 K and 1 bar.....	101
Figure 4.5. Pore size distribution for: a) neat i-IP, b) composite structure of i-IP + 10% IL, c) i-IP + 30% IL, and d) i-IP + 50% IL at 294 K and 1 bar (specifically, sample #2 of Table 2 after CO ₂ saturation).....	105
Figure 4.6. Comparison of: a) the surface area and b) the FFV at 294 K and 1 bar for CO ₂ saturated structures.....	105
Figure 4.7. Comparison of the average: a) surface area, b) solubility, and c) FFV change before and after the MD/GCMC cycles involving CO ₂ adsorption.....	106
Figure 4.8. Probe diameter size sensitivity analysis for the CO ₂ saturated structures: a) 1.0 Å, b) 2.0 Å, c) 3.0 Å, and d) 4.0 Å.	107
Figure 4.9. Radial distribution functions of gas interactions with different anion species: a and b) carbon site of CO ₂ ; c and d) nitrogen sites of N ₂ ; e and f) carbon site of CH ₄	109
Figure C4.10. CO ₂ solubility calculation at 294 K and 1 bar for [Tf ₂ N ⁻]-based structure.	113
Figure C4.11. CO ₂ solubility calculation at 294 K and 1 bar for [BF ₄ ⁻]-based structure.	114
Figure C4.12. CO ₂ solubility calculation at 294 K and 1 bar for [PF ₆ ⁻]-based structure.....	115
Figure C4.13. 3D printed structure of the polymer in a) cylindrical and b) cube shape to better illustrate the polymer molecules chain and crated porous area.	116

Figure C4.14. Carbon site of CO ₂ interaction with anions. (B in BF ₄ , P in PF ₆ and O in Tf ₂ N).	119
Figure C4.15. Nitrogen site of N ₂ gas interactions with anions. (B in BF ₄ , P in PF ₆ and O in Tf ₂ N).	120
Figure C4.16. Carbon site of CH ₄ in interaction with anions. (B in BF ₄ , P in PF ₆ and O in Tf ₂ N).	121
Figure 6.1. a) i-IP structure with PMDA ligand. b) PMDA molecule.	134
Figure 6.2. a) i-IP structure with 6-FDA ligand. b) the alternative i-IP structure with 6-FDA and c) the 6-FDA structure.	135

1. INTRODUCTION

1.1 Motivation

Due to industrial advancement and increasing population, the global energy demand is increasing. A large portion of the global energy demand is met by fossil fuels, such as natural gas, coal, oil, etc. Hydrocarbon-based fuel sources are anticipated to play a significant role in the global economy due to their low cost and availability. However, fossil fuels are known to be direct sources of greenhouse gas emissions. In this work, two different technologies were investigated that have the potential for reducing, directly and indirectly, greenhouse gas emissions. One is the direct conversion of heat to electricity using thermoelectric (TE) materials. By converting thermal energy to electricity by using TE devices, the demand for fossil based energy can potentially be reduced.¹ These TE devices can also be used as a heat pump to provide active cooling and heating under current flow without moving parts.² Second is the direct reduction of CO₂ emission through pre-combustion and post-combustion CO₂ capture using novel membrane materials.

Research in TE devices has rapidly increased in the past two decades.³ Exploring alternative sources of energy has been one of the main themes of the current century. Effectively converting waste heat to electricity could play a valuable role in a global sustainable energy solution.³ The key challenge to increase the efficiency of TE devices is to increase the “figure of merit” $zT = \alpha^2 \sigma T / (\kappa_e + \kappa_L)$, where α , σ , T , κ_e , and κ_L are the Seebeck coefficient, electrical conductivity, absolute temperature, and electronic and lattice contributions to the total thermal

conductivity, respectively. In last two decades, tremendous exploratory efforts have been made to develop modern theories and apply advanced synthesis techniques.³ A high “figure of merit” was reported in the context of performance optimization of TE materials. To increase the figure of merit, a low thermal conductivity in combination with a high electrical conductivity is desired. Low cost of production, capability of producing nanostructured TE materials (e.g. 2D TE materials), and compatibility with the scale-up manufacture makes chalcogenide materials promising TE devices. In this study, the exfoliation of thermoelectric materials using liquid-phase exfoliation was evaluated to produce 2D nanolayers of Bi₂Te₃. Producing nanolayers as thin as 1 nm of these types of TE materials increases the figure of merit from $zT = 1.14$ to 3 or 4 at room temperature by decreasing the lattice thermal conductivity and increasing the electric conductivity.

The most effective TE materials at low temperature (300–500 K) are the alloys of (Bi,Sb)₂(Te,Se)₃. A high figure of merit of ~ 1.2-1.4 for Bi₂Te₃-based alloys was reported.^{3,4} Medium-temperature (500-900 K) TE materials, specifically lead salts, are the largest family of TE materials for power generation. These types of alloys include Pb(Te,Se,S), PbTe-AgSbTe₂, and GeTe-AgSbTe₂. A figure of merit of ~1.7 to ~2.2 was reported for PbTe alloys in the medium-temperature range. For high-temperature (>900 K) TE materials, a figure of merit of > 1.0 was reported for SiGe, La₃Te₄, Yb₁₄MnSb₁₁, ZrCoSb based alloys.³ The high operation temperature of these TE materials compensates their low figure of merit in comparison to medium-temperature alloys. Other advantages of these high-temperature TE materials are related to their mechanical robustness and thermal stability, which are important for commercial applications.

Chalcogenides are one of the typical TE materials that have received attention, due to their applications over a wide range of temperatures.⁵ Large interface density of chalcogenide based materials in nanostructure form of TE devices results in low thermal conductivity, which increases the figure of merit. Close electronegativity of the chalcogenide materials from sulfur to tellurium and producing a large variety of TE materials by combining elements to the chalcogenides result in semiconductors with wide ranges of energy gap in various temperatures.

In the second study, new membrane materials were evaluated for CO₂ capture. Though natural gas (NG) has less environmental impact than coal, its natural composition contains CO₂, H₂S, CO, and mercaptans, which are considered great ecological threats to the atmosphere. These contaminants cause problems in natural gas processing and transportation; therefore, it is desirable to remove acid gases before use in processes. The presence of these acid gases in NG reduces the heating value, increases the maintenance cost of transportation materials and pipelines, and decreases the process performance. Therefore, eliminating these acid gases during pre-combustion CO₂ capturing up to an acceptable specification (2-3 mol%) is mandatory prior to transporting NG. Corrosivity and toxicity of acid gasses create a vast challenge for transportation pipelines, and their high freezing point reduces plant operation efficiency by reducing heat exchanger surface area and plugging in lines. Many acid gas removal technologies exist such as absorption processes (chemical and physical sorption), adsorption processes within solid porous materials, and membrane separations. Selecting an appropriate technology depends on: (I) contaminant concentration in the feed, (II) the degree of purification required in the outlet gas, (III) hydrocarbon composition in the feed gas, and (IV) the flow rate of the feed gas.⁶

Traditionally, the majority of pre-combustion and post-combustion CO₂ capturing technologies are amine based.⁷ However, amine based solvents have some disadvantages that

have led research groups to investigate alternatives, such as solvent loss during adsorption and recovery, corrosivity, and high heat of solution. In contrast, there are other potential processes investigated to eliminate these disadvantages. Ionic liquid (IL) solvents have beneficial physicochemical properties such as: low volatility, high thermal stability, high CO₂ solubility, and high tunability by pairing different cations and anions. These properties make these solvents a potential absorbent in CO₂ removal applications.^{6,8-15} ILs are molten salts at low temperatures, non-volatile, and air and water stable and can be compatible solvents for a wide variety of organic, inorganic, and polymeric materials.^{6,13} However, ILs also have some disadvantages such as high viscosity, low porosity, and hygroscopic nature. Thus, pairing the ILs and other solvents with solid structures for gas adsorption applications may provide a better composite for effective CO₂ capture due to combining of high CO₂ solubility and selectivity in ILs and porosity of solid structures.

Adsorption is another potential technology for gas separation and storage. Several different adsorbents such as activated carbon,¹⁶ zeolites,¹⁷ metal organic frameworks (MOFs),¹⁸ and covalent organic frameworks (COFs)¹⁹ have been widely studied for CO₂ adsorption. These materials provide a high capacity for gas adsorption while suffering from limitations in selectivity, cost, or stability. The primary advantage of physical adsorption processes over amine-based solvents is the lower energy demand for solvent recovery due to CO₂ adsorption accomplished through physical interactions instead of chemical reactions.^{20,21}

To commercialize new separation materials, their physicochemical properties must be thoroughly understood. Properties and thermodynamic models, molecular simulation studies, process engineering studies, basic and detailed process design, simulation, optimization, and scale-up need to be implemented for newly developed materials. Membrane separation

technology has evolved as a competitive technique in energy production and CO₂ separation.^{22,23} Membrane separation is reported as a cost-effective, low energy consumption, continuous operation, as well as a flexible and durable process compared to traditional techniques.^{24,25} Membrane performance can be categorized based on the separation mechanism and structure of the materials, while the diffusion performance is mainly governed by morphological and physical properties. Textural properties of membrane structures mainly relate to innate characteristics such as pore volume, pore size distribution, average pore diameter, and pore length of the membrane. Membrane separation processes can achieve high CO₂ separation due to molecular sieving by variance of molecule size and diffusion principles.^{26,27} While separation processes in glassy material membranes (such as biphenol polysulfanes) depend mainly on difference in size or kinetic diameter of gas compounds, rubbery material membranes (such as polydimethyl siloxane) separate compounds based on condensability.²⁶ Glassy membranes are expected to perform better in gas separation applications; however, polymeric membranes have restrictions due to permeability versus selectivity of gases.

1.2 Objectives

This work mainly concentrates on IL applications in green sources of energy production. In the second chapter, we investigate the applicability of ILs for exfoliating bismuth telluride (Bi₂Te₃), which is a well-known thermoelectric material for high efficiency energy saving applications. In this part of the study, different types of ILs were used to calculate the potential of mean force and force regarding to initiate exfoliation. Since keeping exfoliated layers suspended is important, the charge orientation and confined liquid arrangement between suspended layers were thoroughly investigated. In this section of IL study, the most efficient solvent based on ILs in interaction with a bismuth telluride surface was evaluated.

In the second study, which is covered in chapters three and four, we explore novel types of membrane materials for CO₂ capture. Upon adding IL molecules to the backbone of the monomer (pyromellitic dianhydride as an organic ligand in this case) in the polymerization process, we were able to simulate ionic polyimide (i-IP) polymers by combining different types of anions (bis(trifluoromethylsulfonyl)imide ([Tf₂N⁻]), tetrafluoroborate ([BF₄⁻]), and hexafluorophosphate ([PF₆⁻])) in polymer structure. The target of our study in these sections is to design the most efficient polymer in base of CO₂ solubility and solubility-selectivity for both pre-combustion and post-combustion CO₂ capture. Mixing ILs with the prepared neat polymer to merge both polymer and ILs generates a composite structure. The structural modification of polymer structures during gas adsorption was explored and the effect of different anions on gas solubility and selectivity was evaluated.

1.3 Overview of computational methods

In this work, multiple computational techniques were applied such as: density functional theory (DFT), molecular dynamics (MD), and Monte Carlo (MC) simulations. In addition, some in-house codes were developed to prepare the input files for simulation, switch between different computational simulations (MD/MC), and analyze the extracted results. DFT calculations were used to perform the structure relaxation and predict the partial charge distribution on the monomers before polymerization. MD calculations were used to model the solvent interactions with the solid surface and the gas-liquid interaction. Furthermore, MC calculations were utilized to calculate the gas solubility of the prepared polymer. The following section explains the details of each approach.

1.3.1 *Density functional theory*

Using quantum mechanics calculations, the modeling of the small-scale systems (upper limit of thousands of atoms for times of 100 ps) is possible. It is possible to predict the electronic energy, bond structure, molecular orbitals, optimized geometry, vibration, and transition states of reactions. This scale of computational chemistry solves the Schrödinger equation (Kohn-Sham equation in DFT calculations) to evaluate the fundamental properties while considering the potential and kinetic energy of the system. Hohenberg and Kohn established that the total electron density completely determines all the ground state properties of the N-electron system.²⁸ Therefore, DFT can capture the kinetic energy correlation, while the Hartree-Fock-Slater method was missing dynamic correlation.²⁹ Kohn-Sham DFT is simpler than Hartree-Fock, and in principle it can predict the exact density and exact total energy of any interacting and correlated electron system by defining the exchange-correlation function and its derivative.²⁹ Kohn and Sham developed a simple model for exchange-correlation energy as a function of electron density called local density approximation (LDA).³⁰ Since then, other modification on LDA and hybrid forms of exchange-correlation energy have been developed. The generalized gradient approximation (GGA)³¹ was developed to improve LDA to calculate the energy required to dissociate a molecule called atomization energy. A hybrid form of the Lee, Yang, and Parr (LYP)³² correlation function called B3LYP was developed by Frisch and co-workers.^{33 34} To calculate the charge distribution after structural optimization, a variety of methods, such as electrostatic potential (ChelpG)³⁵, atomic orbital (Mulliken)³⁶, bonding orbitals (NBO)³⁷, and deformation density (Hirschfeld)³⁸ can be used.

In this work, structural optimization was calculated using Gaussian09³⁹ with a basis set of 6-31G(d) in B3LYP function.⁴⁰ In the mentioned split-valence basis set (6-31G(d)), known as

Pople basis sets⁴¹, the core orbital is described by a contraction of 6 Gaussian orbitals and the valence is described by two orbitals, one made of 3 Gaussians and another made of one Gaussian. Using the optimized structure of the monomer before polymerization, the partial charge calculation of each atom was conducted using the ChelpG method.³⁹ Other charge calculation schemes (Hirschfeld, NBO, Merz-Kollman) were also considered and consistent results were extracted. The partial charges that were evaluated from the ChelpG method in combination with OPLS-AA (all-atom optimized potentials for liquid simulations) force field parameters were chosen to modify the monomer topology file in the MD and MC calculations.

1.3.2 *Molecular dynamics and Monte Carlo simulations*

Larger systems containing millions of atoms can be simulated using computational methods such as MD and MC. At this level of simulation, the assigned and fixed partial charges of the atoms in combination with Leonard-Jones parameters are used to calculate the interactions within the system. Using the potential energy functions to calculate the atomic interactions in combination with Newtonian equations of motion, the thermodynamic properties such as density, heat capacity, surface tension, solubility and transport properties of the complex systems can be investigated. To this extent, robust force field parameters regarding the phase and molecular composition of the system should be implemented. The optimized potential for liquid solvation (OPLS) force field, developed by William L. Jorgensen, is well suited for specific functional groups and carbohydrates.⁴² Choosing between MD and MC largely depends on the desired phenomenon being investigated in the system. Molecular transition in interaction with neighboring atoms enables MD to be efficient in transport property calculations such as viscosity. However, simulation of the system with varying particle numbers (grand canonical Monte Carlo (GCMC)⁴³) is the versatile benefit of MC in comparison to MD calculations.

During GCMC calculations, the created molecules can move in interaction with surrounding molecules, and the density can fluctuate in constant volume and temperature by inserting and deleting molecules.

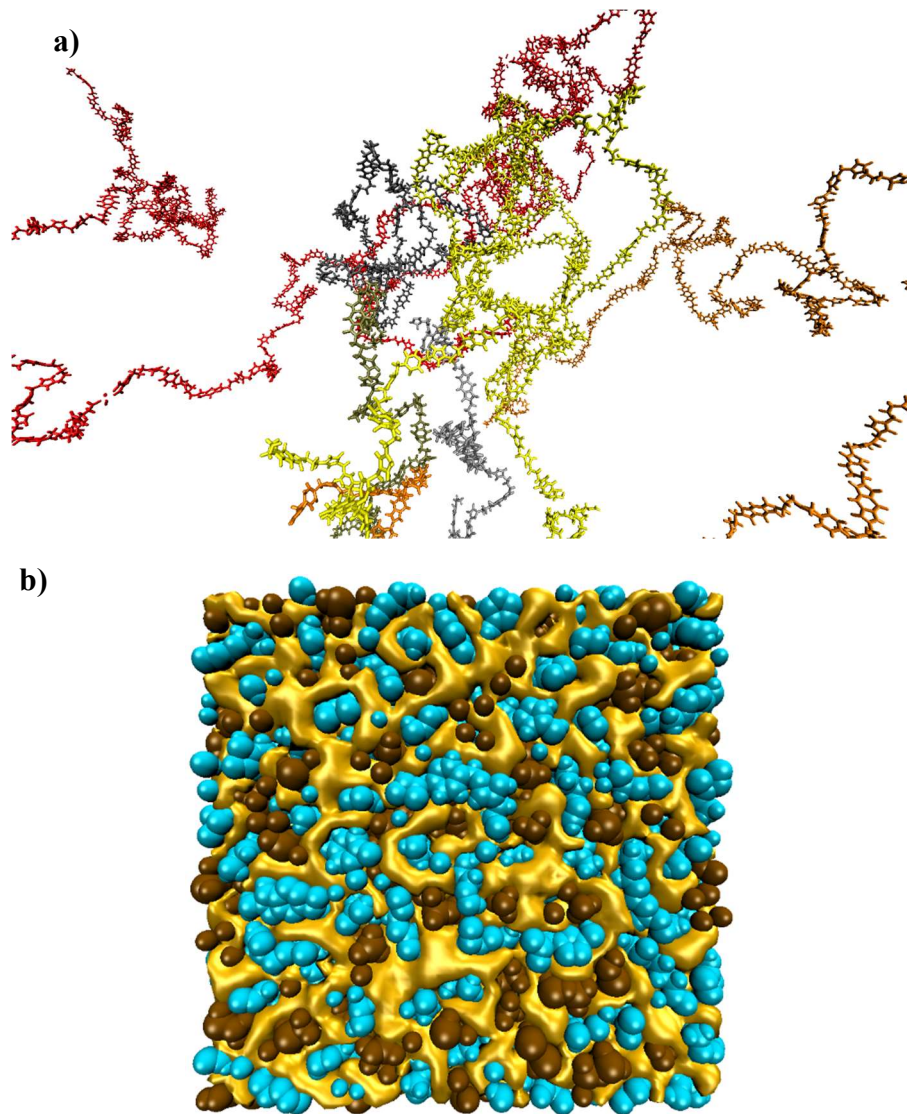


Figure 1.1. a) The polymer structure after relaxation. Anions were deleted for clarity. b) The polymer structure considering periodic boundary conditions in the x, y, and z direction. The golden area was the porosity created by polymer chains. Polymer chains are represented in light blue and anions are represented in dark red.

1.4 Overview of our work

Bismuth telluride (Bi_2Te_3) exfoliation was studied through a liquid phase exfoliation technique. Imidazolium-based ILs were used as a potential ionic liquid solvent to initiate the exfoliation due to a small discrepancy between the surface energy of ionic liquids and the estimated surface energy of the Bi_2Te_3 (63-81 mJ/m^2). The solvents were prepared by pairing different cations and anions. In this work, 1-n-butyl-3-methylimidazolium ($[\text{C}_4\text{mim}^+]$) and 1-n-ethyl-3-methylimidazolium ($[\text{C}_2\text{mim}^+]$) were used as cations in combination with bis(trifluoromethylsulfonyl)imide ($[\text{Tf}_2\text{N}^-]$), hexafluorophosphate ($[\text{PF}_6^-]$), bromide ($[\text{Br}^-]$), and chloride ($[\text{Cl}^-]$) as anions. Exfoliation was started by implementing steered molecular dynamics calculations in different temperatures ranging from 350 to 550 K. The evaluation of different solvents showed that $[\text{Tf}_2\text{N}^-]$ -based ILs are a potentially more effective solvent to enhance exfoliation. The unique solvation structures of the $[\text{Tf}_2\text{N}^-]$ -based ILs that developed on the surface of the Bi_2Te_3 explained the effective exfoliation process.

In addition, CO_2 solubility capacity and selectivity in the imidazolium-based ILs provided a great subject of interest to explore, specifically regarding the potential application of these types of ILs in industrial scale CO_2 separation processes. In our study, “ionic polyimides” (i-IPs) have been reported as a new class of condensation polymers, which combine structural components of both ionic liquids (ILs) and polyimides through covalent linkages (**Figure 1.1**).

To combine both IL gas selectivity and i-IP gas solubility capacity, a composite of i-IP in different concentrations of ILs were prepared. It is found that the 50% IL addition can increase CO₂/CH₄ selectivity by 16% in [BF₄⁻]-based and by 36% in [PF₆⁻]-based structures for 5% of CO₂ in CO₂/CH₄ mixtures. Higher gas solubility capacity was found in [PF₆⁻]-based structures. While the [BF₄⁻]-based system shows higher CO₂/CH₄ selectivity, the [Tf₂N⁻]-based system shows higher CO₂/N₂ gas separation performance.

References

- (1) Ding, L. C.; Akbarzadeh, A.; Tan, L. A review of power generation with thermoelectric system and its alternative with solar ponds. *Renew. Sust. Energ. Rev.* **2018**, *81*, 799-812.
- (2) Choi, J.; Lee, J. Y.; Lee, S.-S.; Park, C. R.; Kim, H. High-Performance Thermoelectric Paper Based on Double Carrier-Filtering Processes at Nanowire Heterojunctions. *Adv. Energy Mater.* **2016**, *6*, 1502181.
- (3) Zhu, T.; Liu, Y.; Fu, C.; Heremans, J. P.; Snyder, J. G.; Zhao, X. Compromise and Synergy in High-Efficiency Thermoelectric Materials. *Adv. Mater.* **2017**, *29*.
- (4) Hu, L.; Wu, H.; Zhu, T.; Fu, C.; He, J.; Ying, P.; Zhao, X. Tuning Multiscale Microstructures to Enhance Thermoelectric Performance of n-Type Bismuth-Telluride-Based Solid Solutions. *Adv. Energy Mater.* **2015**, *5*, 1500411.
- (5) Ding, D.; Lu, C.; Tang, Z. Bottom Up Chalcogenide Thermoelectric Materials from Solution-Processed Nanostructures. *Adv. Mater. Interfaces* **2017**, *4*, 1700517.
- (6) Kumar, S.; Cho, J. H.; Moon, I. Ionic liquid-amine blends and CO₂ BOLs: Prospective solvents for natural gas sweetening and CO₂ capture technology—A review. *Int. J. Greenh. Gas Con.* **2014**, *20*, 87-116.
- (7) Abdul Halim, H. N.; M. Shariff, A.; Tan, L. S.; Bustam, M. A. Mass Transfer Performance of CO₂ Absorption from Natural Gas using Monoethanolamine (MEA) in High Pressure Operations. *Ind. Eng. Chem. Res.* **2015**, *54*, 1675-1680.
- (8) Budhathoki, S.; Shah, J. K.; Maginn, E. J. Molecular Simulation Study of the Performance of Supported Ionic Liquid Phase Materials for the Separation of Carbon Dioxide from Methane and Hydrogen. *Ind. Eng. Chem. Res.* **2017**, *56*, 6775-6784.
- (9) Cadena, C.; Anthony, J. L.; Shah, J. K.; Morrow, T. I.; Brennecke, J. F.; Maginn, E. J. Why is CO₂ so soluble in imidazolium-based ionic liquids? *J. Am. Chem. Soc.* **2004**, *126*, 5300-5308.
- (10) Li, Z.; Xiao, Y.; Xue, W.; Yang, Q.; Zhong, C. Ionic Liquid/Metal–Organic Framework Composites for H₂S Removal from Natural Gas: A Computational Exploration. *J. Phys. Chem. C* **2015**, *119*, 3674-3683.
- (11) Harris, K. R.; Kanakubo, M. Self-diffusion, velocity cross-correlation, distinct diffusion and resistance coefficients of the ionic liquid [BMIM][Tf₂N] at high pressure. *Phys. Chem. Chem. Phys.* **2015**, *17*, 23977-23993.
- (12) Kinik, F. P.; Altintas, C.; Balci, V.; Koyuturk, B.; Uzun, A.; Keskin, S. [BMIM][PF₆] Incorporation Doubles CO₂ Selectivity of ZIF-8: Elucidation of Interactions and Their Consequences on Performance. *ACS Appl. Mater. Inter.* **2016**, *8*, 30992-31005.
- (13) Wu, N.; Ji, X.; Xie, W.; Liu, C.; Feng, X.; Lu, X. Confinement Phenomenon Effect on the CO₂ Absorption Working Capacity in Ionic Liquids Immobilized into Porous Solid Supports. *Langmuir* **2017**, *33*, 11719-11726.
- (14) Ramdin, M.; Balaji, S. P.; Vicent-Luna, J. M.; Gutiérrez-Sevillano, J. J.; Calero, S.; de Loos, T. W.; Vlugt, T. J. H. Solubility of the Precombustion Gases CO₂, CH₄, CO, H₂, N₂, and H₂S in the Ionic Liquid [bmim][Tf₂N] from Monte Carlo Simulations. *J. Phys. Chem. C* **2014**, *118*, 23599-23604.
- (15) Bara, J. E.; Carlisle, T. K.; Gabriel, C. J.; Camper, D.; Finotello, A.; Gin, D. L.; Noble, R. D. Guide to CO₂ Separations in Imidazolium-Based Room-Temperature Ionic Liquids. *Ind. Eng. Chem. Res.* **2009**, *48*, 2739-2751.

- (16) To, J. W.; He, J.; Mei, J.; Haghpanah, R.; Chen, Z.; Kurosawa, T.; Chen, S.; Bae, W. G.; Pan, L.; Tok, J. B.; Wilcox, J.; Bao, Z. Hierarchical N-Doped Carbon as CO₂ Adsorbent with High CO₂ Selectivity from Rationally Designed Polypyrrole Precursor. *J. Am. Chem. Soc.* **2016**, *138*, 1001-1009.
- (17) Delgado, J. A.; Águeda, V. I.; Uguina, M. A.; Sotelo, J. L.; Brea, P.; Grande, C. A. Adsorption and Diffusion of H₂, CO, CH₄, and CO₂ in BPL Activated Carbon and 13X Zeolite: Evaluation of Performance in Pressure Swing Adsorption Hydrogen Purification by Simulation. *Ind. Eng. Chem. Res.* **2014**, *53*, 15414-15426.
- (18) Vicent-Luna, J. M.; Luna-Triguero, A.; Calero, S. Storage and Separation of Carbon Dioxide and Methane in Hydrated Covalent Organic Frameworks. *J. Phys. Chem. C* **2016**, *120*, 23756-23762.
- (19) Xiang, Z.; Mercado, R.; Huck, J. M.; Wang, H.; Guo, Z.; Wang, W.; Cao, D.; Haranczyk, M.; Smit, B. Systematic Tuning and Multifunctionalization of Covalent Organic Polymers for Enhanced Carbon Capture. *J. Am. Chem. Soc.* **2015**, *137*, 13301-13307.
- (20) Olajire, A. A. CO₂ capture and separation technologies for end-of-pipe applications – A review. *Energy* **2010**, *35*, 2610-2628.
- (21) D'Alessandro, D. M.; Smit, B.; Long, J. R. Carbon Dioxide Capture: Prospects for New Materials. *Angew. Chem. Int. Edit.* **2010**, *49*, 6058-6082.
- (22) MacDowell, N.; Florin, N.; Buchard, A.; Hallett, J.; Galindo, A.; Jackson, G.; Adjiman, C. S.; Williams, C. K.; Shah, N.; Fennell, P. An overview of CO₂ capture technologies. *Energ. Environ. Sci.* **2010**, *3*, 1645.
- (23) Vinoba, M.; Bhagiyalakshmi, M.; Alqaheem, Y.; Alomair, A. A.; Pérez, A.; Rana, M. S. Recent progress of fillers in mixed matrix membranes for CO₂ separation: A review. *Sep. Purif. Technol.* **2017**, *188*, 431-450.
- (24) Sridhar, S.; Smitha, B.; Aminabhavi, T. M. Separation of carbon dioxide from natural gas mixtures through polymeric membranes - A review. *Sep. Purif. Rev.* **2007**, *36*, 113-174.
- (25) Du, N.; Park, H. B.; Dal-Cin, M. M.; Guiver, M. D. Advances in high permeability polymeric membrane materials for CO₂ separations. *Energy Environ. Sci.* **2012**, *5*, 7306-7322.
- (26) Kapantaidakis, G. C.; Kaldis, S. P.; Sakellariopoulos, G. P.; Chira, E.; Loppinet, B.; Floudas, G. Interrelation between phase state and gas permeation in polysulfone/polyimide blend membranes. *J. Polym. Sci. Pol. Phys.* **1999**, *37*, 2788-2798.
- (27) Wang, S.; Li, X.; Wu, H.; Tian, Z.; Xin, Q.; He, G.; Peng, D.; Chen, S.; Yin, Y.; Jiang, Z.; Guiver, M. D. Advances in high permeability polymer-based membrane materials for CO₂ separations. *Energ. Environ. Sci.* **2016**, *9*, 1863-1890.
- (28) Hohenberg, P.; Kohn, W. Inhomogeneous Electron Gas. *Phys. Rev. B* **1964**, *136*, B864-B871.
- (29) Becke, A. D. Perspective: Fifty years of density-functional theory in chemical physics. *J. Chem. Phys.* **2014**, *140*.
- (30) Vosko, S. H.; Wilk, L.; Nusair, M. Accurate Spin-Dependent Electron Liquid Correlation Energies for Local Spin-Density Calculations - a Critical Analysis. *Can. J. Phys.* **1980**, *58*, 1200-1211.
- (31) Perdew, J. P.; Burke, K.; Ernzerhof, M. Generalized gradient approximation made simple. *Phys. Rev. Lett.* **1996**, *77*, 3865-3868.
- (32) Lee, C.; Yang, W.; Parr, R. G. Development of the Colle-Salvetti correlation-energy formula into a functional of the electron density. *Phys. Rev. B* **1988**, *37*, 785-789.
- (33) Gill, P. M. W.; Johnson, B. G.; Pople, J. A.; Frisch, M. J. An Investigation of the Performance of a Hybrid of Hartree-Fock and Density Functional Theory. *Int. J. Quantum Chem.* **1992**, 319-331.

- (34) Burke, K. Perspective on density functional theory. *J. Chem. Phys.* **2012**, *136*.
- (35) Breneman, C. M.; Wiberg, K. B. Determining Atom-Centered Monopoles from Molecular Electrostatic Potentials - the Need for High Sampling Density in Formamide Conformational-Analysis. *J. Comput. Chem.* **1990**, *11*, 361-373.
- (36) Mulliken, R. S. Electronic Population Analysis on Lcao-Mo Molecular Wave Functions .1. *J. Chem. Phys.* **1955**, *23*, 1833-1840.
- (37) Wilkens, S. J.; Westler, W. M.; Markley, J. L.; Weinhold, F. Natural J-coupling analysis: Interpretation of scalar J-couplings in terms of natural bond orbitals. *J. Am. Chem. Soc.* **2001**, *123*, 12026-12036.
- (38) Hirshfeld, F. L. Bonded-Atom Fragments for Describing Molecular Charge-Densities. *Theor. Chim. Acta.* **1977**, *44*, 129-138.
- (39) Frisch, M. J.; Trucks, G. W.; Schlegel, H. B.; Scuseria, G. E.; Robb, M. A.; Cheeseman, J. R.; Scalmani, G.; Barone, V.; Mennucci, B.; Petersson, G. A.; Nakatsuji, H.; Caricato, M.; Li, X.; Hratchian, H. P.; Izmaylov, A. F.; Bloino, J.; Zheng, G.; Sonnenberg, J. L.; Hada, M.; Ehara, M.; Toyota, K.; Fukuda, R.; Hasegawa, J.; Ishida, M.; Nakajima, T.; Honda, Y.; Kitao, O.; Nakai, H.; Vreven, T.; Montgomery Jr., J. A.; Peralta, J. E.; Ogliaro, F.; Bearpark, M. J.; Heyd, J.; Brothers, E. N.; Kudin, K. N.; Staroverov, V. N.; Kobayashi, R.; Normand, J.; Raghavachari, K.; Rendell, A. P.; Burant, J. C.; Iyengar, S. S.; Tomasi, J.; Cossi, M.; Rega, N.; Millam, N. J.; Klene, M.; Knox, J. E.; Cross, J. B.; Bakken, V.; Adamo, C.; Jaramillo, J.; Gomperts, R.; Stratmann, R. E.; Yazyev, O.; Austin, A. J.; Cammi, R.; Pomelli, C.; Ochterski, J. W.; Martin, R. L.; Morokuma, K.; Zakrzewski, V. G.; Voth, G. A.; Salvador, P.; Dannenberg, J. J.; Dapprich, S.; Daniels, A. D.; Farkas, Ö.; Foresman, J. B.; Ortiz, J. V.; Cioslowski, J.; Fox, D. J.: Gaussian 09. Gaussian, Inc.: Wallingford, CT, USA, 2009.
- (40) Becke, A. D. Density-functional thermochemistry. III. The role of exact exchange. *J. Chem. Phys.* **1993**, *98*, 5648-5652.
- (41) Ditchfield, R.; Hehre, W. J.; Pople, J. A. Self-Consistent Molecular-Orbital Methods .9. Extended Gaussian-Type Basis for Molecular-Orbital Studies of Organic Molecules. *J. Chem. Phys.* **1971**, *54*, 724-728.
- (42) Jorgensen, W. L.; Maxwell, D. S.; TiradoRives, J. Development and testing of the OPLS all-atom force field on conformational energetics and properties of organic liquids. *J. Am. Chem. Soc.* **1996**, *118*, 11225-11236.
- (43) Adams, D. J. Grand Canonical Ensemble Monte-Carlo for a Lennard-Jones Fluid. *Mol. Phys.* **1975**, *29*, 307-311.

2. MOLECULAR DYNAMICS SIMULATION OF BISMUTH TELLURIDE EXFOLIATION MECHANISMS IN DIFFERENT IONIC LIQUID SOLVENTS¹

2.1 Introduction

Bismuth Telluride (Bi_2Te_3) and other layered chalcogenide materials are currently being investigated for their interesting thermoelectric, catalytic properties, and optical properties.¹⁻³ In particular, the bulk thermal and electrical properties of Bi_2Te_3 can be very different when the thickness of the material is decreased to less than 10 nm.⁴ When these materials are exfoliated into very thin layers, phonon scattering is increased (decreasing the thermal conductivity), while their high crystallinity enhances their electrical conductivity. As a result, these materials possess valuable thermoelectric properties, with a high thermoelectric “figure of merit”.⁵ However, in order to move this technology forward and aid commercialization, there still need to be fundamental investigations about the different material growth processes, exfoliation techniques, and interactions between these materials and different solvents.

Currently, vapor-phase deposition^{6,7} or liquid-phase synthesis^{8,9} can produce two-dimensional (2D) nanosheets of Bi_2Te_3 . However, we focus on liquid-phase synthesis, since it can potentially provide an economical route for large-scale production, and there is very little information available about the interaction of these materials with different liquid solvents. The individual crystal layers of Bi_2Te_3 are quintuple sheets of the order Te1-Bi-Te2-Bi-Te1 (bonded

¹ Reprinted with permission from LANGMUIR, doi: 10.1021/acs.langmuir.6b02663. Copyright © 2016 American Chemical Society.

covalently), with a thickness of approximately 1 nm. The bulk Bi₂Te₃ material is composed of stacked quintuple sheets, with only weak dispersion interactions acting between the neighboring nanosheets.

In the past, liquid-phase exfoliation¹⁰ has been frequently used to generate 2D nanosheets from bulk materials, including metal oxide nanosheets,¹¹ graphene,^{12,13} hexagonal boron nitride (h-BN),^{14,15} metal chalcogenides,¹⁶⁻¹⁸ phosphorene,^{19,20} and black phosphorus.²¹ Among the different possible solvents, ionic liquids (ILs) have received a great deal of interest.²² This is due to many of the inherent properties of these compounds:²³⁻²⁵ low volatility, high thermal stability, low melting point, potential recyclability, and the high degree of tunability by pairing different IL cations and anions. In addition, understanding the fundamental interaction of ILs with 2D materials is important to many emerging technical applications (capacitors, batteries, sensors, lubrication, etc.).²⁶⁻³⁰

Molecular dynamics (MD) simulations are particularly useful for understanding the interfacial behavior and the thermophysical properties of ILs.^{31,32} In the past, there have already been a few attempts at modeling the exfoliation behavior of different nanomaterials in IL solvents. This includes, the exfoliation of bilayer graphene nanosheets,³³ hexagonal boron nitride (h-BN),³⁴ and bismuth telluride.¹⁶ As an example, Baker et al.³³ used adaptive bias force-molecular dynamics (ABF-MD) to determine the free energy of exfoliation for graphene bilayer in different IL solvents. Their simulations were initiated by positioning the two graphene layers approximately 10 angstroms apart, allowing the IL molecules to intercalate within the slit-shaped gap. In the exfoliation simulations, the initial separation was followed by shearing the upper graphene layer from the IL solvent to the vacuum and calculating the free energy of the process and the potential of mean force (PMF). In contrast to many of the previous studies, we are

focused on the thermodynamics of the initial exfoliation step, which leads to the subsequent IL intercalation. The electrostatic characteristics of the Bi_2Te_3 surface provide for unique interfacial properties that are not encountered in many of the other 2D systems. For instance, while Bi_2Te_3 nanosheets are charge-neutral, the Te atoms cover the basal plane of the quintuple sheets, and this presents a negatively-charged surface that can have strong interfacial interactions with polar or charged molecules, such as ionic liquids.

Currently, there is a lack of knowledge about how to design effective IL solvents for exfoliating and stabilizing chalcogenide nanosheets. A deeper molecular-level understanding of these systems is needed, including the structure of the solvent molecules at the interface. With this knowledge in hand, there can be much clearer experimental targets for synthesizing solvents that provide the necessary structural and electrostatic interactions for effective exfoliation.

In our study, we use MD simulations to model the initial exfoliation of Bi_2Te_3 in eight different imidazolium-based ILs, composed of different cation/anion species (structures illustrated in **Figure A2.11**): $[\text{C}_4\text{mim}^+]/[\text{C}_2\text{mim}^+]$ and $[\text{Tf}_2\text{N}^-]/[\text{PF}_6^-]/[\text{Br}^-]/[\text{Cl}^-]$. Imidazolium-based ionic liquids are air and water stable,³⁵ these imidazolium-based ILs have surface energies estimated to be 63-83 mJ/m^2 ,^{15,36} which provide a commensurate match with the estimated surface energy of Bi_2Te_3 (63-81 mJ/m^2).¹⁶ This close match in surface energy of ILs and Bi_2Te_3 is expected to be helpful for exfoliation, similar to other surface energy matching techniques.¹² Our previous study showed that the ionic liquid $[\text{C}_4\text{mim}^+][\text{Cl}^-]$ can act as an effective exfoliation solvent for Bi_2Te_3 , and the exfoliation of the layers is primarily driven by the cation.¹⁶ The interfacial IL structure on Bi_2Te_3 forms an alternating double-layer of cations and anions, which propagates 2 to 3 nm away from the interface, and this is consistent with IL behavior at other surfaces.³⁷⁻³⁹ Based on our initial MD simulations of small Bi_2Te_3 models in a single IL solvent,

the exfoliation process is predicted to start from a shearing and peeling mechanism. Thus, in this study, steered molecular dynamics simulations are used to directly explore three different viable exfoliation mechanisms (peeling, pulling, and shearing), as illustrated in **Figure 2.1**. Overall, our simulations indicate that peeling is the most probable initiation mechanism. Furthermore, the $[\text{C}_4\text{mim}^+][\text{Tf}_2\text{N}^-]$ solvent provides the lowest barrier for exfoliation, and its effectiveness can be traced to its unique cation and anion interactions with the surface of the Bi_2Te_3 quintuple sheets.

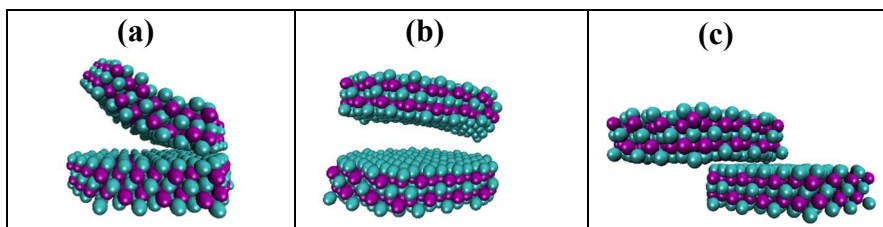


Figure 2.1. Illustration of the exfoliation mechanisms simulated for the bilayer Bi_2Te_3 system: (a) peeling, (b) pulling, and (c) shearing. The atom colors represent Te (cyan) and Bi (purple).

2.2 Simulation Methods

All of our MD simulations have been performed with the GROMACS 4.6.5 simulation package.⁴⁰ The IL molecular interactions are described with the OPLS-AA force field.⁴¹ The IL force field parameters were taken from Lopes, et al.³¹ with Lennard-Jones interactions and partial atomic charges assigned to individual atoms. A Morse potential was used to describe the interaction within the quintuple sheets of Bi_2Te_3 , and these parameters were developed by Qui and Ruan.⁴² For describing the IL- Bi_2Te_3 parameters, UFF parameters⁴³ were used for Bi_2Te_3 , and cross-term interactions were estimated using the Lorentz-Berthelot mixing rules. The Lennard-Jones potential and electrostatic interactions were both truncated at a distance of 1.4 nm. Long-range electrostatic interactions were calculated with the smooth particle mesh Ewald sum (SPME),⁴⁴ with a 0.16 nm of Fourier-spacing parameter. Periodic boundary conditions were applied in all three dimensions. The Parrinello-Rahman barostat^{45,46} was used to maintain the

pressure, and the Nose-Hoover thermostat⁴⁷ was used to maintain the temperature in our isothermal-isobaric (NPT) ensemble simulations.

We simulated three different exfoliation mechanisms to find the most thermodynamically-preferred route. In all exfoliation processes (peeling, pulling, and shearing), position restraints on the Bi_2Te_3 sheets were used during equilibration and solvent relaxation to prevent the 2D nanosheets from prematurely separating (before the surrounding solvent has time to equilibrate). All initial solvent configurations were generated by PACKMOL,⁴⁸ followed by an energy minimization process using the steepest descent algorithm. In order to accommodate the Bi_2Te_3 layers in the peeling and pulling simulations, rectangular cells with dimensions of $7.0 \times 7.0 \times 16.0 \text{ nm}^3$ were used, while a $7.0 \times 12.0 \times 7.0 \text{ nm}^3$ box was used for the shearing simulations. Each box contains 1000 to 3100 pairs of anions and cations, in addition to two quintuple sheets of Bi_2Te_3 , with 435 atoms per sheet. The Bi_2Te_3 sheets have a hexagonal cross-section in order to make our model consistent with the geometries often observed in the experimental studies. To relax the IL molecules before running the steered molecular dynamics (SMD) simulations,⁴⁹ the temperature was first raised to 2000 K in the NVT ensemble. Then, NPT simulations were used to gradually decrease the pressure to one bar and the chosen final temperature. Prior to beginning the SMD simulations, the systems were allowed to further relax for 5 ns (using a time step of 1 fs). Additional details of our simulation methods and analyses are provided within the context of our results in the next section.

2.3 Results and Discussion

We use several different approaches to analyze our IL- Bi_2Te_3 systems. We first used SMD simulations to identify the maximum force necessary to initiate the exfoliation process at different temperatures and in different IL solvents. For more rigorous comparison, we then use

the SMD simulations to evaluate the PMF along the exfoliation process, with a goal of identifying the minimum energy pathway among the different exfoliation mechanisms and IL solvents. After the exfoliation energetics of the different scenarios are estimated, we perform detailed analyses of the IL structure at the Bi₂Te₃ interface in order to help identify the underlying molecular interactions responsible for the exfoliation behavior in the different ILs.

As mentioned previously, eight different ILs are included in our study (with cations/anion structures shown in **Figure A2.11**), and the available physical properties of these solvents are listed in **Table A2.1**. The melting temperatures and decomposition temperatures help set the general bounds of the temperature range in our investigation (350 K to 550 K), and the experimental densities are used to benchmark the simulated values in our study.

2.3.1 Steered Molecular Dynamics Simulations

In the past, the SMD technique has been used to quantify the thermodynamics of different processes within a wide variety of systems, including biological macromolecules,^{50,51} carbon nanotubes,^{52,53} thermoelectric materials,⁵⁴⁻⁵⁶ nanoparticles,⁵⁷ and lubrication.^{28,58} In brief, SMD simulations perturb a system by applying a moving spring force to a specific point of the target. The amount of force (F_{SMD}) is dictated by the end moving velocity (v) and the stiffness of the spring (K) as shown in Equation 1.

$$F_{SMD} = K(x_0 + vt - x) \quad (1)$$

In this equation, (x_0) is the initial position of the restraint point and (x) is the distance from the spring end to the target tether point. The spring stiffness and the end moving velocity can affect the energy pathway of the system,^{50,59} so several different values were tested to ensure reliable results (tests with different parameters are included in the Supporting Information). After system equilibration, the exfoliation process is implemented by moving the top layer of the

Bi₂Te₃ system in three different directions, corresponding to: peeling (dragging one edge of the top layer in a direction normal to the surface), pulling (dragging the entire top layer in a direction normal to the surface), and shearing processes (dragging the top layer in a direction perpendicular to the surface normal), while the lower layer is restrained in its position. These mechanisms are illustrated in **Figure 2.1**. While the actual experimental mechanism may not strictly follow these trajectories, a comparison of the energetics of these exfoliation pathways helps to characterize the most plausible route.

As an example of the SMD simulations, **Figure A2.17** illustrates the applied force during the peeling simulation within the [C₄mim⁺]-based ILs at a temperature of 450 K. In all cases, the spring force increases until the initial separation force is reached. Once the separation is initiated, there is still additional force needed to continue the exfoliation process, and this represents a combination of the force necessary to disrupt the Bi₂Te₃-Bi₂Te₃ interactions and the force needed to rearrange the surrounding IL solvent molecules. The initial equilibrium center-of-mass distance between the two sheets is ~1.1 nm, and the exfoliation mechanism tends to begin at a center-of-mass distance of ~1.3 nm. From each of these simulations, we have recorded the maximum applied force along the exfoliation trajectory, and we use this information to make a general comparison of the energetics of the three different exfoliation mechanisms and eight different IL solvents.

The results of the SMD simulations are compiled in **Figure 2.2**. Five different temperatures were tested (350 K to 550 K), which should correspond to the usable range of the IL solvents. In general, the peeling mechanism requires the least amount of force to initiate, and this result is consistently seen at different temperatures and when comparing different solvents. This is the also the same mechanism previously used to model the exfoliation of phosphorene.²⁰ Also, in

most cases, the maximum applied exfoliation force required in the $[\text{C}_4\text{mim}^+]$ -based solvents is just slightly less than that for the $[\text{C}_2\text{mim}^+]$ -based systems. Within our group of 8 ILs, the $[\text{Tf}_2\text{N}^-]$ -based solvents tend to require the least applied force to perform the exfoliation, while the $[\text{Cl}^-]$ -based ILs tend to require the most (although there are exceptions). As expected, the applied force is lower at the higher temperatures, and there is much less distinction between the different solvents at the elevated temperatures.

The maximum force provides a good initial reference for comparing the energetics of the different exfoliation mechanisms and IL solvents, but a more rigorous analysis can be made by examining the potential of mean force along the different exfoliation trajectories. Due to the computational demands of these calculations, PMF curves are only generated for a subset of our systems. In particular, the most promising IL solvent $[\text{C}_4\text{mim}^+][\text{Tf}_2\text{N}^-]$ is analyzed, as well as several of its variants.

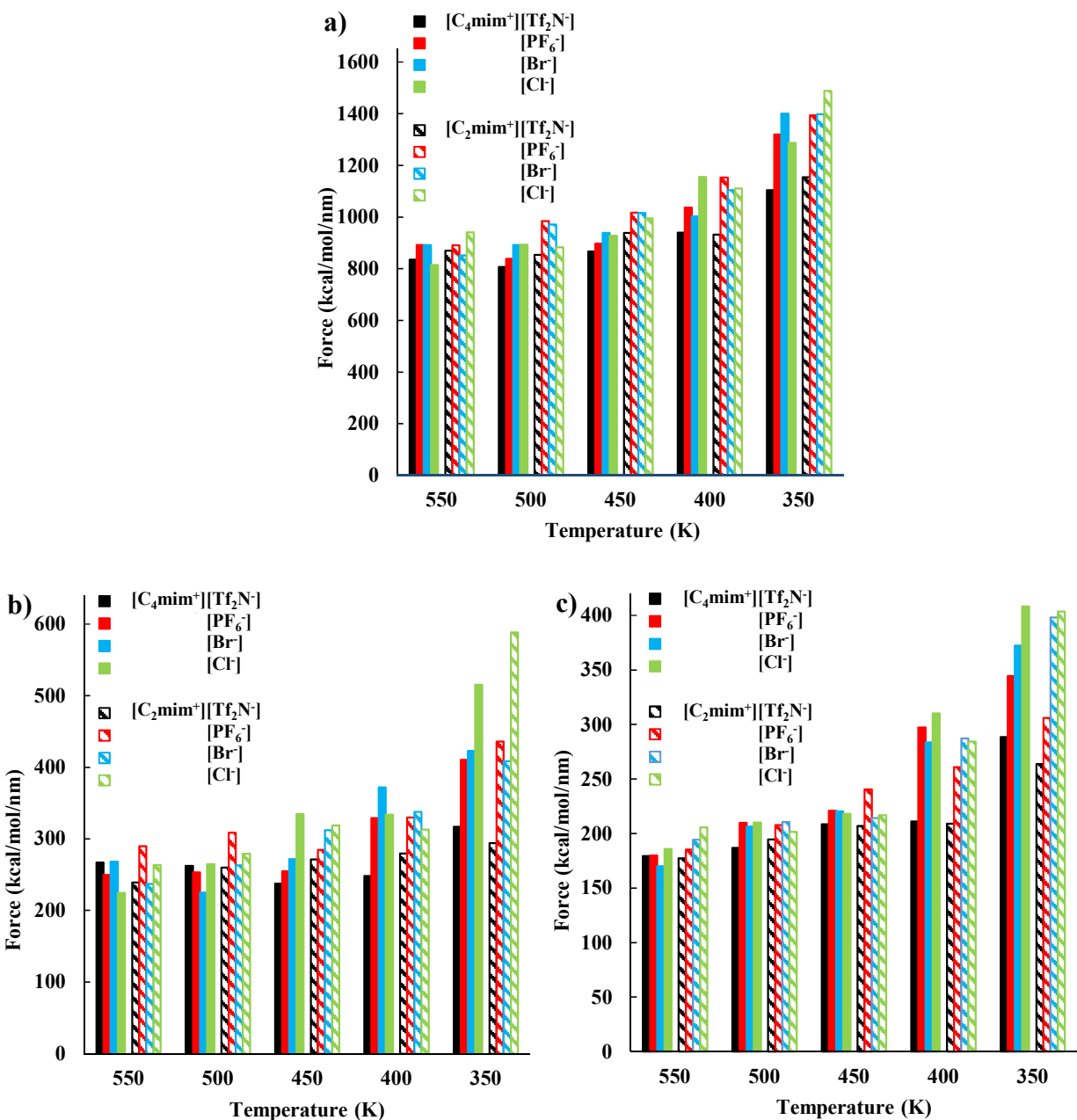


Figure 2.2. Maximum applied force for exfoliation of Bi_2Te_3 via the a) pulling, b) shearing, and c) peeling mechanisms.

2.3.2 Potential of Mean Force

For selected systems, we generated PMF curves to more rigorously compare the Bi_2Te_3 exfoliation energetics. The chosen systems were based on the most effective IL from the SMD

analysis ([C₄mim⁺][Tf₂N⁻]), and both the pulling and peeling mechanisms were compared, which were previously identified to be the least favorable and most favorable exfoliation mechanisms, respectively. In addition, because of the computational demands of the lower-temperature simulations (i.e., slow convergence), the PMF calculations were only performed at the highest temperature of 550 K. The results from the SMD simulations are generally consistent at the low and high temperatures. Furthermore, the molecular structure of the IL molecules demonstrates similar behavior at the low and high temperatures. As an example, Figure S-8 of the Supporting Information compares several different IL density profiles at 450 K and 550 K at the Bi₂Te₃ interface. At the two different temperatures, the position of the density profile peaks are only slightly displaced (1-15%) and the heights of the density profile peaks are only moderately varied (3-20%).

In order to generate the PMF curves, a harmonic spring force is used to stabilize the top Bi₂Te₃ layer at fixed positions along the exfoliation trajectory, while the bottom layer is held in place. Each one of the fixed positions along the trajectory corresponds to a separate simulation or “window”, and during the simulation, the remainder of the system relaxes (with respect to the applied harmonic restraint). In our particular systems, we needed approximately 300 different windows (each approximately 1 ns in duration) along the pulling and peeling trajectories to obtain converged results. This harmonic force was applied to the center of mass of the Bi₂Te₃ nanosheet during the pulling simulation, while the force was applied to the edge atoms during the peeling simulations. Once completed, the individual windows were combined to produce the PMF using the weighted histogram analysis method (WHAM).⁶⁰ The PMF was calculated with a convergence tolerance of 10⁻⁶.

The PMF results are summarized in **Figure 2.3**. Although the SMD predictions of the maximum exfoliation force provide a reasonable initial comparison, the PMF plots provide more differentiation amongst the different IL solvents. While we still find that $[\text{C}_4\text{mim}^+][\text{Tf}_2\text{N}^-]$ provides the lowest energy pathway to exfoliation, there is greater distinction found for the other IL pairs. The $[\text{Br}^-]$ and $[\text{Cl}^-]$ anions increase the PMF barrier by 30-40%, and the $[\text{C}_2\text{mim}^+]$ cation shows a slight elevation in the PMF exfoliation barrier. A comparison of the $[\text{C}_4\text{mim}^+]$ and the $[\text{C}_2\text{mim}^+]$ results tend to corroborate results from our previous MD simulations¹⁶ that predicted the imidazolium ring interacts strongly with the Bi_2Te_3 surface. Hence, the shorter $[\text{C}_2\text{mim}^+]$ tail seems to only have a small influence on the initial cation penetration and subsequent nanosheet separation.

When comparing the pulling versus peeling trajectories, the PMF results mimic the initial SMD data. The peeling process is still predicted to be the most likely route, and this is also the mechanism that is the most physically intuitive. The direct pulling (or sliding) mechanism inherently involves energetic barriers that are proportional to the Bi_2Te_3 cross-sectional area. For instance, when following the direct exfoliation trajectory, there is a very large amount of force that has to be exerted to pull apart the nanosheet layers. During this initial separation process, a vacuum region is created between the nanosheets (with a volume directly proportional to the Bi_2Te_3 cross-section), and the IL solvent is not able to penetrate the gap and passivate the surfaces until a separation distance of approximately 0.6-0.7 nm is reached (as reflected in **Figure 2.4**). In contrast, during the peeling process, the IL solvent is able to gradually intercalate and passivate the Bi_2Te_3 surfaces, as the top layer is incrementally peeled away from the bottom. The difference in the exfoliation energetics is also reflected in the overall quality of the PMF data in parts (a) and (b) of **Figure 2.3**. The direct pulling process is difficult to

stabilize, requiring very large spring forces, and this leads to a great deal of noise in the PMF curves. Even with additional simulation time and additional windows, the statistical noise in the data is still very difficult to eliminate.

The exfoliation energetics and the performance of different IL solvents can be attributed to their molecular-level interactions with the Bi_2Te_3 interface. By analyzing the molecular structure (total density, individual site distributions, and orientations), we can learn a great deal about the trends in the SMD data and PMF curves.

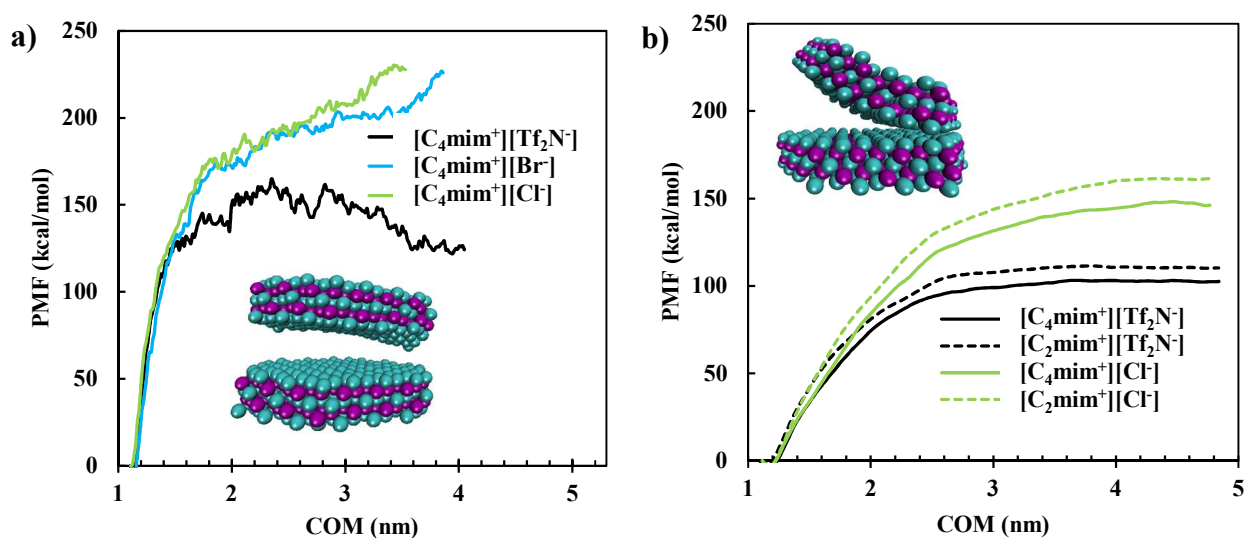


Figure 2.3. PMF results for Bi_2Te_3 exfoliation at 550 K for: (a) pulling and (b) peeling process.

2.4 Density Profile

Along with analyzing the molecular density profiles, we also benchmarked our simulation results against available experimental data. **Figures A2.19** and **A2.20** show the density profiles of the IL, plotted as a function of the distance from the Bi_2Te_3 interface. The interface of Bi_2Te_3 corresponds to $z = 0$, and this is defined as the center of mass of the Te surface atoms. All of the ILs show distinct surface layers at the solid surface; cations and anions are separated into

alternating layers penetrating deep into the bulk fluid. The simulated densities fluctuate very close to the experimental bulk densities, except in the case of $[\text{C}_2\text{mim}^+][\text{PF}_6^-]$, which is approximately 5% below the experimental value.

As mentioned previously, the exfoliation processes is aided by the ILs passivating the electrostatic interactions on the Bi_2Te_3 surfaces. The partial negative charges of the Te atoms at the surface of the quintuple layers make them susceptible to attack by the cation species (**Figure 2.4**). However, there are steric limitations that can prevent the initial IL intercalation. In order to more clearly investigate this aspect, we focus on the most effective IL, $[\text{C}_4\text{mim}^+][\text{Tf}_2\text{N}^-]$. We prepared 5 pairs of quintuple layers with different gap distances, ranging from 0.3 to 1.2 nm (defined as the distance between the center of mass of interface atoms (Te) in each quintuple layer). Each pair of these nanosheets is separated by a distance of 1.5 nm from the neighboring pair, and the nanosheets are restrained in their initial positions during the entire simulation.

From **Figure 2.4**, it is possible to identify the minimum gap between the Bi_2Te_3 nanosheets necessary to allow $[\text{C}_4\text{mim}^+][\text{Tf}_2\text{N}^-]$ IL penetration. At gap distances of 0.3 and 0.5 nm between Bi_2Te_3 interfaces, the IL molecules are not able to fully penetrate the gap. There is a small peak from the $[\text{C}_4\text{mim}^+]$ molecules, due to a slight amount of penetration from the butyl branch (the C_4 site in **Figure 2.5** (a)). At a gap distance of 0.7 nm, there is a strong peak in the IL density between the nanosheets. Although both anions and cations are detected within the slit, the cation density is much higher, and the narrow distance between solid surfaces shows a strong positive peak. As the gap grows (0.9 and 1.2 nm), the peaks become weaker but the number of IL layers increases from 1 to 2 at a Bi_2Te_3 separation distance of 1.2 nm. This is also reflected in the charge density profile in **Figure 2.4** (c), which shows the development of two individual positive peaks within the gap, corresponding to the two cation layers. It is also worth noting that at the

gap distance of 1.2 nm, the fluid structure (concentration and charge density) is already very similar to the structure at the opposite surface, in terms of peak heights and widths. Furthermore, the gap distance of 0.7 nm corresponds very closely to the approximate position of the initial exfoliation step in **Figure A2.17** ($0.7 \text{ nm} + 0.8 \text{ nm} = \sim 1.5 \text{ nm}$ center-of-mass distance). The strong solvent layering behavior between nanosheets has also been observed by others when exfoliating graphene and phosphorene.^{13,20}

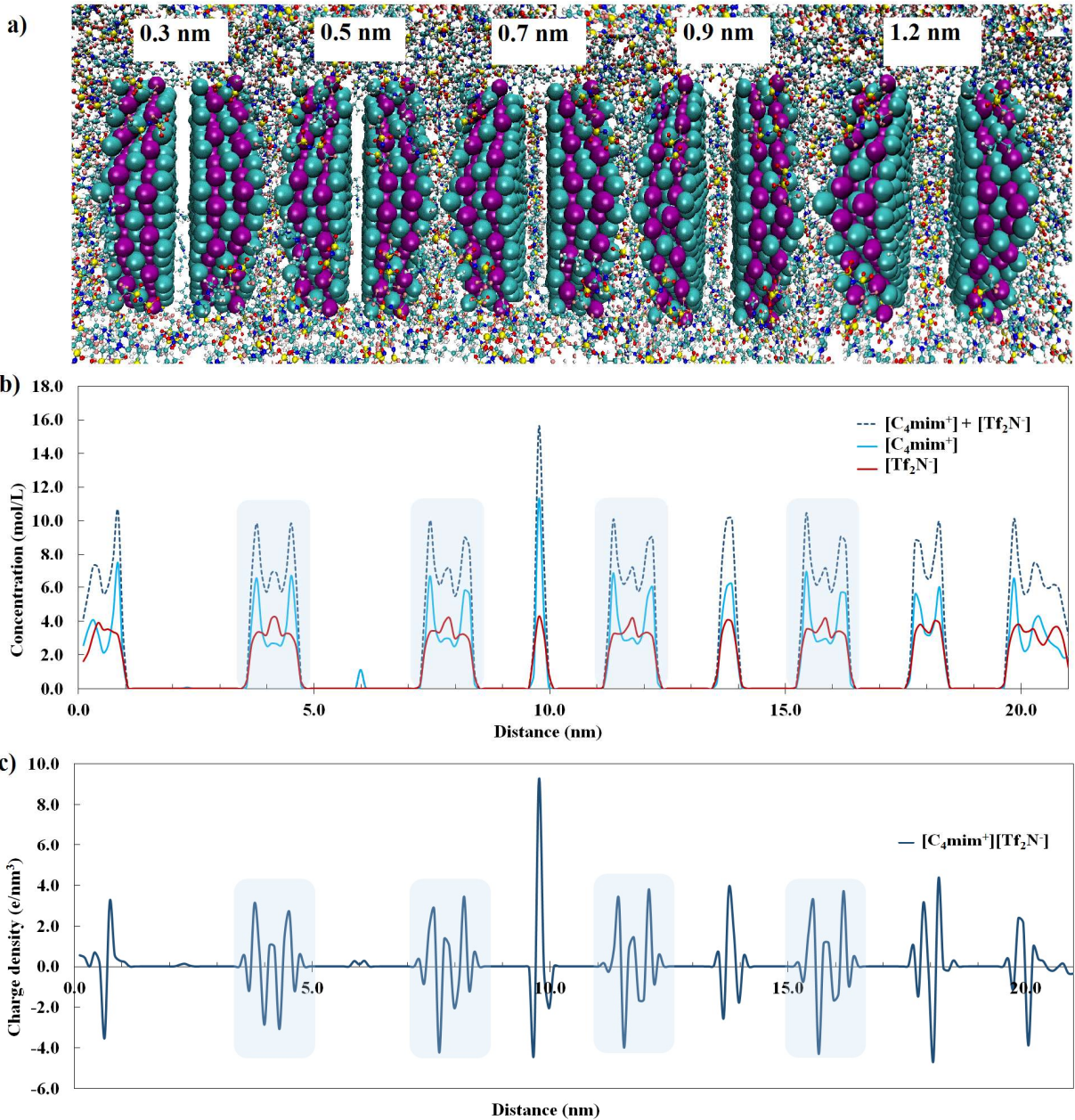


Figure 2.4. Cross-sectional analysis of a $[\text{C}_4\text{mim}^+][\text{Tf}_2\text{N}^-]$ solvent at 450 K for different COM distances between Bi_2Te_3 layers: (a) cross-sectional simulation view, (b) $[\text{C}_4\text{mim}^+]$ and $[\text{Tf}_2\text{N}^-]$ concentrations, and (c) $[\text{C}_4\text{mim}^+][\text{Tf}_2\text{N}^-]$ charge distribution. The highlighted sections represent the 1.5 nm gap between neighboring Bi_2Te_3 pairs.

2.5 Molecular Structure

In order to provide a more detailed analysis of the ILs at the Bi_2Te_3 interface, we calculated the density profile of specific atomic sites, molecular orientations, and charge distributions. In the density profile plots (**Figures 2.5-2.9**), the relevant atomic sites have been highlighted. Specifically, we track N of $[\text{Tf}_2\text{N}^+]$, P of $[\text{PF}_6^-]$, the center of mass of the imidazolium ring (in both $[\text{C}_4\text{mim}^+]$ and $[\text{C}_2\text{mim}^+]$), the terminal carbon of $[\text{C}_4\text{mim}^+]$ (C_4) and $[\text{C}_2\text{mim}^+]$ (C_2), as well as the short methyl branch of $[\text{C}_4\text{mim}^+]$ and $[\text{C}_2\text{mim}^+]$, labeled as (C_M). To calculate the number density of each site, only the density profile inside of the cylinder perpendicular and proportional to the size of the Bi_2Te_3 layer is included in the analysis (in order to eliminate edge effects that may arise from our Bi_2Te_3 model), and all data correspond to a temperature of 450 K.

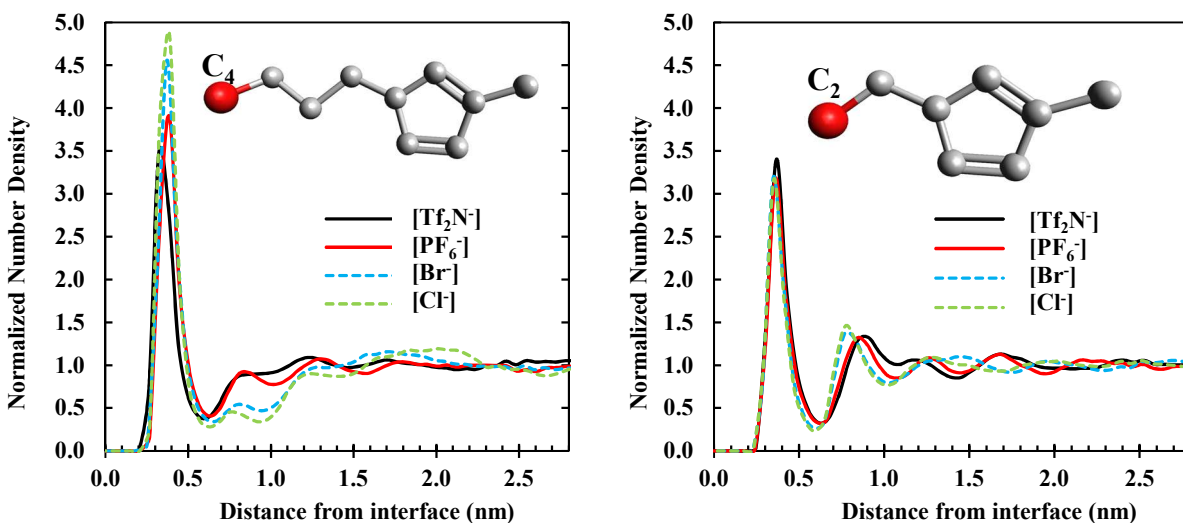


Figure 2.5. Normalized number density of long chain terminal carbon (C_2 , C_4) in different ILs at 450 K: (a) $[\text{C}_4\text{mim}^+]$ and (b) $[\text{C}_2\text{mim}^+]$.

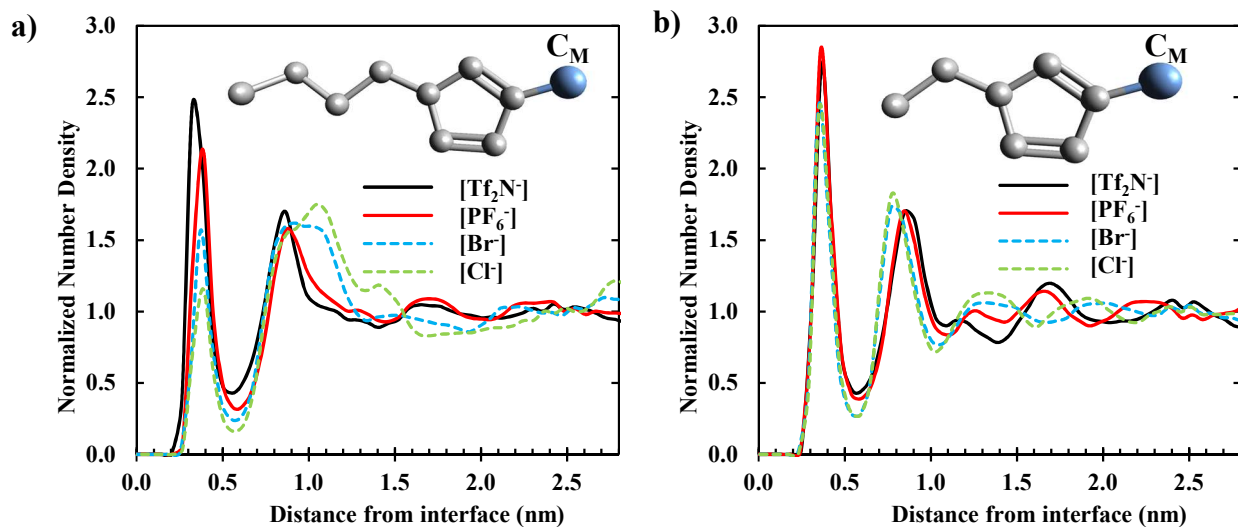


Figure 2.6. Normalized number density of short chain (C_M) carbon in different ILs at 450 K: (a) [C₄mim⁺] and (b) [C₂mim⁺].

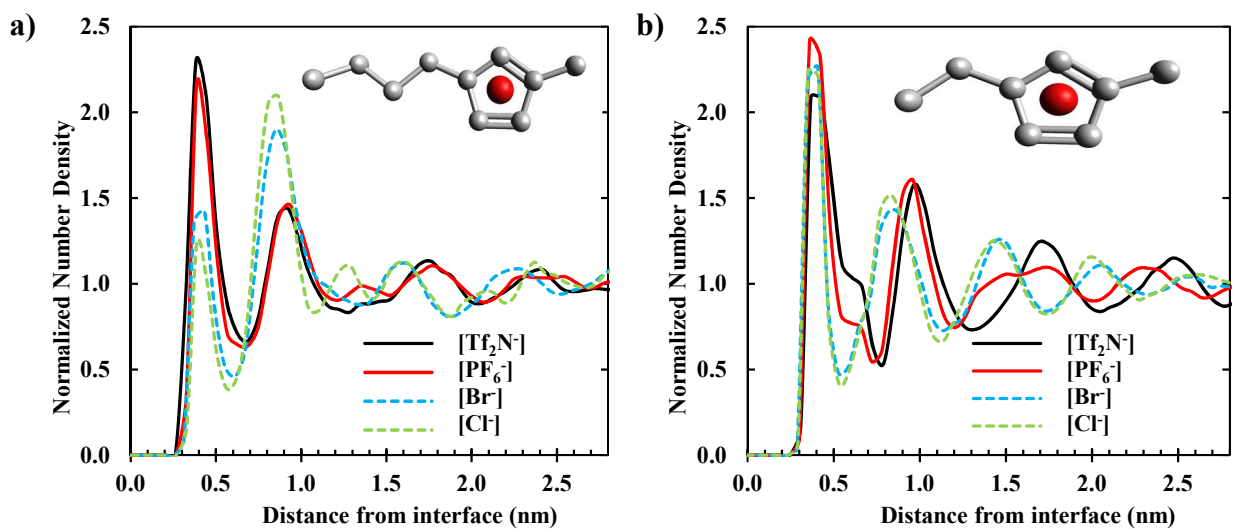


Figure 2.7. Normalized number density of imidazolium ring in different ILs at 450 K. Center of mass of ring (indicated as red sphere) has been chosen to represent ring number density: (a) [C₄mim⁺] and (b) [C₂mim⁺].

In **Figure 2.5** (a), we compare the normalized number density of the C₄ group among different [C₄mim⁺]-based ILs. The magnitude of the first peak (interfacing with the Bi₂Te₃ surface) is strongest with the [Cl⁻] and [Br⁻] anions. However, the behavior of these [C₄mim⁺]-based ILs is contrasted with the density profiles illustrated in **Figures 2.6** and **2.7**. In these two figures, the C_M group and the imidazole ring are shown to have much stronger interactions with the surface when paired with the [Tf₂N⁻] and [PF₆⁻] anions, while the interactions are weakened when paired with the [Cl⁻] and [Br⁻] anions. **Figure 2.6** and **2.7** show particularly interesting behavior, as the results with the [Br⁻] and [Cl⁻] anions show a depressed first layer density and an enhanced second layer density. This corroborates the very strong C₄ interaction with the surface, which tends to position more of the imidazole ring and C_M groups into the second interfacial layer. There is a moderate enhancement of the C₂ interaction with the surface when using the [Tf₂N⁻] and [PF₆⁻] anions (**Figure A2.21**). The density peaks are sharper and they are positioned closer to the Bi₂Te₃ surface.

In light of the enhanced exfoliation performance of the [Tf₂N⁻]-based ILs (and to some extent, the [PF₆⁻]-based ILs), the differences in interfacial structure suggest that the C_M group and the imidazole ring play a dominant role in the exfoliation process, versus direct interactions with the longer alkyl chains. In **Figures 2.5**, **2.6**, and **2.7**, the behavior of the [C₂mim⁺]-based ILs is also shown for comparison. The general interfacial structure is similar to the [C₄mim⁺]-based ILs, but there is less distinction between the peak heights when comparing the [C₂mim⁺] structure, when paired with different anions.

In addition to identifying the distribution of the atomic sites, we have also calculated the orientation of the imidazole rings at the interface. In **Figure 8**, we show the relative orientation of the imidazole ring with the surface (where θ corresponds to the angle between the plane of the

imidazole rings and the Bi_2Te_3 surface), and we distinguish molecules into first and second layer groups (according to the density profiles at the interface). There is significant ordering in the first layer, but very little ordering found in the second layer. In the first layer, the $[\text{C}_4\text{mim}^+][\text{Cl}^-]$ molecule is dominated by imidazole rings parallel to the surface. The $[\text{C}_4\text{mim}^+][\text{Tf}_2\text{N}^-]$ solvent is also predicted to favor a parallel orientation, but the effect is much less pronounced.

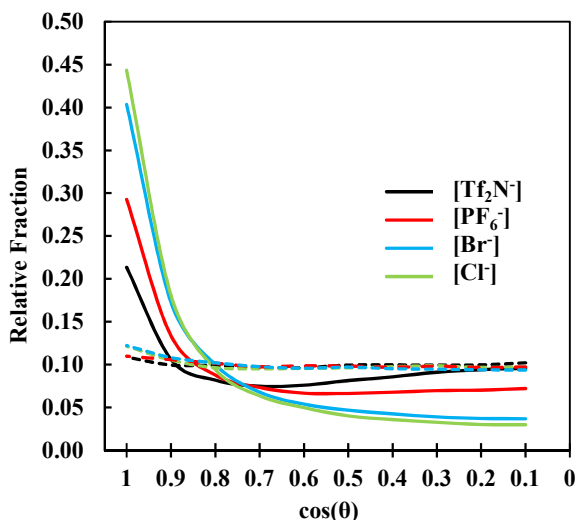


Figure 2.8. Ring angle distribution for $[\text{C}_4\text{mim}^+]$ -based ILs. Solid lines represent the first layer and the dashed lines represent second layer (as estimated from the density profiles).

Our structural analysis also shows strong differences in the anion distributions at the Bi_2Te_3 interface. **Figure 2.9** shows the anion number densities for the $[\text{C}_4\text{mim}^+]$ -based and $[\text{C}_2\text{mim}^+]$ -based ILs, and in both cases, the $[\text{Tf}_2\text{N}^-]$ anion has a particularly strong interaction at the interface. The first density peak is approximately 50% higher than the other anions, while the successive peaks are similar in height to the other compounds. The features of the $[\text{Br}^-]$ and $[\text{Cl}^-]$ curves are almost identical, while the $[\text{PF}_6^-]$ shows a peak splitting in the first layer.

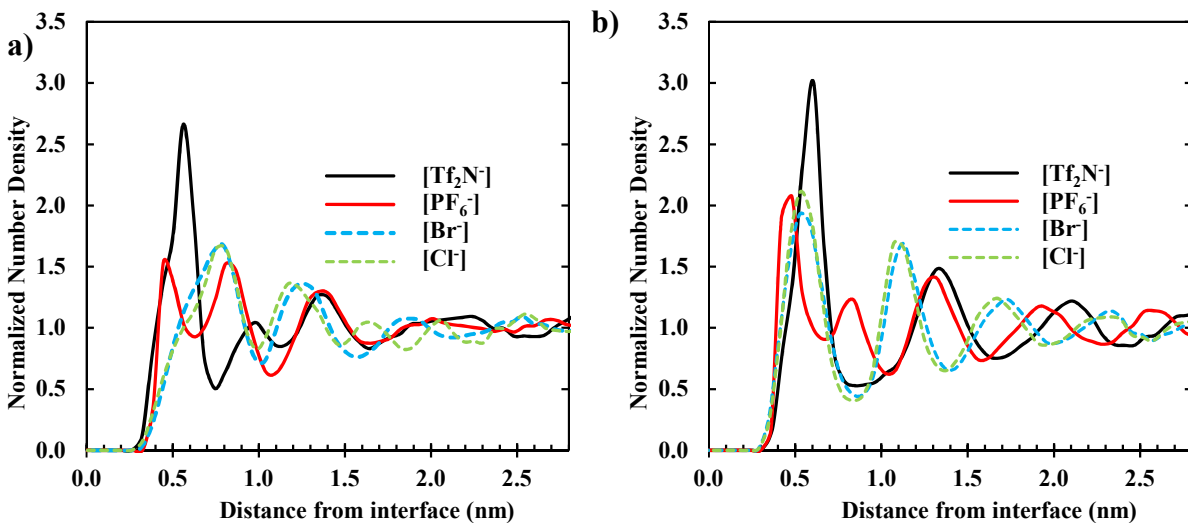


Figure 2.9. Normalized number density of anions in different ILs at 450 K. The nitrogen of $[\text{Tf}_2\text{N}^-]$ and the phosphorene of $[\text{PF}_6^-]$ have been chosen to represent these anion number densities: (a) $[\text{C}_4\text{mim}^+]$ and (b) $[\text{C}_2\text{mim}^+]$.

Finally, the combined effects of the cation and anion structure at the interface can lead to unique electrostatic solvation effects. Since the planar surfaces of the Bi_2Te_3 quintuple layers are negatively charged, the electrostatic interactions with the solvent can have a strong influence on the exfoliation. **Figure 2.10** shows the charge density at the Bi_2Te_3 surface with respect to the eight different IL solvents. Overall, the magnitude of the charge densities tend to be larger with the $[\text{C}_2\text{mim}^+]$ -based ILs, likely due to the smaller relative size versus the $[\text{C}_4\text{mim}^+]$ -based ILs, but the general structure of the $[\text{C}_2\text{mim}^+]$ -based and $[\text{C}_4\text{mim}^+]$ -based ILs is similar. As before, the results from the $[\text{Cl}^-]$ and $[\text{Br}^-]$ systems demonstrate very consistent features, in terms of charge density peak heights and layering, whereas the $[\text{Tf}_2\text{N}^-]$ and $[\text{PF}_6^-]$ are characteristically different. In $[\text{Tf}_2\text{N}^-]$ and $[\text{PF}_6^-]$ solvents, the charge density at the interface shows a very distinct double-layer structure, and it extends out to approximately 0.75 nm from the surface. Beyond this distance, the fluctuating charge density rapidly attenuates. Both the magnified double-layer

structure at the interface and the abrupt attenuation of the charge density at longer distances are unique to the $[\text{Tf}_2\text{N}^-]$ and $[\text{PF}_6^-]$ solvents. In our analysis of the charge density profiles, it should be noted that there are always ambiguities in the partial charge assignments that are used in the underlying forcefields. This translates into some inherent uncertainty in the predicted charge densities, as well as possible deviations from polarization effects (which are neglected in our models).

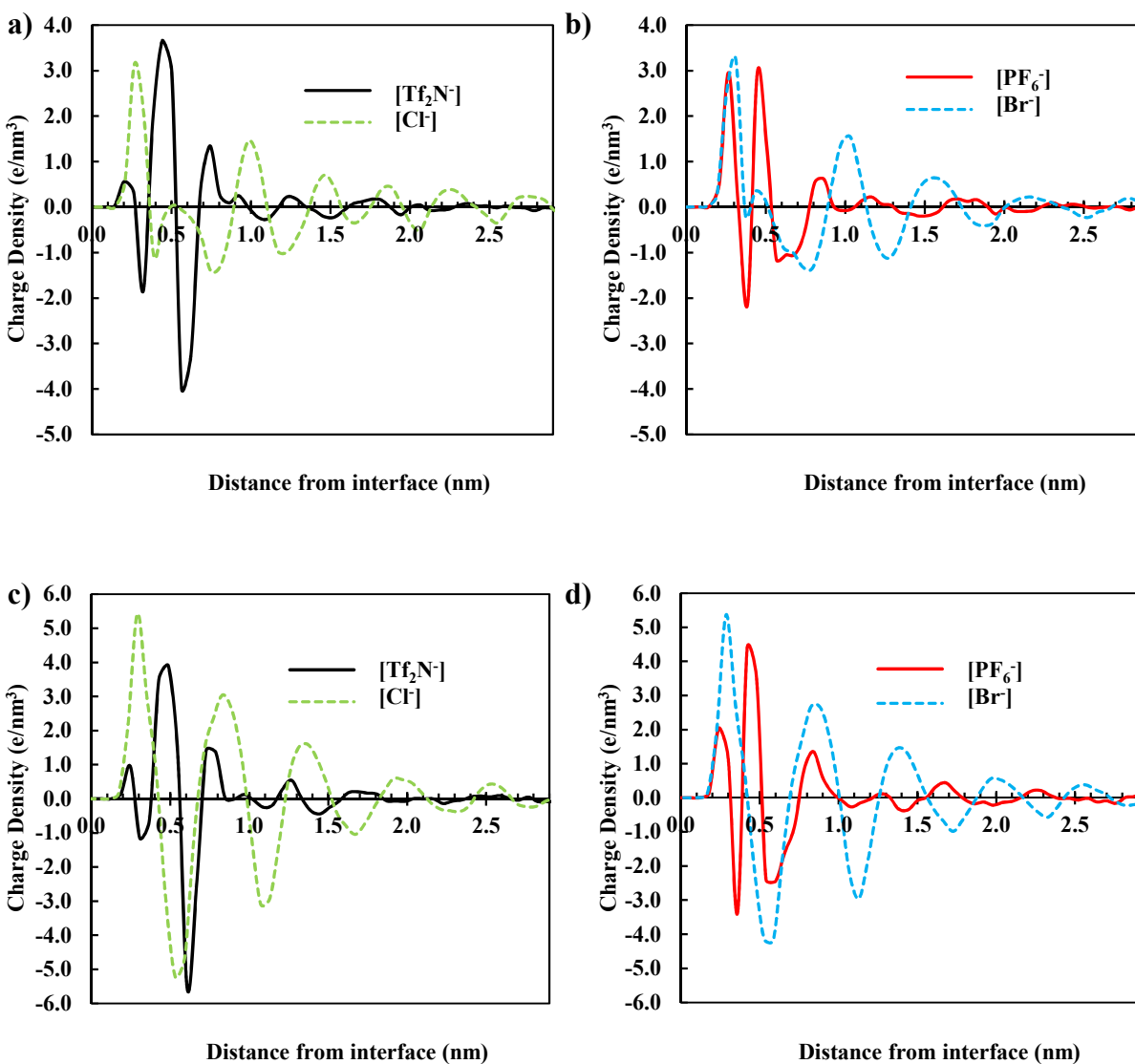


Figure 2.10. Charge distribution of ILs solvent at 450 K: (a,b) $[\text{C}_4\text{mim}^+]$ (c,d) $[\text{C}_2\text{mim}^+]$.

2.6 Conclusions

Eight different ionic liquids were evaluated as solvents for the exfoliation of Bi_2Te_3 nanosheets. A range of different temperatures were explored, falling within the general bounds of the melting temperature and decomposition temperature of the solvents (i.e., 350 K to 550 K). In order to evaluate the relative exfoliation energetics, three different exfoliation mechanisms were directly probed (pulling, shearing, and peeling) using steered molecular dynamics and calculating the potential of mean force.

With respect to the exfoliation energetics, the peeling mechanism is strongly preferred, as the exfoliated layer can be gradually passivated by the surrounding IL solvent. Due to the negatively-charged Te species, the cation molecules are strongly adsorbed at the planar Bi_2Te_3 solid-liquid interface. In addition, there are strong distinctions in the performance of the different IL solvents. Among the different cation ($[\text{C}_2\text{mim}^+]$, $[\text{C}_4\text{mim}^+]$) and anion ($[\text{Tf}_2\text{N}^-]$, $[\text{PF}_6^-]$, $[\text{Br}^-]$, $[\text{Cl}^-]$) pairs, the $[\text{Tf}_2\text{N}^-]$ -based solvents are predicted to be particularly effective for exfoliation, while there is only marginal distinction between the $[\text{C}_2\text{mim}^+]$ and $[\text{C}_4\text{mim}^+]$ behavior.

The differences in solvent performance can be correlated to the underlying molecular structures at the Bi_2Te_3 interface. While there are some exceptions, the performance of the $[\text{Tf}_2\text{N}^-]$ -based ILs is ranked highest, while that of the $[\text{Cl}^-]$ -based ILs is ranked lowest, and we find that the molecular features of these two solvent systems are characteristically different. For instance, the $[\text{Tf}_2\text{N}^-]$ anion induces much more tilt in the $[\text{C}_4\text{mim}^+]$ species at the interface (versus a much more planar configuration when paired with the $[\text{Cl}^-]$ anion). In addition, the normalized number density indicates a much higher $[\text{Tf}_2\text{N}^-]$ packing density in the first anion

layer at the interface (versus $[\text{Cl}^-]$). Also, when comparing $[\text{C}_4\text{mim}^+][\text{Tf}_2\text{N}^-]$ and $[\text{C}_4\text{mim}^+][\text{Cl}^-]$, the $[\text{Tf}_2\text{N}^-]$ anion gives rise to a strong interaction between the $[\text{C}_4\text{mim}^+]$ ring and methyl group (C_M site) with the Bi_2Te_3 surface, while $[\text{Cl}^-]$ anion leads to enhanced interaction between the cation tail (C_4 site) and the Bi_2Te_3 surface.

In summary, while our previous work (including experimental validation)¹⁶ highlighted the exfoliation of Bi_2Te_3 in $[\text{C}_4\text{mim}^+][\text{Cl}^-]$, our current study provides the motivation to test $[\text{Tf}_2\text{N}^-]$ -based ILs for accelerating the nanosheet dispersion. Furthermore, our work provides some of the molecular-level indicators of solvent performance, which may be useful for screening other potential solvents and/or for tuning the interactions between other ILs and layered dichalcogenide materials.

Acknowledgements

Support for this work provided by The University of Alabama Research Grants Committee and computer resources were provided by the Alabama Supercomputer Center.

Supporting Information

The Supporting Information is available in Appendix A. Molecular structures of the ILs and their physical properties. Detailed SMD simulation parameter selection corresponding to different solvents and exfoliation mechanisms. Normalized number density calculations at the IL- Bi_2Te_3 interface at temperatures of 450 K and 550 K. Additional density profiles of ILs at the Bi_2Te_3 interface.

Appendix A, Supporting Information for Chapter 2

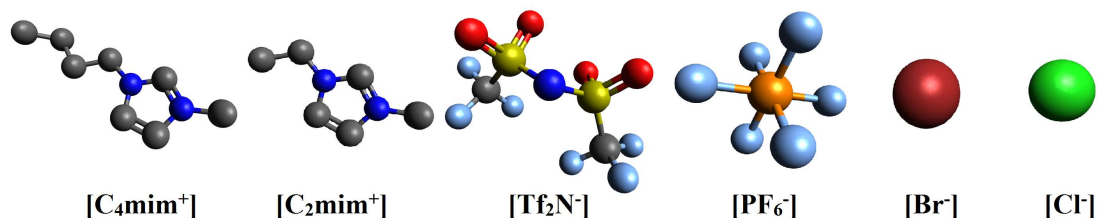


Figure A2.11. Chemical structure of 1-butyl-3-methylimidazolium $[C_4mim]^+$, 1-ethyl-3-methylimidazolium $[C_2mim]^+$, bis(trifluoromethylsulfonyl)imide $[Tf_2N]^-$, hexafluorophosphate $[PF_6]^-$, bromide $[Br]^-$, and chloride $[Cl]^-$ ions (N = navy, O = red, S = yellow, C = grey, F = light blue, P = orange, Br = dark red, Cl = green, and hydrogen atoms are omitted for clarity).

Table A2.1. Physical properties of ionic liquids: density (ρ) at corresponding temperature indicated in parenthesis, onset temperature of decomposition (T_d), melting temperature (T_m), and surface tension.

Compound	Densities (ρ) [g/cm ³]	T_d [K]	T_m [K]	Surface tension (25°C) [mN/m]
$[C_4mim]^+[Tf_2N]^-$	1.434 (304 K) ⁶¹	695 ⁶¹	271 ⁶¹	37.5 ⁶²
$[C_4mim]^+[PF_6]^-$	1.360 (298 K) ⁶²	622 ⁶²	283 ⁶²	48.8 ⁶²
$[C_4mim]^+[Br]^-$	1.300 (298 K) ⁶³	546 ⁶¹	338-348 ⁶⁴	--
$[C_4mim]^+[Cl]^-$	1.080 (298 K) ⁶²	537 ⁶¹	314 ⁶²	48.2 ³⁶
$[C_2mim]^+[Tf_2N]^-$	1.516 (304 K) ⁶¹	728 ⁶²	277 ⁶²	35.71 ⁶⁵
$[C_2mim]^+[PF_6]^-$	1.422 (352 K) ⁶⁶	648 ⁶²	331-333 ⁶²	--
$[C_2mim]^+[Br]^-$	--	584 ⁶⁷	350 ⁶⁷	--
$[C_2mim]^+[Cl]^-$	1.112 (353 K) ⁶⁸	558 ⁶²	357 ⁶⁹	--

Figure A2.12 compares different values of the spring stiffness during the Bi_2Te_3 pulling process in the $[\text{C}_4\text{mim}^+][\text{Tf}_2\text{N}^-]$ solvent for SMD simulation at 550 K. According to this figure, changing the spring stiffness only reduces the separation time. The maximum amount of force to separate the nanosheets in pulling simulations remains constant.

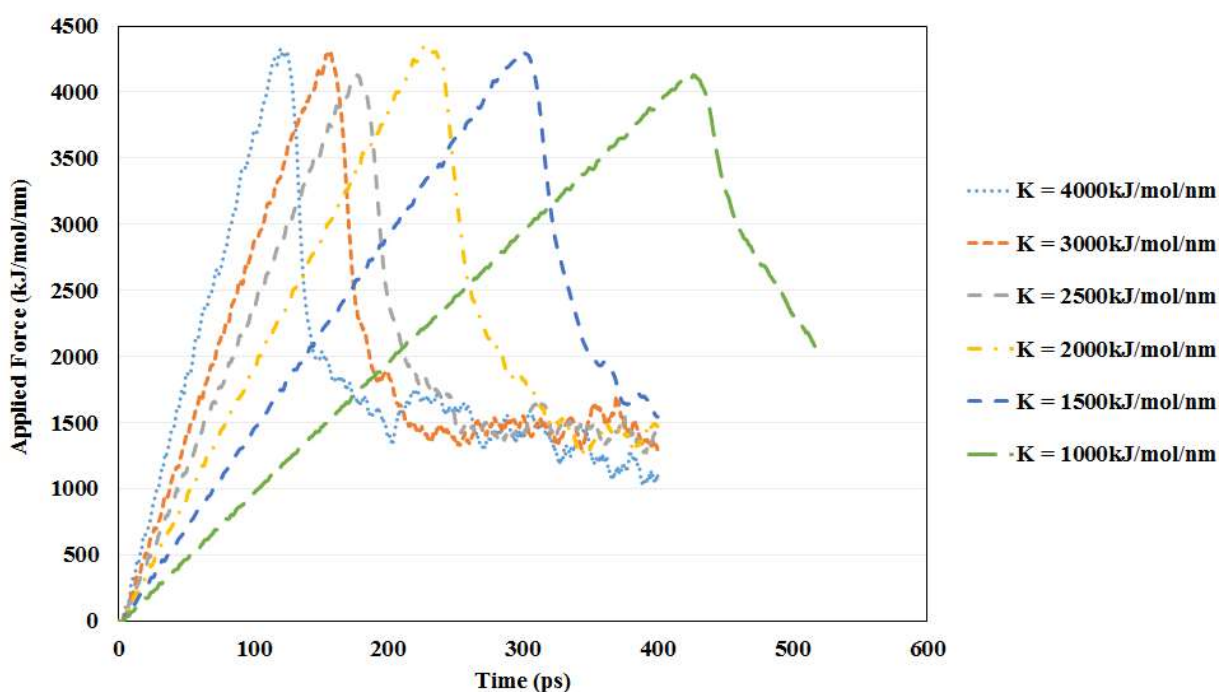


Figure A2.12. Force versus time for Bi_2Te_3 exfoliation in $[\text{C}_4\text{mim}^+][\text{Tf}_2\text{N}^-]$ solution at 550 K via the pulling process. The exfoliation rate for all cases is 0.01 nm/ps.

Figure A2.13 compares different separation velocities during the Bi_2Te_3 pulling process in a $[\text{C}_4\text{mim}^+][\text{Tf}_2\text{N}^-]$ solvent at 550 K. Higher separation velocities reduce the exfoliation time and change the maximum amount of initiation force. With higher separation velocities, the calculated spring force exceeds the required amount of exfoliation force. In addition, a high

separation velocity and high spring stiffness cause unwanted disturbances in the exfoliation trajectory.

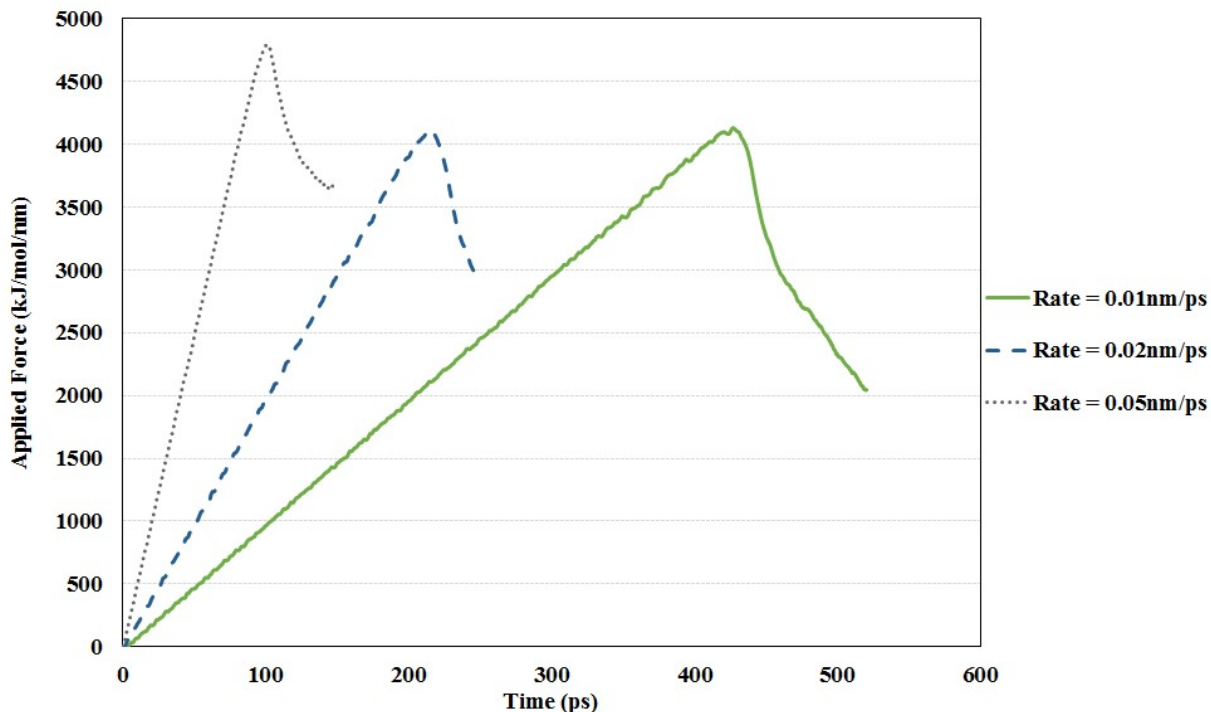


Figure A2.13. Force versus time for Bi_2Te_3 exfoliation in a $[\text{C}_4\text{mim}^+][\text{Tf}_2\text{N}^-]$ solvent at 550 K via the pulling mechanism. The spring stiffness for all cases is 1000 kJ/mol/nm.

To choose the most appropriate parameters for the spring stiffness and the separation velocity, we sampled different combinations of these parameters. A velocity of 0.002 nm/ps and a stiffness of 1000 kJ/mol/nm were chosen for the pulling mechanism, since these values led to a convergence of the maximum separation force (**Figure A2.14**). To calculate the most applicable exfoliation parameters for the peeling mechanism, two representative IL solvents were tested ($[\text{C}_4\text{mim}^+][\text{Tf}_2\text{N}^-]$ and $[\text{C}_4\text{mim}^+][\text{Cl}^-]$) at 450 K, as shown in **Figure A2.15** and **A2.16**. A velocity of 0.001 nm/ps and a spring stiffness of 500 kJ/mol/nm have been identified to perform best in the peeling and shearing simulations. Since the peeling process requires less force, the

exfoliation parameters (spring stiffness and velocity of separation) are reassigned different values.

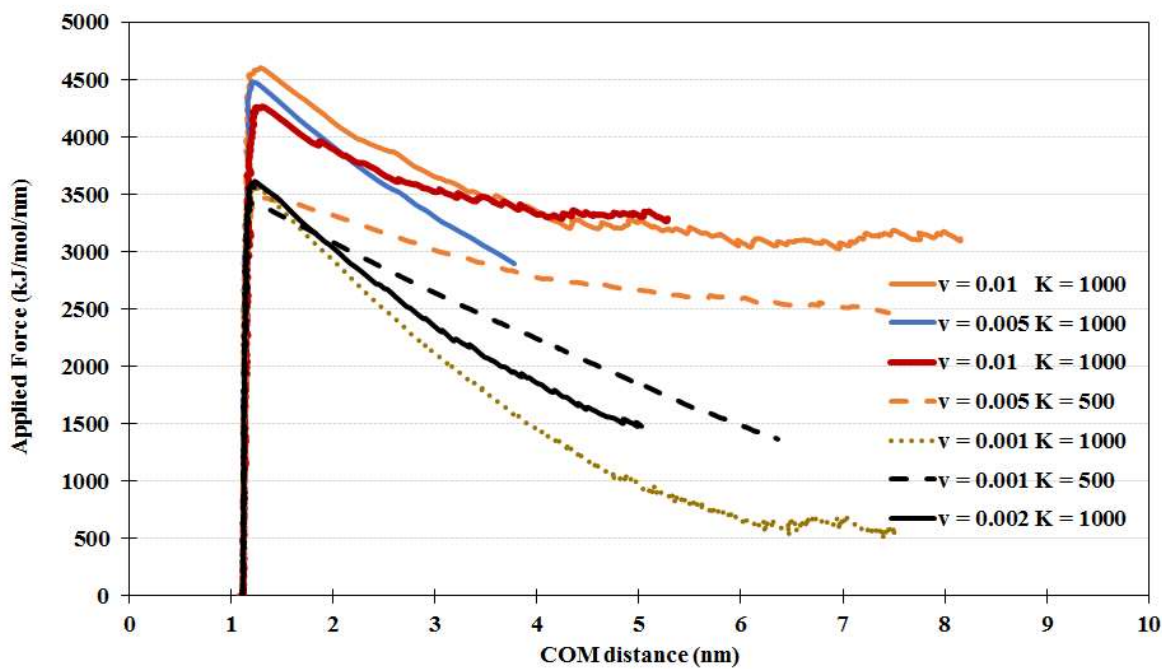


Figure A2.14. Force versus distance for the Bi_2Te_3 pulling mechanism in a $[\text{C}_4\text{mim}^+][\text{Tf}_2\text{N}^-]$ solvent at 450 K. The velocity (v) values are reported in units of nm/ps and the spring stiffness (K) values are reported in units of kJ/mol/nm.

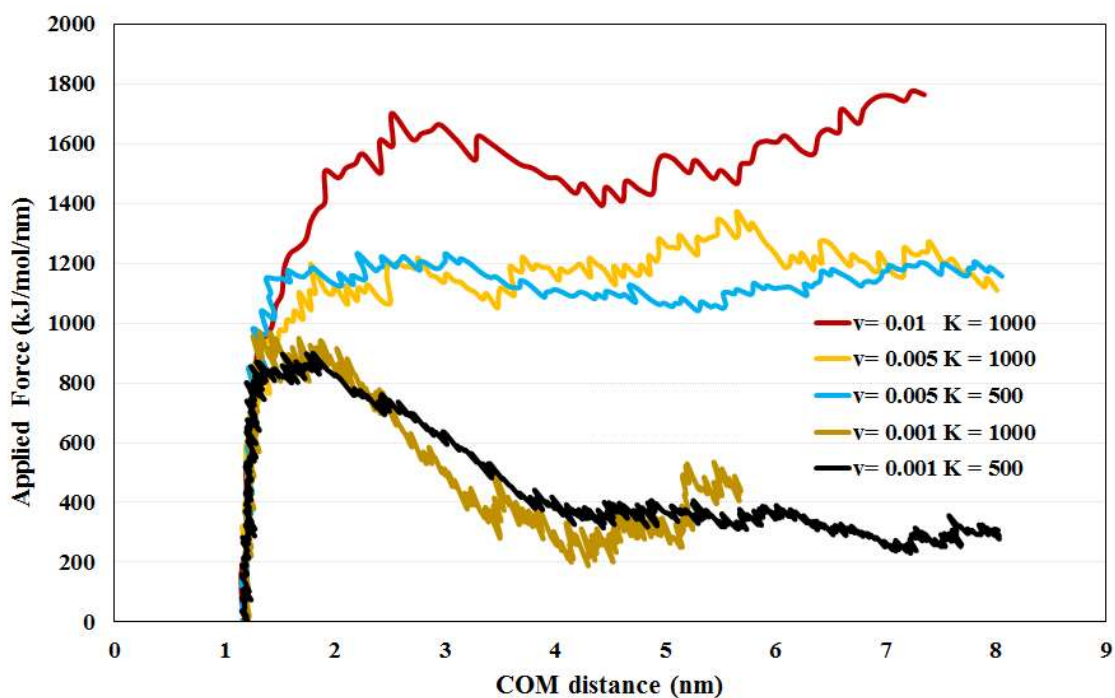


Figure A2.15. Force versus distance for the Bi_2Te_3 peeling mechanism in a $[\text{C}_4\text{mim}^+][\text{Tf}_2\text{N}^-]$ solvent at 450 K. The velocity (v) values are reported in units of nm/ps and the spring stiffness (K) values are reported in units of kJ/mol/nm.

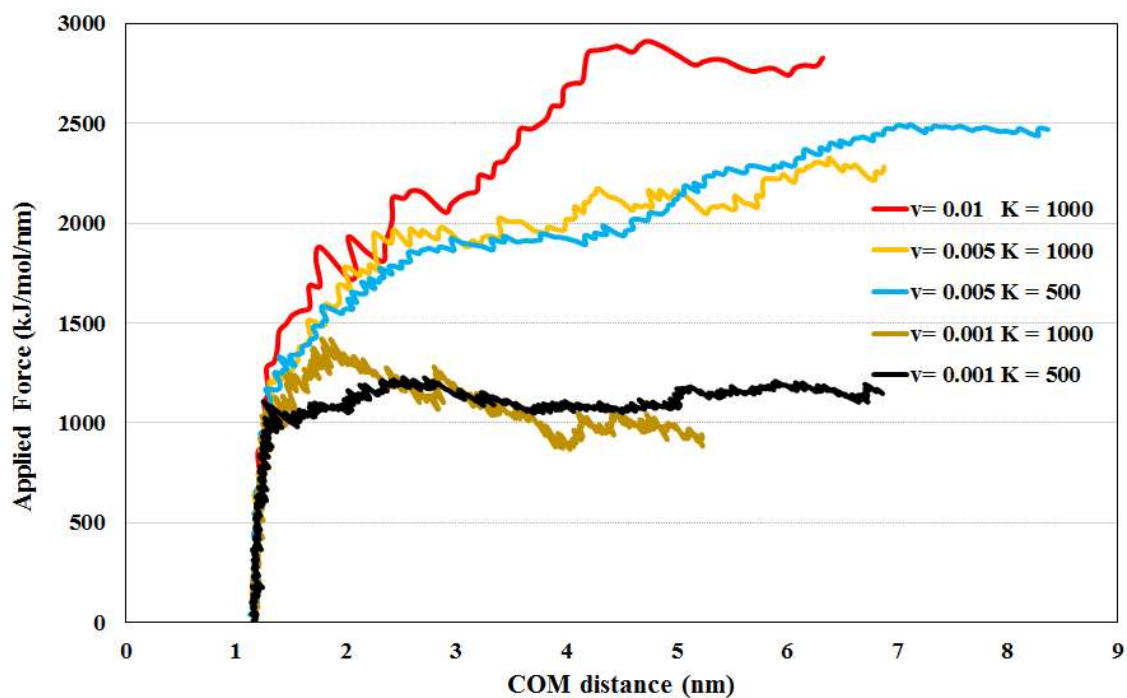


Figure A2.16. Force versus distance for the Bi_2Te_3 peeling mechanism in a $[\text{C}_4\text{mim}^+][\text{Cl}^-]$ solvent at 450 K. The velocity (v) values are reported in units of nm/ps and the spring stiffness (K) values are reported in units of kJ/mol/nm.

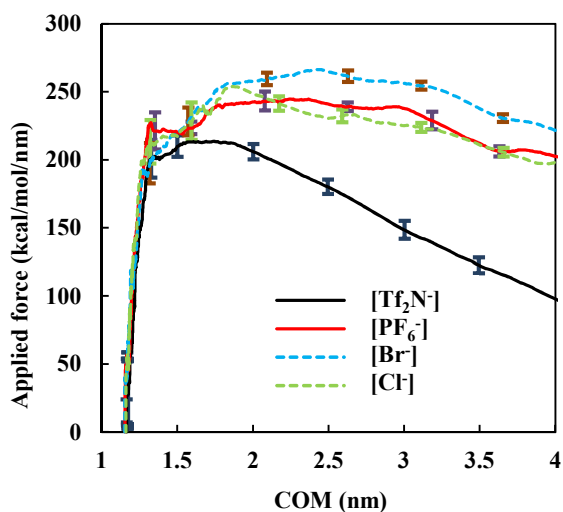


Figure A2.17. Force versus separation distance for the peeling mechanism in four different $[\text{C}_4\text{mim}^+]$ -based solvents at 450 K. Lines represent the average of 20 points, and the error bars indicate the standard deviation.

In **Figure A2.18**, the normalized number density for different ILs is reported at temperatures of 450 K and 550 K. The positions of the peaks are very similar at the two temperatures, and the peak heights are slightly reduced at the higher temperature.

The density profiles of the ILs are compared with the bulk experimental density values in **Figures A2.19, A2.20**. To the best of our knowledge, the experimental density for pure $[\text{C}_4\text{mim}^+][\text{Br}^-]$ is not available in the literature.

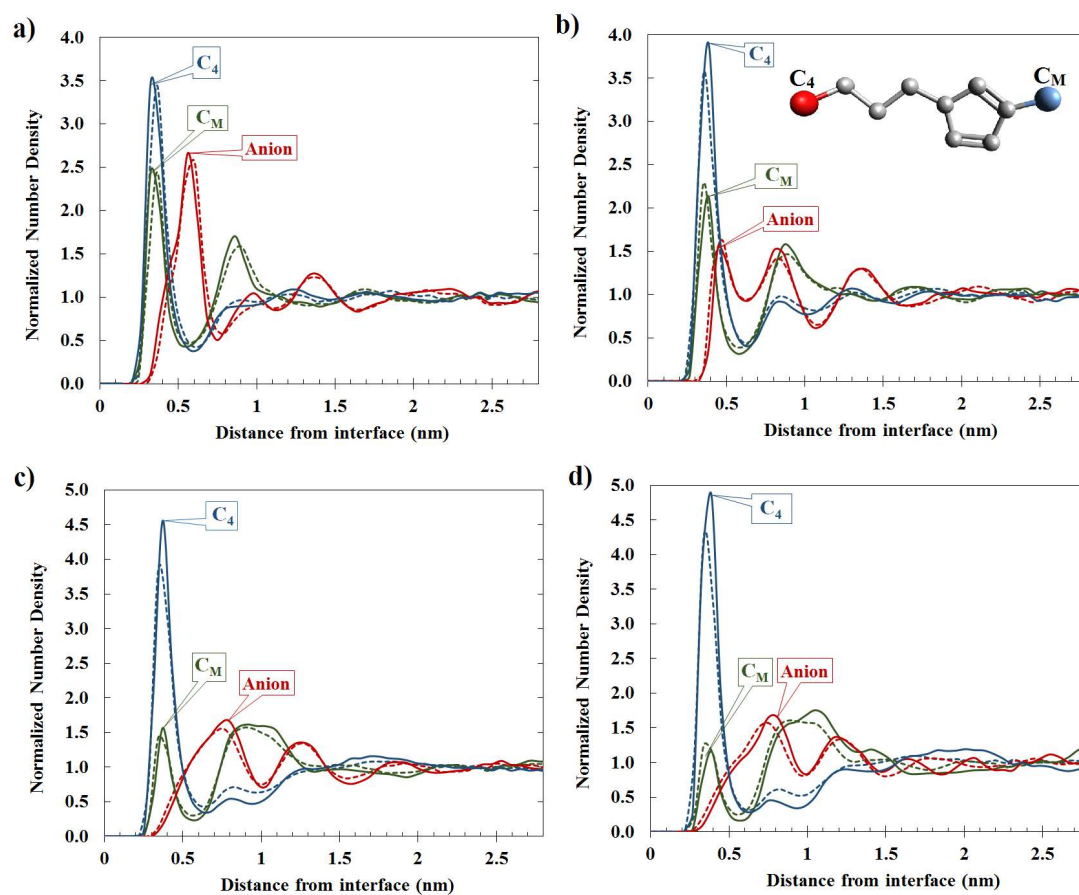


Figure A2.18. Normalized number density for selected atoms of: a) $[\text{C}_4\text{mim}^+][\text{Tf}_2\text{N}^-]$, b) $[\text{C}_4\text{mim}^+][\text{PF}_6^-]$, c) $[\text{C}_4\text{mim}^+][\text{Br}^-]$, d) $[\text{C}_4\text{mim}^+][\text{Cl}^-]$. The solid line corresponds to 450 K and the dashed line corresponds to 550 K.

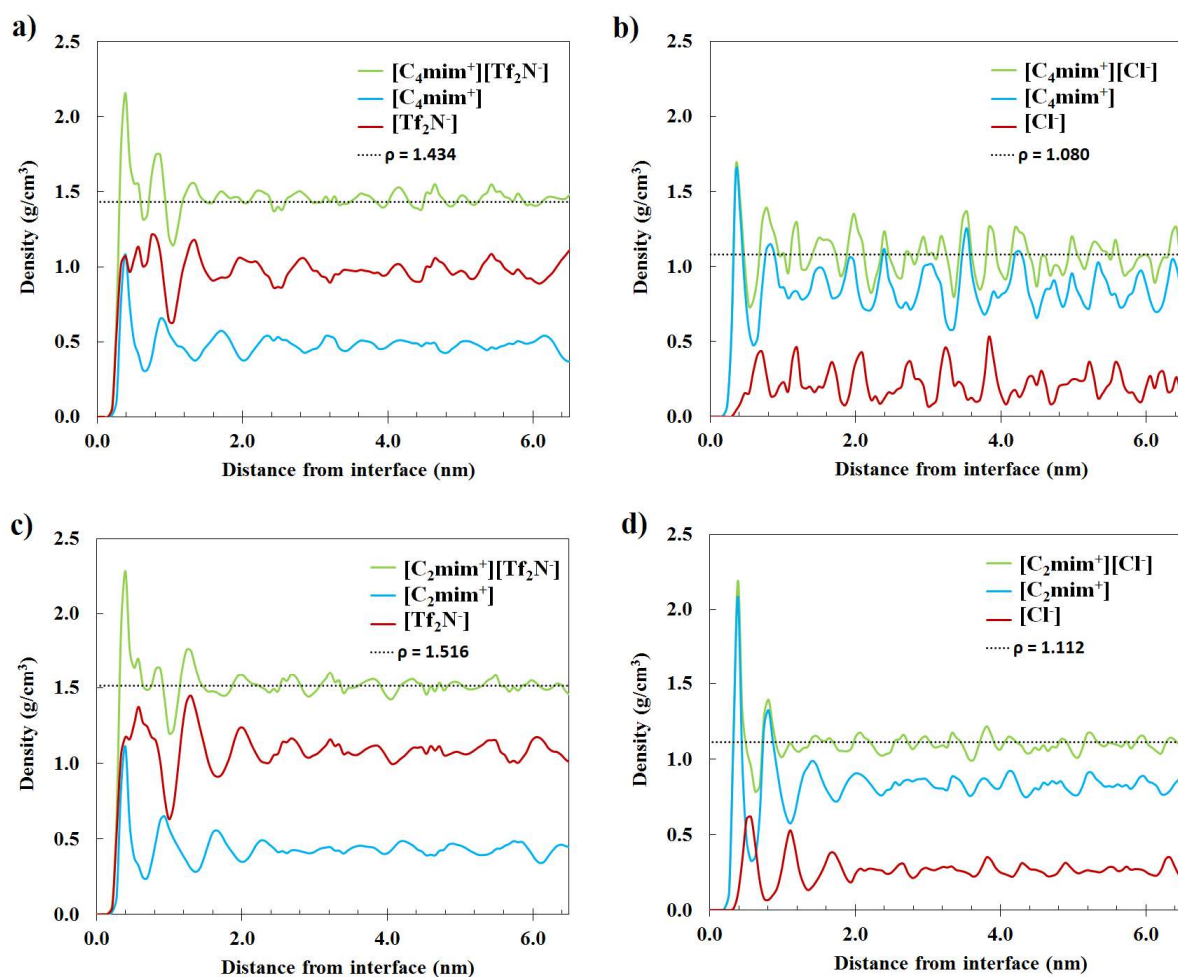


Figure A2.19. Calculated densities of ILs versus experiments at: (a) 304 K for $[\text{C}_4\text{mim}^+][\text{Tf}_2\text{N}^-]$, (b) 298 K for $[\text{C}_4\text{mim}^+][\text{Cl}^-]$, (c) 304 K for $[\text{C}_2\text{mim}^+][\text{Tf}_2\text{N}^-]$, and (d) 353 K for $[\text{C}_2\text{mim}^+][\text{Cl}^-]$. The dashed lines represent the experimental data.

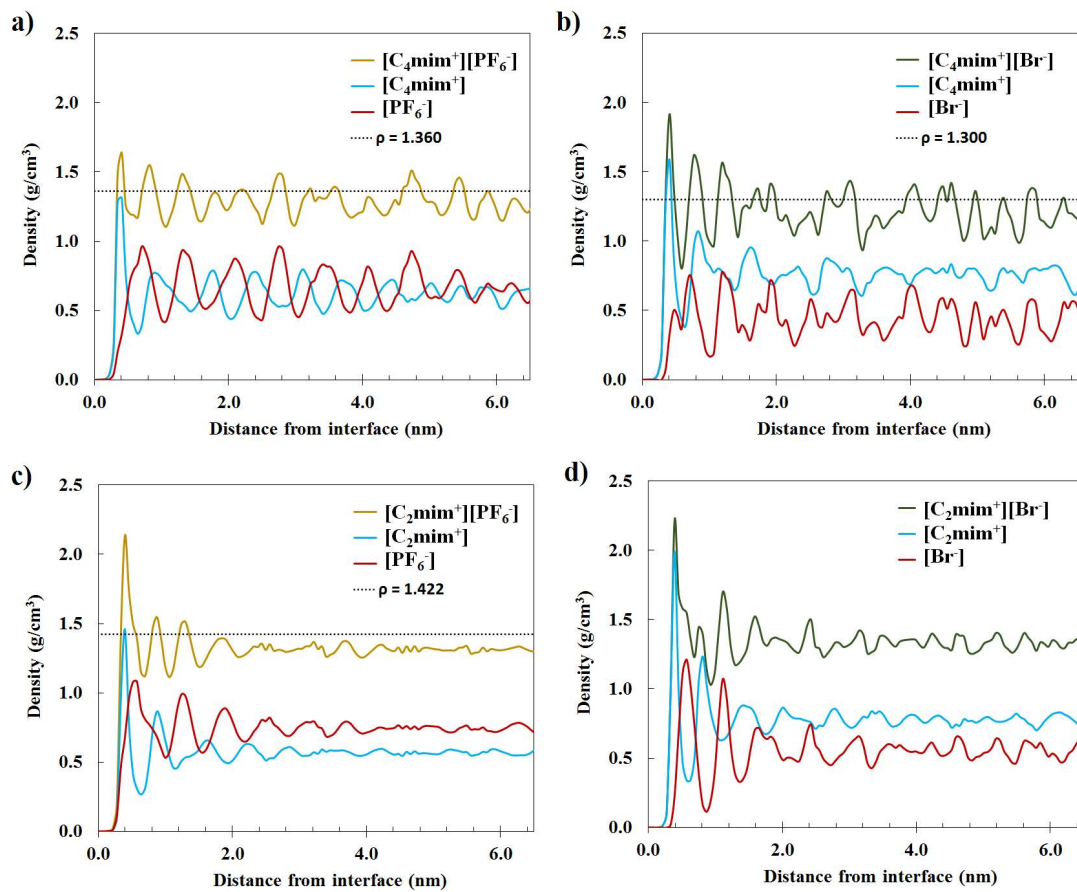


Figure A2.20. Calculated density profiles of different ILs at the Bi_2Te_3 interface vs. the bulk experimental density values: a) $[\text{C}_4\text{mim}^+][\text{PF}_6^-]$ at 298 K, b) $[\text{C}_4\text{mim}^+][\text{Br}^-]$ at 298 K c) $[\text{C}_2\text{mim}^+][\text{PF}_6^-]$ at 352 K, and d) $[\text{C}_2\text{mim}^+][\text{Br}^-]$ at 353 K. The dashed lines represent the bulk experimental densities.

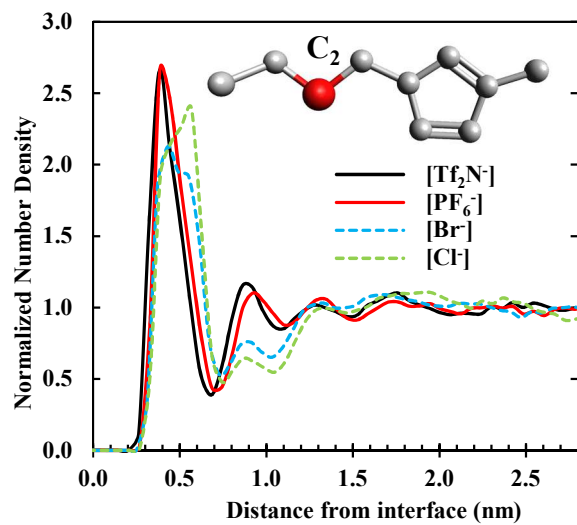


Figure A2.21. Normalized number density of C₂ carbon in [C₄mim⁺] structure at 450 K.

References

- (1) Fei, F.; Wei, Z.; Wang, Q.; Lu, P.; Wang, S.; Qin, Y.; Pan, D.; Zhao, B.; Wang, X.; Sun, J.; Wang, X.; Wang, P.; Wan, J.; Zhou, J.; Han, M.; Song, F.; Wang, B.; Wang, G. Solvothermal Synthesis of Lateral Heterojunction $\text{Sb}_2\text{Te}_3/\text{Bi}_2\text{Te}_3$ Nanoplates. *Nano Lett.* **2015**, *15*, 5905-5911.
- (2) Mishra, S. K.; Satpathy, S.; Jepsen, O. Electronic structure and thermoelectric properties of bismuth telluride and bismuth selenide. *J. Phys-Condens Mat.* **1997**, *9*, 461-470.
- (3) Yin, K.; Cui, Z. D.; Zheng, X. R.; Yang, X. J.; Zhu, S. L.; Li, Z. Y.; Liang, Y. Q. A $\text{Bi}_2\text{Te}_3@\text{CoNiMo}$ composite as a high performance bifunctional catalyst for hydrogen and oxygen evolution reactions. *J. Mater. Chem. A* **2015**, *3*, 22770-22780.
- (4) Sung, J. H.; Heo, H.; Hwang, I.; Lim, M.; Lee, D.; Kang, K.; Choi, H. C.; Park, J. H.; Jhi, S. H.; Jo, M. H. Atomic layer-by-layer thermoelectric conversion in topological insulator bismuth/antimony tellurides. *Nano Lett.* **2014**, *14*, 4030-4035.
- (5) Teweldebrhan, D.; Goyal, V.; Rahman, M.; Balandin, A. A. Atomically-thin crystalline films and ribbons of bismuth telluride. *Appl. Phys. Lett.* **2010**, *96*, 053107.
- (6) Kong, D.; Dang, W.; Cha, J. J.; Li, H.; Meister, S.; Peng, H.; Liu, Z.; Cui, Y. Few-layer nanoplates of Bi_2Se_3 and Bi_2Te_3 with highly tunable chemical potential. *Nano Lett.* **2010**, *10*, 2245-2250.
- (7) Guo, L.; Ivey, B. C.; Aglan, A.; Tang, C.; Song, J.; Turner, C. H.; Frazier, R. M.; Gupta, A.; Wang, H. T. Vapor Phase Growth of Bismuth Telluride Nanoplatelets on Flexible Polyimide Films. *ECS Solid State Lett.* **2012**, *2*, P19-P21.
- (8) Wang, D.; Yu, D.; Mo, M.; Liu, X.; Qian, Y. Preparation and characterization of wire-like Sb_2Se_3 and flake-like Bi_2Se_3 nanocrystals. *J. Cryst. Growth* **2003**, *253*, 445-451.
- (9) Wang, W. Z.; Poudel, B.; Yang, J.; Wang, D. Z.; Ren, Z. F. High-yield synthesis of single-crystalline antimony telluride hexagonal nanoplates using a solvothermal approach. *J. Am. Chem. Soc.* **2005**, *127*, 13792-13793.
- (10) Niu, L.; Coleman, J. N.; Zhang, H.; Shin, H.; Chhowalla, M.; Zheng, Z. Production of Two-Dimensional Nanomaterials via Liquid-Based Direct Exfoliation. *Small* **2016**, *12*, 272-293.
- (11) Dias, A.; Lima, S.; Carriazo, D.; Rives, V.; Pillinger, M.; Valente, A. Exfoliated titanate, niobate and titanoniobate nanosheets as solid acid catalysts for the liquid-phase dehydration of d-xylose into furfural. *J. Catal.* **2006**, *244*, 230-237.
- (12) Hernandez, Y.; Nicolosi, V.; Lotya, M.; Blighe, F. M.; Sun, Z.; De, S.; McGovern, I. T.; Holland, B.; Byrne, M.; Gun'ko, Y. K.; Boland, J. J.; Niraj, P.; Duesberg, G.; Krishnamurthy, S.; Goodhue, R.; Hutchison, J.; Scardaci, V.; Ferrari, A. C.; Coleman, J. N. High-yield production of graphene by liquid-phase exfoliation of graphite. *Nat. Nanotechnol.* **2008**, *3*, 563-568.
- (13) Shih, C. J.; Lin, S. C.; Strano, M. S.; Blankschtein, D. Understanding the Stabilization of Liquid-Phase-Exfoliated Graphene in Polar Solvents: Molecular Dynamics Simulations and Kinetic Theory of Colloid Aggregation. *J. Am. Chem. Soc.* **2010**, *132*, 14638-14648.
- (14) Zhi, C.; Bando, Y.; Tang, C.; Kuwahara, H.; Golberg, D. Large-Scale Fabrication of Boron Nitride Nanosheets and Their Utilization in Polymeric Composites with Improved Thermal and Mechanical Properties. *Adv. Mater.* **2009**, *21*, 2889-2893.
- (15) Morishita, T.; Okamoto, H.; Katagiri, Y.; Matsushita, M.; Fukumori, K. A high-yield ionic liquid-promoted synthesis of boron nitride nanosheets by direct exfoliation. *Chem. Commun. (Camb)* **2015**, *51*, 12068-12071.

- (16) Ludwig, T.; Guo, L.; McCrary, P.; Zhang, Z.; Gordon, H.; Quan, H.; Stanton, M.; Frazier, R. M.; Rogers, R. D.; Wang, H. T.; Turner, C. H. Mechanism of bismuth telluride exfoliation in an ionic liquid solvent. *Langmuir* **2015**, *31*, 3644-3652.
- (17) Coleman, J. N.; Lotya, M.; O'Neill, A.; Bergin, S. D.; King, P. J.; Khan, U.; Young, K.; Gaucher, A.; De, S.; Smith, R. J.; Shvets, I. V.; Arora, S. K.; Stanton, G.; Kim, H. Y.; Lee, K.; Kim, G. T.; Duesberg, G. S.; Hallam, T.; Boland, J. J.; Wang, J. J.; Donegan, J. F.; Grunlan, J. C.; Moriarty, G.; Shmeliov, A.; Nicholls, R. J.; Perkins, J. M.; Grieveson, E. M.; Theuvsissen, K.; McComb, D. W.; Nellist, P. D.; Nicolosi, V. Two-dimensional nanosheets produced by liquid exfoliation of layered materials. *Science* **2011**, *331*, 568-571.
- (18) Zheng, J.; Zhang, H.; Dong, S.; Liu, Y.; Nai, C. T.; Shin, H. S.; Jeong, H. Y.; Liu, B.; Loh, K. P. High yield exfoliation of two-dimensional chalcogenides using sodium naphthalenide. *Nat. Commun.* **2014**, *5*, 2995.
- (19) Yasaei, P.; Kumar, B.; Foroozan, T.; Wang, C.; Asadi, M.; Tuschel, D.; Indacochea, J. E.; Klie, R. F.; Salehi-Khojin, A. High-quality black phosphorus atomic layers by liquid-phase exfoliation. *Adv. Mater.* **2015**, *27*, 1887-1892.
- (20) Sresht, V.; Padua, A. A. H.; Blankschtein, D. Liquid-Phase Exfoliation of Phosphorene: Design Rules from Molecular Dynamics Simulations. *Acs Nano* **2015**, *9*, 8255-8268.
- (21) Hanlon, D.; Backes, C.; Doherty, E.; Cucinotta, C. S.; Berner, N. C.; Boland, C.; Lee, K.; Harvey, A.; Lynch, P.; Gholamvand, Z.; Zhang, S.; Wang, K.; Moynihan, G.; Pokle, A.; Ramasse, Q. M.; McEvoy, N.; Blau, W. J.; Wang, J.; Abellan, G.; Hauke, F.; Hirsch, A.; Sanvito, S.; O'Regan, D. D.; Duesberg, G. S.; Nicolosi, V.; Coleman, J. N. Liquid exfoliation of solvent-stabilized few-layer black phosphorus for applications beyond electronics. *Nat. Commun.* **2015**, *6*, 8563.
- (22) Sutto, T. E.; Duncan, T. T. The intercalation behavior of ionic liquids in the layered metal dichalcogenide TiS_2 . *Electrochim. Acta* **2012**, *77*, 204-211.
- (23) Wilkes, J. S. A short history of ionic liquids—from molten salts to neoteric solvents. *Green Chem.* **2002**, *4*, 73-80.
- (24) Capello, C.; Fischer, U.; Hungerbühler, K. What is a green solvent? A comprehensive framework for the environmental assessment of solvents. *Green Chem.* **2007**, *9*, 927.
- (25) Dilip, M. Cradle to grave: How green are ionic liquids? *Nanomaterials and Energy* **2012**, *1*, 193-206.
- (26) Sato, T.; Masuda, G.; Takagi, K. Electrochemical properties of novel ionic liquids for electric double layer capacitor applications. *Electrochim. Acta* **2004**, *49*, 3603-3611.
- (27) Wei, D.; Ivaska, A. Applications of ionic liquids in electrochemical sensors. *Anal. Chim. Acta* **2008**, *607*, 126-135.
- (28) Capozza, R.; Benassi, A.; Vanossi, A.; Tosatti, E. Electrical charging effects on the sliding friction of a model nano-confined ionic liquid. *J. Chem. Phys.* **2015**, *143*, 144703.
- (29) Black, J. M.; Baris Okatan, M.; Feng, G.; Cummings, P. T.; Kalinin, S. V.; Balke, N. Topological defects in electric double layers of ionic liquids at carbon interfaces. *Nano Energy* **2015**, *15*, 737-745.
- (30) Black, J. M.; Walters, D.; Labuda, A.; Feng, G.; Hillesheim, P. C.; Dai, S.; Cummings, P. T.; Kalinin, S. V.; Proksch, R.; Balke, N. Bias-dependent molecular-level structure of electrical double layer in ionic liquid on graphite. *Nano Lett.* **2013**, *13*, 5954-5960.
- (31) Lopes, J. N. C.; Deschamps, J.; Padua, A. A. H. Modeling ionic liquids using a systematic all-atom force field. *J. Phys. Chem. B* **2004**, *108*, 2038-2047.

- (32) Shah, J. K.; Brennecke, J. F.; Maginn, E. J. Thermodynamic properties of the ionic liquid 1-n-butyl-3-methylimidazolium hexafluorophosphate from Monte Carlo simulations. *Green Chem.* **2002**, *4*, 112-118.
- (33) Kamath, G.; Baker, G. A. In silico free energy predictions for ionic liquid-assisted exfoliation of a graphene bilayer into individual graphene nanosheets. *Phys. Chem. Chem. Phys.* **2012**, *14*, 7929-7933.
- (34) Kamath, G.; Baker, G. A. Are ionic liquids suitable media for boron nitride exfoliation and dispersion? Insight via molecular dynamics. *RSC Adv.* **2013**, *3*, 8197.
- (35) Wilkes, J. S.; Zaworotko, M. J. Air and Water Stable 1-Ethyl-3-Methylimidazolium Based Ionic Liquids. *J. Chem. Soc. Chem. Comm.* **1992**, 965-967.
- (36) Tariq, M.; Freire, M. G.; Saramago, B.; Coutinho, J. A.; Lopes, J. N.; Rebelo, L. P. Surface tension of ionic liquids and ionic liquid solutions. *Chem. Soc. Rev.* **2012**, *41*, 829-868.
- (37) Vatamanu, J.; Bedrov, D. Capacitive Energy Storage: Current and Future Challenges. *J. Phys. Chem. Lett.* **2015**, *6*, 3594-3609.
- (38) Federici Canova, F.; Mizukami, M.; Imamura, T.; Kurihara, K.; Shluger, A. L. Structural stability and polarisation of ionic liquid films on silica surfaces. *Phys. Chem. Chem. Phys.* **2015**, *17*, 17661-17669.
- (39) Wang, Y. L.; Laaksonen, A. Interfacial structure and orientation of confined ionic liquids on charged quartz surfaces. *Phys. Chem. Chem. Phys.* **2014**, *16*, 23329-23339.
- (40) Van Der Spoel, D.; Lindahl, E.; Hess, B.; Groenhof, G.; Mark, A. E.; Berendsen, H. J. GROMACS: fast, flexible, and free. *J. Comput. Chem.* **2005**, *26*, 1701-1718.
- (41) Jorgensen, W. L.; Maxwell, D. S.; TiradoRives, J. Development and testing of the OPLS all-atom force field on conformational energetics and properties of organic liquids. *J. Am. Chem. Soc.* **1996**, *118*, 11225-11236.
- (42) Qiu, B.; Ruan, X. Molecular dynamics simulations of lattice thermal conductivity of bismuth telluride using two-body interatomic potentials. *Phys. Rev. B* **2009**, *80*.
- (43) Rappe, A. K.; Casewit, C. J.; Colwell, K. S.; Goddard, W. A.; Skiff, W. M. Uff, a Full Periodic-Table Force-Field for Molecular Mechanics and Molecular-Dynamics Simulations. *J. Am. Chem. Soc.* **1992**, *114*, 10024-10035.
- (44) Essmann, U.; Perera, L.; Berkowitz, M. L.; Darden, T.; Lee, H.; Pedersen, L. G. A smooth particle mesh Ewald method. *J. Chem. Phys.* **1995**, *103*, 8577-8593.
- (45) Parrinello, M. Polymorphic transitions in single crystals: A new molecular dynamics method. *J. Appl. Phys.* **1981**, *52*, 7182.
- (46) Parrinello, M.; Rahman, A. Crystal Structure and Pair Potentials: A Molecular-Dynamics Study. *Phys. Rev. Lett.* **1980**, *45*, 1196-1199.
- (47) Hoover, W. G. Canonical dynamics: Equilibrium phase-space distributions. *Phys. Rev. A* **1985**, *31*, 1695-1697.
- (48) Martinez, L.; Andrade, R.; Birgin, E. G.; Martinez, J. M. PACKMOL: a package for building initial configurations for molecular dynamics simulations. *J. Comput. Chem.* **2009**, *30*, 2157-2164.
- (49) Balsera, M.; Stepaniants, S.; Izrailev, S.; Oono, Y.; Schulten, K. Reconstructing potential energy functions from simulated force-induced unbinding processes. *Biophys. J.* **1997**, *73*, 1281-1287.
- (50) Lemkul, J. A.; Bevan, D. R. Assessing the Stability of Alzheimer's Amyloid Protofibrils Using Molecular Dynamics. *J. Phys. Chem. B* **2010**, *114*, 1652-1660.

- (51) Gautieri, A.; Pate, M. I.; Vesentini, S.; Redaelli, A.; Buehler, M. J. Hydration and distance dependence of intermolecular shearing between collagen molecules in a model microfibril. *J. Biomech.* **2012**, *45*, 2079-2083.
- (52) Bratzel, G. H.; Cranford, S. W.; Espinosa, H.; Buehler, M. J. Bioinspired noncovalently crosslinked “fuzzy” carbon nanotube bundles with superior toughness and strength. *J. Mater. Chem.* **2010**, *20*, 10465.
- (53) Zhang, Z.; Turner, C. H. Water-Induced Interactions between Boron-Doped Carbon Nanotubes. *J. Phys. Chem. C* **2014**, *118*, 17838-17846.
- (54) Meng, J.; Tajaddod, N.; Cranford, S. W.; Minus, M. L. Polyethylene-Assisted Exfoliation of Hexagonal Boron Nitride in Composite Fibers: A Combined Experimental and Computational Study. *Macromol. Chem. Phys.* **2015**, *216*, 847-855.
- (55) Lee, O.-S.; Carignano, M. A. Exfoliation of Electrolyte-Intercalated Graphene: Molecular Dynamics Simulation Study. *J. Phys. Chem. C* **2015**, *119*, 19415-19422.
- (56) Fu, C.; Yang, X. Molecular simulation of interfacial mechanics for solvent exfoliation of graphene from graphite. *Carbon* **2013**, *55*, 350-360.
- (57) Welch, D. A.; Woehl, T. J.; Park, C.; Faller, R.; Evans, J. E.; Browning, N. D. Understanding the Role of Solvation Forces on the Preferential Attachment of Nanoparticles in Liquid. *ACS Nano* **2016**, *10*, 181-187.
- (58) Fajardo, O. Y.; Bresme, F.; Kornyshev, A. A.; Urbakh, M. Electrotunable Friction with Ionic Liquid Lubricants: How Important Is the Molecular Structure of the Ions? *J. Phys. Chem. Lett.* **2015**, *6*, 3998-4004.
- (59) Walton, E. B.; Lee, S.; Van Vliet, K. J. Extending Bell's model: how force transducer stiffness alters measured unbinding forces and kinetics of molecular complexes. *Biophys. J.* **2008**, *94*, 2621-2630.
- (60) Kumar, S.; Bouzida, D.; Swendsen, R. H.; Kollman, P. A.; Rosenberg, J. M. The Weighted Histogram Analysis Method for Free-Energy Calculations on Biomolecules .1. The Method. *J. Comput. Chem.* **1992**, *13*, 1011-1021.
- (61) Fredlake, C. P.; Crosthwaite, J. M.; Hert, D. G.; Aki, S. N. V. K.; Brennecke, J. F. Thermophysical properties of imidazolium-based ionic liquids. *J. Chem. Eng. Data* **2004**, *49*, 954-964.
- (62) Huddleston, J. G.; Visser, A. E.; Reichert, W. M.; Willauer, H. D.; Broker, G. A.; Rogers, R. D. Characterization and comparison of hydrophilic and hydrophobic room temperature ionic liquids incorporating the imidazolium cation. *Green Chem.* **2001**, *3*, 156-164.
- (63) Kim, K. S.; Shin, B. K.; Lee, H. Physical and electrochemical properties of 1-butyl-3-methylimidazolium bromide, 1-butyl-3-methylimidazolium iodide, and 1-butyl-3-methylimidazolium tetrafluoroborate. *Korean J. Chem. Eng.* **2004**, *21*, 1010-1014.
- (64) Bmim Br. <http://www.chemspider.com/Chemical-Structure.2015992.html>.
- (65) Wandschneider, A.; Lehmann, J. K.; Heintz, A. Surface tension and density of pure ionic liquids and some binary mixtures with 1-propanol and 1-butanol. *J. Chem. Eng. Data* **2008**, *53*, 596-599.
- (66) Taguchi, R.; Machida, H.; Sato, Y.; Smith, R. L. High-Pressure Densities of 1-Alkyl-3-methylimidazolium Hexafluorophosphates and 1-Alkyl-3-methylimidazolium Tetrafluoroborates at Temperatures from (313 to 473) K and at Pressures up to 200 MPa. *J. Chem. Eng. Data* **2009**, *54*, 22-27.
- (67) Chambreau, S. D.; Boatz, J. A.; Vaghjiani, G. L.; Koh, C.; Kostko, O.; Golan, A.; Leone, S. R. Thermal decomposition mechanism of 1-ethyl-3-methylimidazolium bromide ionic liquid. *J. Phys. Chem. A* **2012**, *116*, 5867-5876.

- (68) Fannin, A. A.; Floreani, D. A.; King, L. A.; Landers, J. S.; Piersma, B. J.; Stech, D. J.; Vaughn, R. L.; Wilkes, J. S.; Williams, J. L. Properties of 1,3-Dialkylimidazolium Chloride Aluminum-Chloride Ionic Liquids .2. Phase-Transitions, Densities, Electrical Conductivities, and Viscosities. *J. Phys. Chem-Us* **1984**, *88*, 2614-2621.
- (69) Klinov, A. V.; Fedorov, M. V.; Malygin, A. V.; Minibaeva, L. R. Properties of an aqueous solution of ionic liquid [Emim][Cl] at standard atmospheric pressure. *Russian J. Phys. Chem. A* **2014**, *88*, 1682-1688.

3. MOLECULAR SIMULATION OF GAS SOLUBILITY CAPACITY IN IONIC POLYIMIDES AND COMPOSITES WITH IONIC LIQUIDS²

3.1 Introduction

Industrial gas separation and storage processes present many technical and economic challenges to the natural gas industry and to power plants. For instance, the existence of acid gases such as H₂S and CO₂ in natural gas increases equipment maintenance and separation cost for the energy industry.¹ To make energy supply lines more economically feasible and minimize corrosion, these impurities must be removed through natural gas sweetening with removal of CO₂ prior to routing natural gas to the supply line.² Furthermore, CO₂ is the primary waste component of power plant exhaust gas and is a side product of many processes of the petrochemical industry, such as ammonia production. Palliating CO₂ from emission sources is a critical need in industry, and it is necessary in order to meet current and future environmental regulations. Aqueous alkanolamine (e.g., monoethanolamine (MEA)) solvents are the most common process liquids for CO₂ absorption units.³ However, these current separation processes are challenged by high energy demands for recovery,⁴ volatility, corrosivity, and degradation to toxic products.⁵

Adsorption in porous materials is an alternative, energy-efficient method for removing CO₂ from natural gas streams, and the development of materials possessing both high CO₂

² Reprinted with permission from LANGMUIR, doi: 10.1021/acs.langmuir.7b01977. Copyright © 2017 American Chemical Society.

selectivity and adsorption capacity are key factors. While CO₂ removal with MEA involves chemisorption (requiring significant regeneration energy), physisorption in porous materials minimizes the regeneration costs. There are some traditional adsorbents that have been widely studied such as activated carbon,^{6,7} zeolites,⁸ metal organic frameworks (MOFs),^{9,10} and silica gel.¹¹ While these materials provide high surface areas and adsorption capacity, in practical gas separation applications, there can be limits in terms of either their stability, selectivity, or cost.

Polymer materials such polyimides and polymers of intrinsic microporosity (PIMs) are emerging materials that can be used as gas separation membranes which exhibit both high CO₂ permeability (i.e., flux) and selectivity.¹² As opposed to bulk adsorbents, membranes are more amenable to continuous processing, as they achieve separation of CO₂ through the solution-diffusion mechanism. The fractional free volume (FFV) of advanced polyimides and PIMs comes from their rigid, yet contorted molecular structures,^{13,14} which creates voids and microstructure due to poor packing between polymer chains.¹⁵⁻¹⁹ Unlike MOFs, which are generally crystalline, polyimides and PIMs are glassy amorphous solids and they tend to have much higher stability in aqueous environments. A major advantage of polyimides and PIMs is the ability select/synthesize requisite monomers as a means of tailoring the polymer repeat unit to maximize specific adsorbent/adsorbate interactions.^{20,21} In order to tailor the selectivity of these materials, we are exploring the behavior of composite structures composed of an i-IP matrix to which additional IL has been added. The intent is to leverage the microporous structure of the i-IP with the tunability of the IL selectivity. Otherwise, a pure IL solvent typically suffers from high transport resistance and low free volume.²²

Ionic liquids, generally defined as organic salts with melting point temperatures < 100 °C, are potential solvents for gas separation processes.²³⁻²⁵ They have demonstrated high

selectivity for CO₂²⁶⁻²⁸ versus CH₄,^{25,29} and this makes ILs promising for applications in natural gas sweetening and pre-combustion CO₂ capture. In addition, the energy required for solvent recovery in ILs can be reduced due to the physical absorption mechanism. Nevertheless, using ILs for gas separation processes has several drawbacks. For instance, the current industrial solvent for CO₂ adsorption, MEA, is at least twenty times less expensive on a per volume basis than even the lowest cost ILs. The second, and possibly the most important drawback for ILs is their high viscosity relative to organic solvents. However, using ILs in membrane systems has significant advantages relative to their use as bulk absorbents.³⁰ The high viscosity of ILs can be mitigated in membrane units, due to the short diffusion paths.³⁰ In addition, the physical stability and processability of i-IPs make these materials an excellent matrix in which to immobilize ILs.³¹ In a recent publication,³² these hybrid materials have demonstrated excellent CO₂/CH₄ separation performance ($S_{\text{CO}_2/\text{CH}_4} = 13.1$) with enhanced permeability (up to 2242% for CO₂ and 2732% for CH₄) when the IL was present within the ionic polyimide.

Several others have recently examined the properties of PIMs and similar materials for gas separations.³³⁻³⁵ Hart, et al. used molecular simulations to model the CO₂/CH₄ separation performance of nitrogen-containing PIMs (tetrafluoroterephthalonitrile) and sulfonyl-based PIMs.²⁰ They also evaluated the permselectivity of these membranes for CO₂/CH₄ and CO₂/N₂ separation processes,¹⁵ concluding that the polar sulfonyl functionality increases the gas solubility and permselectivity. With regards to CO₂/CH₄ gas separation, the solubility and permeability of CO₂ increases by adding dipolar functionalities and bulky spirocenter groups on the PIM, since these groups increase both the enthalpy of CO₂ adsorption and FFV. In related work, Calero et al.³⁶ investigated the CO₂ adsorption isotherm and selectivity of CO₂/CH₄ in both a hydrated structure of a covalent organic framework (COF) and in a COF structure with a small

amount of IL. Adding the IL in the COF structure increased the selectivity of the CO₂ without a drastic reduction in the adsorption capacity. In the hydrated COF structure, the adsorption capacity tends to decrease while the selectivity increases in favor of the CO₂. In comparison, PIMs possess an amorphous structure, while the COFs have crystalline structures (more similar to MOFs), but with covalently bonded structures of light elements (C, H, N, O, B, etc.) instead of coordinated metallic ions during the reaction. Covalent bonds of light elements (H, B, C, N, and O) compose the crystal structure in COFs while crystal structures of MOFs are coordinated by metal ions.

While the experimental realization of the first generation of i-IP + IL composite materials have already been reported,³² molecular simulations can provide detailed insight into the molecular-level structures and interactions in these systems responsible for the experimentally observed behavior. In our study, the 1-butyl-3-methylimidazolium bis(trifluoromethylsulfonyl)imide ([C₄mim][Tf₂N]) IL has been chosen to reside within the ionic polyimide matrix because of the structural consistency between the i-IP and [C₄mim⁺][Tf₂N⁻] and because this particular IL has been thoroughly studied and its absorption properties toward CO₂ are well-known (**Figure B3.11**).^{1,37-41} We thoroughly characterize the neat i-IP relative to the i-IP + IL composite materials by analyzing their average pore size distributions, surface areas, FFV, as well as their adsorption of CO₂ and CH₄. The adsorption data is benchmarked against recent experimental results, and we are able to achieve good agreement with the experimental data,³² but this is only obtained after a moderate densification of the simulation cell. Overall, our study highlights the nuances of structural relaxation and its importance on the emergent adsorption behavior in i-IP-based materials, as well as the changes in the molecular-level adsorption behavior induced by the presence of the IL within the i-IP matrix.

3.2 Simulation Details

Our simulation procedure is comprised of several different steps. First, electronic structure calculations are used to assign partial charges on the atom sites of the i-IP monomer units. Then, molecular dynamics simulations (MD) are used to prepare the relaxed initial structure of the neat i-IP and i-IP + IL composite, and this involves a polymerization scheme, followed by several stages of structural relaxation. The initial system also contains an N-methyl-2-pyrrolidone (NMP) solvent, which is eventually removed and replaced with the IL species following polymerization, and this is intended to mimic the experimental synthesis procedure.³² Finally, using an iterative combination of molecular dynamics and grand canonical Monte Carlo (GCMC) simulations, the solubility of CO₂ and CH₄ is modeled over a wide range of different pressures within the neat i-IP and i-IP + IL composite materials. The details of each stage are described below, and a schematic overview of our simulation models is illustrated in **Figure 3.1**.

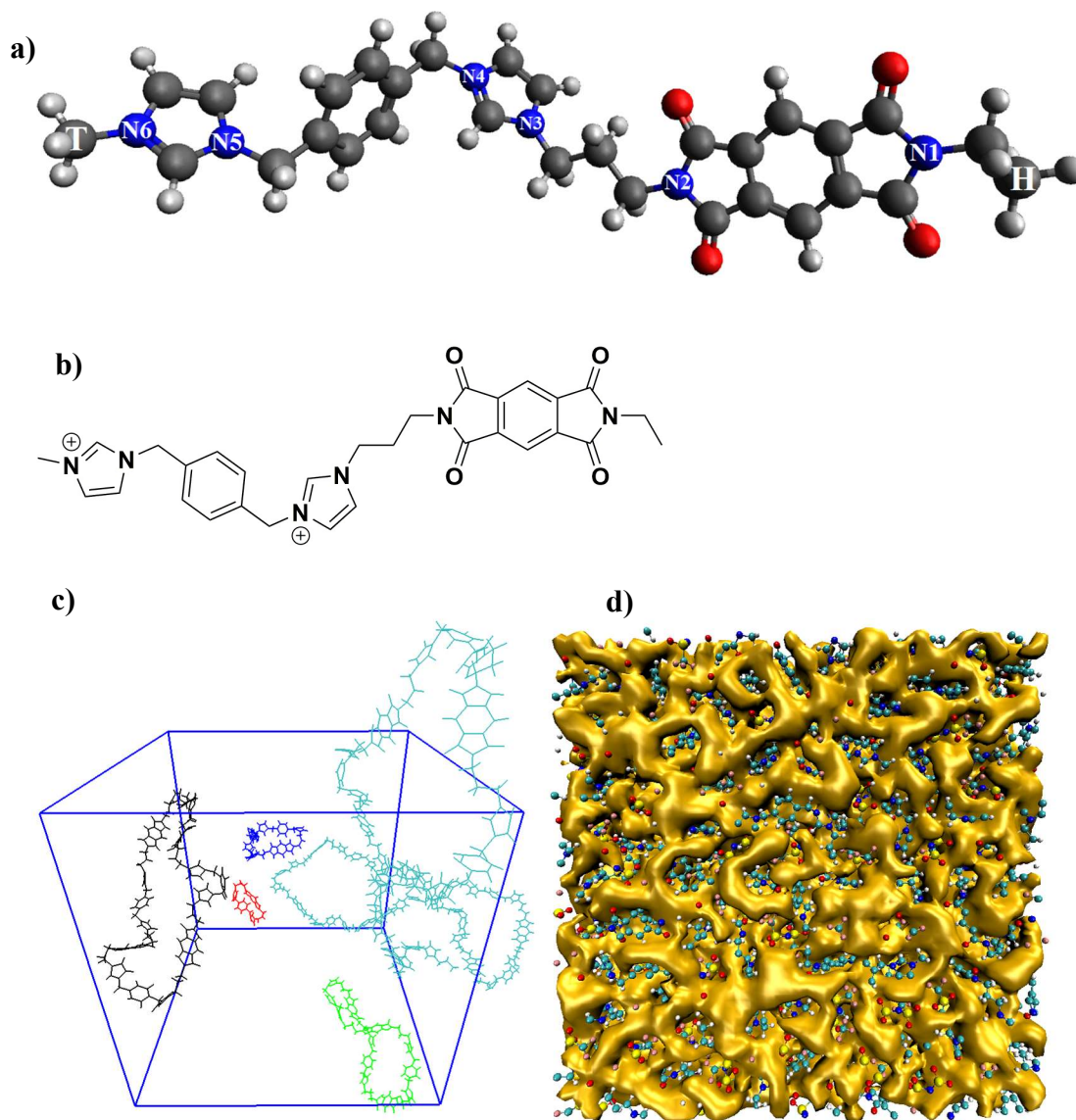


Figure 3.1. Representative overview of the simulation models: a) i-IP monomer, atoms are colored according to their type (N = navy, O = red, C = grey, and H = white). Specific nitrogen sites of the i-IP are labeled for reference, as well as the head (H) and tail (T) designation; b) 2-dimensional monomer representation; c) post-polymerization with different chain lengths (red: 1, blue: 2, green: 3, black: 4, and cyan: 12 monomers). $[\text{Tf}_2\text{N}^-]$ and NMP are deleted for clarity; and d) visualization of the FFV (gold region) within the final polymer system.

In the electronic structure calculations, the geometric optimization of the isolated monomer structure was conducted using the B3LYP functional⁴² with the 6-31G(d) basis set

using Gaussian09.⁴³ Using the relaxed structure, the partial charges on each atom were approximated using the ChelpG method.⁴³ Other charge assignment schemes (Hirschfeld, NBO, Merz-Kollman) were also evaluated, and consistent results were found. Ultimately, the partial charge results from the ChelpG method were used to modify the monomer topology file in combination with OPLS-AA force field parameters for monomer interactions. Force field parameters for [C₄mim][Tf₂N] ILs were taken from Lopez, et al,^{44,45} while parameters for NMP molecules were extracted from Aparicio, et al.⁴⁶ The TraPPE⁴⁷ force field for CO₂, and CH₄ was used, based on the previous experience of others modeling gas adsorption in ILs.^{1,27,48} The Lorentz-Berthelot mixing rules were used for cross-term interactions.

Following the assignment of the force fields, the i-IP and i-IP + IL systems were constructed and conditioned according to the following default procedure (with specific variations noted later in the text):

- a) Ionic polyimide monomers were inserted into the simulation box using PACKMOL,⁴⁹ followed by energy minimization using the steepest descent algorithm. In order to test for finite-size effects, systems with 55, 110, and 200 monomer units were tested (along with the balance of [Tf₂N⁻] molecules to maintain charge neutrality). In addition, each of these systems was run at least twice, in order to evaluate the reproducibility of the results.
- b) In addition to the monomers, NMP molecules were also inserted at three different ratios: 1:4, 1:6, and 1:8 (monomer:NMP). The experiments used a ratio of approximately 1:60 during polymerization.³²
- c) The monomer + NMP molecules were relaxed with MD simulations using a cycle of canonical (NVT) to increase the temperature following with isothermal-isobaric (NPT)

ensemble simulations at high temperature and pressure, followed by a slow quench to room temperature.

- d) The monomer units were polymerized, using a nearest-neighbor algorithm (described below), followed by additional relaxation with MD.
- e) The NMP was then removed from the system, and the i-IP + IL samples were generated by inserting the IL molecules in the cavities left by the NMP molecules, again using PACKMOL.
- f) Both neat i-IP and i-IP + IL systems were further equilibrated and relaxed via NVT and NPT cycles, until a final temperature of 294 K and a pressure of 1 bar was reached.

All of the MD simulations were performed with the GROMACS 5.0 simulation package.⁵⁰ The Lennard-Jones potential and electrostatic interactions were calculated with a cut off distance of 1.4 nm, and the smooth particle mesh Ewald sum (SPME)⁵¹ method was implemented for long-range electrostatic interaction with 0.16 nm of Fourier-spacing. The Nose-Hoover thermostat⁵² was used to maintain the temperature and the Parrinello-Rahman⁵³ barostat was used to maintain the pressure, and the time step was 1 fs. In the MD simulations, periodic boundary conditions were implemented in all three dimensions.

In order to test for finite-size effects and to evaluate system equilibration, the configurations of the initial monomer systems were compared with respect to different system sizes (55, 110, and 200 monomers, which correspond to box lengths of approximately 4, 5, and 6 nm, respectively) and different simulation durations. In order to help analyze the initial structural relaxation of the monomers, radial distribution functions (RDFs) were calculated for the tail (T) and head (H) carbons of the monomers, as labeled in **Figure 3.1**. The RDF results are shown in **Figure B3.10**, indicating that at short times (~10 ns) there are some slight

inconsistencies in the system configurations between different independent runs with varying box sizes, but at longer time (~50 ns), there is excellent agreement among the 3 different system sizes. Also, after this relaxation and decreasing the temperature to 294 K, the density is very consistent for all boxes (1.614 g/cm³) at the final pressure of 1 bar.

After the monomer relaxation, polymerization was then performed by connecting the head and tail groups, according to a nearest-neighbor algorithm. More sophisticated approaches have also been used to emulate the polymerization process, such as the *Polymatic* algorithm,⁵⁴ which temporarily assigns charges to the head and tail groups of the monomers (accelerating the pairing process). Karayiannis, et al.⁵⁵ suggested that low-density polymerization helps to provide free volume for sufficient mobility and flexibility of the chain. Thus, our polymerization step was conducted at an elevated temperature of 550 K and a pressure of 1 bar, in order to provide for effective conformational flexibility. The monomers were attached using an in-house code that analyzed the H-to-T separation distance, and if within a cutoff (1.27 nm on average), then a hydrogen atom from each head and tail is removed, followed by the formation of a covalent bond.

The prepared i-IP structures then followed a steepest-descent energy minimization step for all bonded and non-bonded interactions.⁵⁶ In past work, it has been noted⁵⁵ that temperatures as high as 2000 K were needed to achieve adequate fluctuation and relaxation of glassy polymers. Thus, after polymerization, we continued the equilibration process at a temperature of 2000 K in both the NVT and NPT ensembles prior to cooling to the desired temperature of 294 K. With different initial box sizes (4, 5, and 6 nm) and different initial monomer configurations, the final polymer length distributions varied somewhat. In order to estimate the reproducibility

of our results, these different replicas were all evaluated in our physical and adsorption property analysis. A summary of the different i-IP systems is described in **Table 3.1**.

Table 3.1. Summary of different i-IP systems simulated, with densities corresponding to conditions of 1 bar and 294 K.

description (including approximate box length)	# monomers	# NMP	density (g/cm ³)	polymer chain lengths*
neat, 4 nm (sample 1)	55	0	1.602	29, 10, 7, 7, 2
neat, 4 nm (sample 2)	55	0	1.602	42, 9, 2, 2
neat, 5 nm (sample 1)	110	0	1.625	78, 10, 17, 5
neat, 5 nm (sample 2)	110	0	1.604	33, 46, 2, 14, 15
neat, 6 nm (sample 1)	200	0	1.601	15, 20, 76, 56, 29, 2, 2
neat, 6 nm (sample 2)	200	0	1.641	17, 8, 8, 5, 5, 4(6), 3(11), 2(18), 1(64)
neat, 6 nm (sample 3)	200	800	1.600	80, 13, 41, 40, 20, 6
composite, 6.8 nm (sample 1)	200 (+ 200 IL)	800	1.580	80, 13, 41, 40, 20, 6
composite, 6.8 nm (sample 2)	200 (+ 200 IL)	1200	1.584	178, 14, 8

**Numbers inside the parentheses represent the replication of that polymer chain length.*

As mentioned previously, the experimental production of the i-IP samples involved the addition of NMP (5 mL per gram of monomer, which is a monomer:NMP molar ratio of 1:60).³² After the experimental polymerization reaction is complete, the side products and solvents are removed from the polymer. In order to mimic this process and to create the temporary voids for the IL insertions, the NMP molecules were present throughout the monomer equilibration and polymerization steps. After system equilibration and polymerization, the NMP molecules were

then deleted from the box and the void spaces filled with [C₄mim][Tf₂N] molecules using PACKMOL software. To make sure that we made enough space for [C₄mim][Tf₂N] and were able to generate a well-mixed system, we started with three different ratios of monomer:NMP molecules of 1:4, 1:6, and 1:8. For consistency with the experiments, the IL was added to the i-IP at the same concentrations of 50:50.

Once the neat i-IP ionic polyimide and i-IP + IL samples were prepared, we used the Cassandra package to run grand canonical Monte Carlo (GCMC) simulations of CO₂ and CH₄ adsorption.⁵⁷ During GCMC simulations, the polymer and IL molecules are held rigid, while the GCMC steps involving the gas adsorbates were run for at least 3×10^6 steps (with 33% insertion, 33% deletion, 17% translation, and 17% rotation). In order to improve sampling, these GCMC simulations were iteratively combined with MD simulations to further relax the system configuration. For instance, after finishing one stage of GCMC simulations, the resulting structure (including the gas molecules) was subjected to a short NVT MD relaxation process of 1 ns at the same temperature (294 K). After the MD stage, the resulting structure was then transferred back to the GCMC stage for continued insertion and deletion of gas molecules. This process continued for at least three cycles for each point along the adsorption isotherm, and the average value of the final GCMC cycles is reported in the isotherm graphs and also used to calculate Henry's constants. Henry's constant was extracted from the slope of the fitted line to the solubility graph, which was then converted from units of g/(L·bar) to mol/(L·atm).

In order to connect the i-IP and i-IP + IL composite adsorption properties to the underlying molecular configurations, several different structural analyses were performed, which were originally applied to characterize solid adsorbents. Using the approaches of Gelb and Gubbins,⁵⁸ we calculate the fractional free volume (FFV), pore size distribution (PSD), and

exposed surface area of our i-IP and i-IP + IL composite models (which include all atomic sites during the analysis, with the Lennard-Jones diameters used to define the molecular surfaces), as well as the radial distribution function of key interaction sites in the system.

3.3 Results and Discussion

3.3.1.1 Structural Optimization

The densities of the neat i-IP and i-IP + IL composite systems were optimized, in order to reproduce the experimental CO₂ adsorption data. Thus, the initial system densities ($\sim 1.6 \text{ g/cm}^3$) were slightly decreased to $1.565 \sim 1.589 \text{ g/cm}^3$, while the adsorption behavior was predicted by the GCMC simulations (with the i-IP and i-IP + IL composite considered rigid). These simulation results are indicated by the large red circles in **Figure 3.2**, and they compare well with the experimental data. From these initial simulations, the i-IP and i-IP + IL composite structures were further subjected to stages of MD relaxation. Even though the systems were thoroughly relaxed prior to the initial GCMC simulations, the presence of the adsorbate molecules tends to help condition the adsorbent to increase its capacity. Each MD stage tends to further relax the system, providing additional adsorption capacity during the subsequent GCMC stage. Thus, at a fixed system density, the adsorption still continues to increase by a factor of 2-3 by subjecting the system to additional MD/GCMC stages. Thus, in order to capture the experimental behavior, the system was then gradually compressed until the adsorption approached the experimental values. The optimized i-IP structures had densities approximately 10% higher ($1.72 \pm 0.03 \text{ g/cm}^3$) after the compression steps, with the final values indicated by the green circles in **Figure 3.2**. Each system optimization was repeated three times from the initial structure to the optimized one to evaluate the reproducibility of the results. All GCMC simulations were performed at 294 K and 1 bar for $3\sim 5 \times 10^6$ MC steps while MD calculations

were implemented in the NVT ensemble for 1 ns at 294 K. These final structures were used to calculate the gas adsorption isotherms, as well as for the structural analyses. We followed the same procedure to optimize the i-IP + IL composite, leading to a final density of 1.62 ± 0.02 g/cm³.

In the experiments, an NMP solvent was used during the initial polymerization,³² and then washed away prior to adsorption. To consider the effect of NMP on the simulated structure and gas solubility results, we compared two samples: one includes NMP during polymerization and one is conducted without NMP molecules during polymerization (**Figure B3.12**). After polymerization, the NMP molecules were deleted from the system, followed by relaxation of both systems. As **Figure B3.12** shows, the presence of the NMP solvent during the polymerization simulations does not appreciably affect the final gas solubility. The sample without NMP is referred to as “neat, 6 nm (sample 1)” and the sample with NMP is referred to as “neat, 6 nm (sample 3)”. Although they show a noticeable difference in the first GCMC simulations, their gas adsorption properties converge very closely after 4 cycles of MD/GCMC. Thus, the temporary presence of the NMP molecules was useful for preparing the i-IP+ IL composites, but the NMP does not seem to be responsible for any other residual effects on the gas adsorption performance.

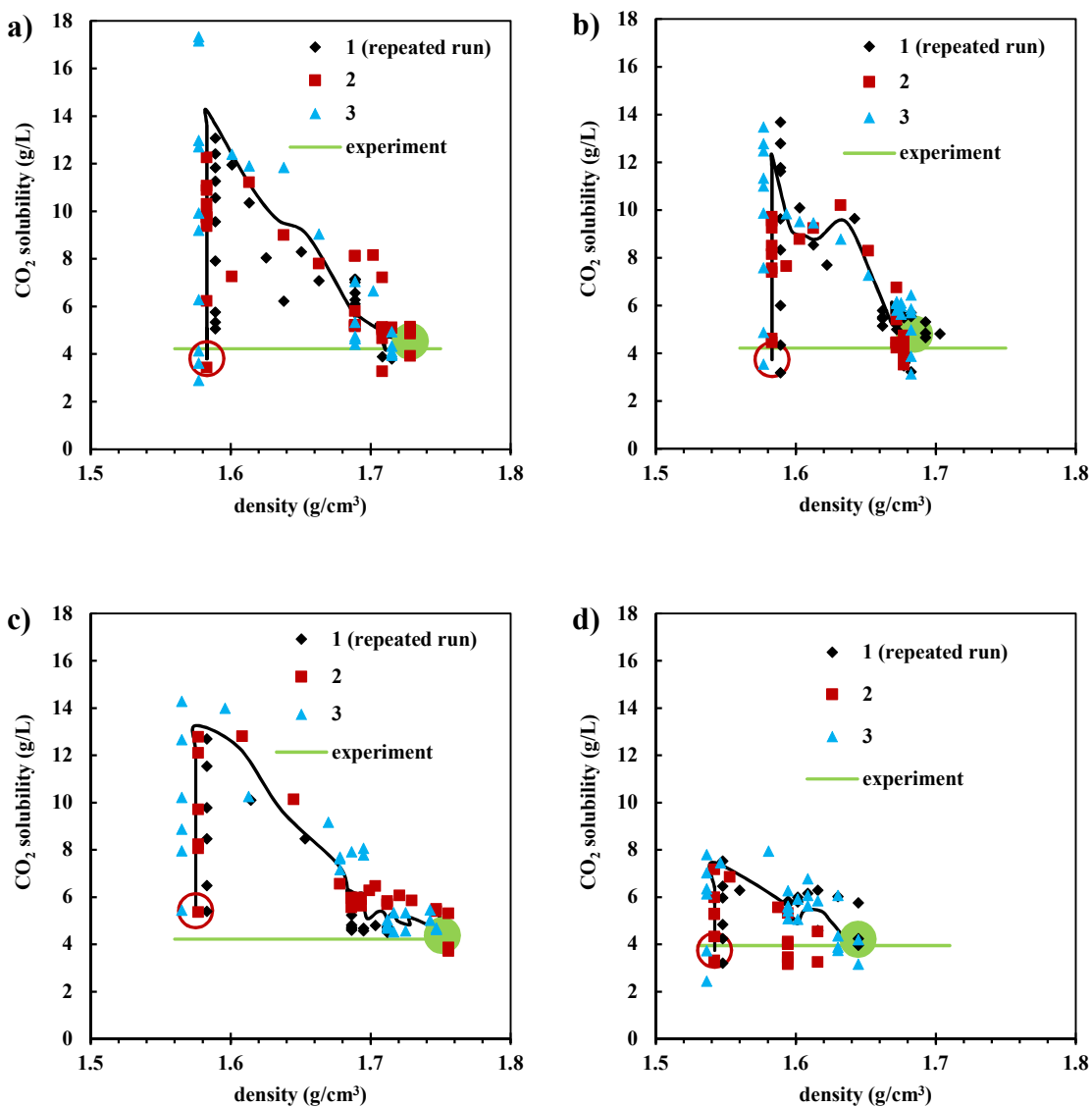


Figure 3.2. CO₂ solubility during densification and relaxation for: a) 55 monomers; b) 110 monomers; c) 200 monomers; and d) 200 monomers in 200 [C₄mim][Tf₂N]. These results are extracted from incremental cycles of MD and GCMC simulations, with each point corresponding to one MD/GCMC cycle. The hollow red circle is the starting point, the green circle is the final optimized structure, and the solid black line is a guide to the eye corresponding to successive cycles. The green line represent the experimental data,³² with a standard deviation of < 5%.

3.4 Structural Analysis

As illustrated in the previous section, the polymer adsorbent shows different solubility values at constant density. While switching back and forth between MD and GCMC calculations, the polymer structure was increasingly relaxed to accept more CO₂ molecules. In order to make the connection between the adsorption data and the different simulation structures, the surface area and FFV were calculated at different points along the simulation trajectory. During the MD simulations, the polymer molecules were free to modify their positions, and during GCMC calculation this modification helped the structure accept more gas molecules until the structure was saturated at the desired temperature and pressure. The exposed surface area (calculated as an average over multiple independent configurations at each stage) can help characterize the structural modification from the initial point to the maximum point of the solid line. At constant density, from the red hollow circle to the maximum point of the solid line, the surface area in the polymer structure increased (**Figure 3.3**), while the FFV is constant (**Figure 3.4**). As **Figures 3.3 and 3.4** show, the predicted solubility tends to be much more sensitive to the exposed surface area versus the FFV, which is typically used as a surrogate to predict gas solubility.

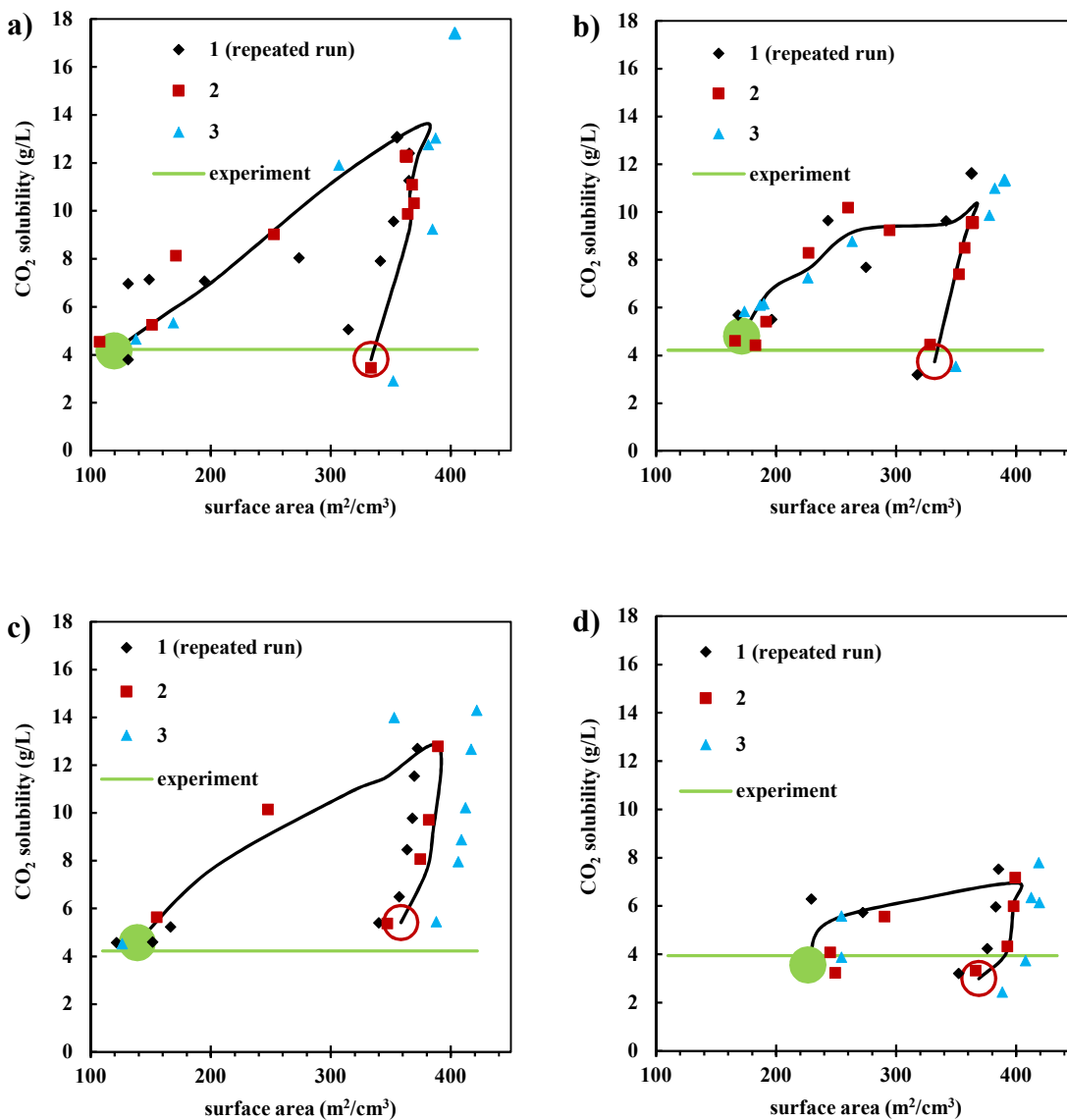


Figure 3.3. CO₂ solubility versus surface area for: a) 55 monomers; b) 110 monomers; c) 200 monomers; and d) 200 monomers in 200 [C₄mim⁺][Tf₂N⁻]. The results are extracted from successive cycles of MD/GCMC simulations. The hollow red circle is the starting point, the green circle is the optimized structure, and the black solid line is a guide to the eye.

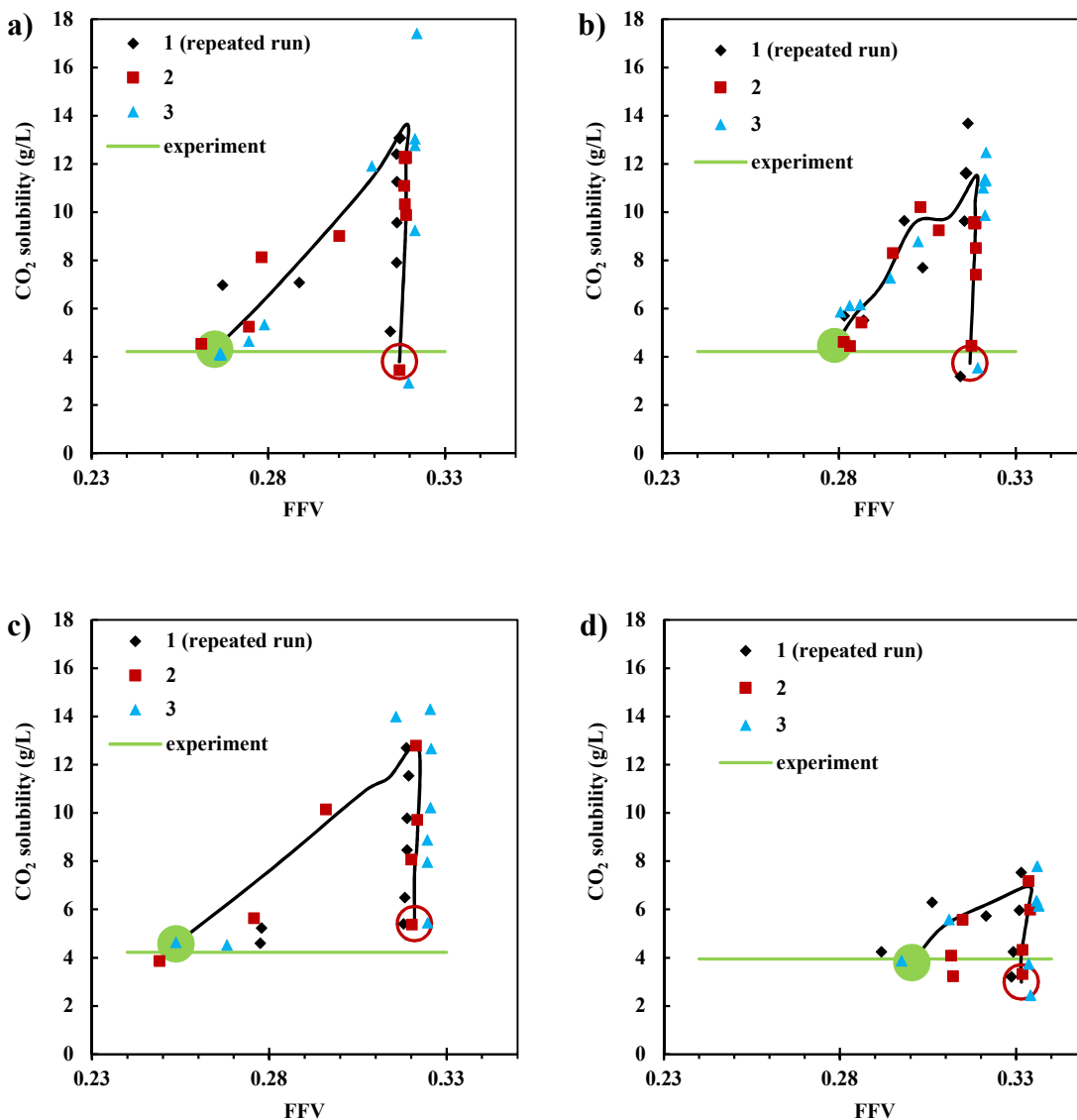


Figure 3.4. CO₂ solubility versus FFV for: a) 55 monomers; b) 110 monomers; c) 200 monomers; and d) 200 monomers in 200 [C₄mim][Tf₂N]. The results are extracted from successive cycles of MD/ GCMC simulations. The hollow red circle is the starting point, the green circle is the optimized structure, and the black solid line is a guide to the eye.

The pore size distribution is one of the key factors for characterizing the gas separation properties of porous materials. **Figure 3.5** shows the pore size distribution of our i-IP systems at

294 K (corresponding to both initial and final structures). The solid lines represent the initial structures (densities of 1.565 ~ 1.589 g/cm³), while the dashed lines represent the final optimized structures. As the density increases, the PSD shifts towards smaller pore sizes, and the FFV decreases, as well. The smaller pore sizes reduce the adsorption capacity of the polymer for both CO₂ and CH₄. **Figure 3.5** shows that similar densities tend to possess similar FFVs and similar pore size distributions. However, as noted previously, the calculated surface area can provide additional distinction between these systems, and the surface area calculation can be performed very efficiently (significantly faster than calculating the PSD).

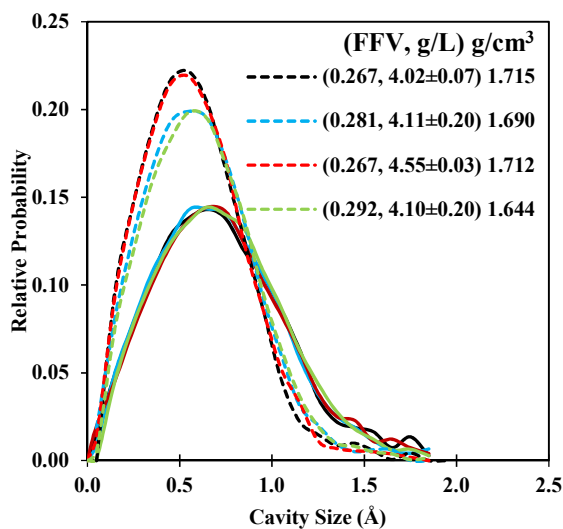


Figure 3.5. Pore size distribution of initial structures (solid lines) and optimized, compressed structure (dashed lines) at 294 K. Colors represent different polymer systems: 55 monomers (black), 110 monomers (blue), 200 monomers (red), and 200 monomers + IL (green). Fractional free volume, CO₂ solubility, and the density are reported for the optimized structures.

3.5 Gas Solubility

The partial pressures of CO₂ in exhaust gases of power plants and flare chambers are around atmospheric pressure. Therefore, we have calculated the isotherm of the desired gases (CO₂ and CH₄) over the range of pressures from 1 × 10⁻³ bar up to atmospheric conditions. The

experimental CO₂ and CH₄ solubility³² at atmospheric pressure and 294 K have been used to benchmark our results (**Figure 3.6**). Adding ILs to the pure polymer did not significantly change the solubility of the gas in the i-IP. However, upon further analysis, we are able to identify very different molecular interactions between the gas molecules and the i-IP and i-IP + IL systems.

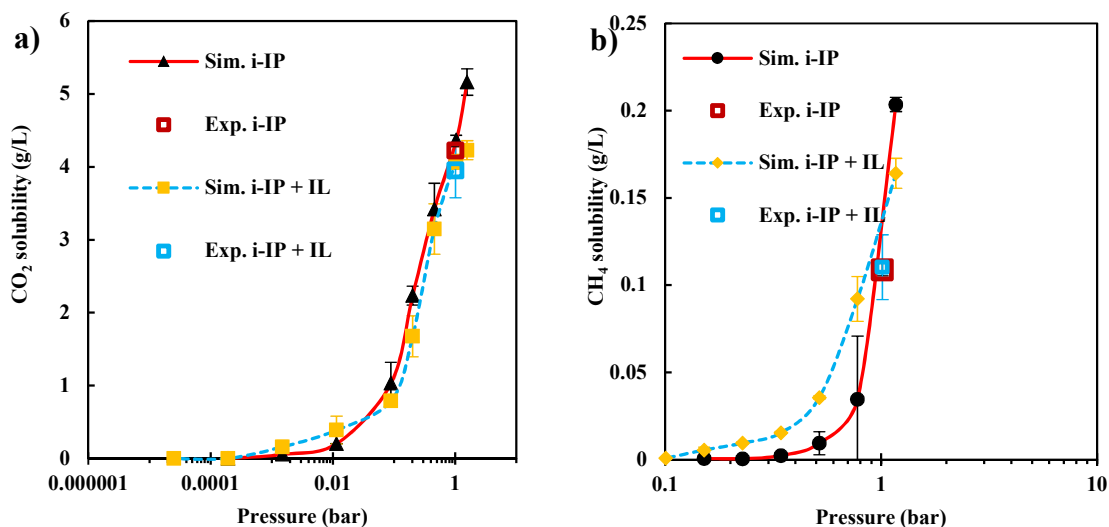


Figure 3.6. Adsorption isotherms at 294 K of: a) CO₂, b) CH₄ (gas solubility values are provided in Table B3.3).

The Henry's constant was also calculated for CO₂ and CH₄ in the i-IP. Adding the IL to the i-IP did not significantly affect CH₄ solubility (0.012 for i-IP and 0.009 mol/(L·atm) for i-IP+IL). Surprisingly, adding the IL to the i-IP slightly reduced the solubility of the CO₂ (0.075 for i-IP and 0.066 mol/(L·atm) for i-IP + IL composite). The Henry's law constant in this report was calculated at 294 K over a pressure range of 0 to 1 bar. In comparison, the reported experimental Henry's law constant for CO₂ and CH₄ in [C₄mim][Tf₂N] is 0.066 and 0.010 mol/(L·atm), respectively. The experimental Henry's law constant was reported at 333 K over a pressure range of 0 to 5 bar for CO₂ and 0 to 20 bar for CH₄.^{1,25,59} Additional data for carbon

dioxide and methane solubility in 1-ethyl-2-methylimidazole and 1-pentyl-2-methylimidazole is included in **Table B3.2**.⁶⁰ According to the simulation and experimental results, adding the IL to the polymer (at a ratio of 50:50) did not significantly change the adsorption of the polymer in favor of CO₂. However, the i-IP and i-IP + IL composite still strongly adsorb CO₂ versus CH₄, and the experiments indicate a significant increase in gas permeability, which we intend to investigate further in future work.

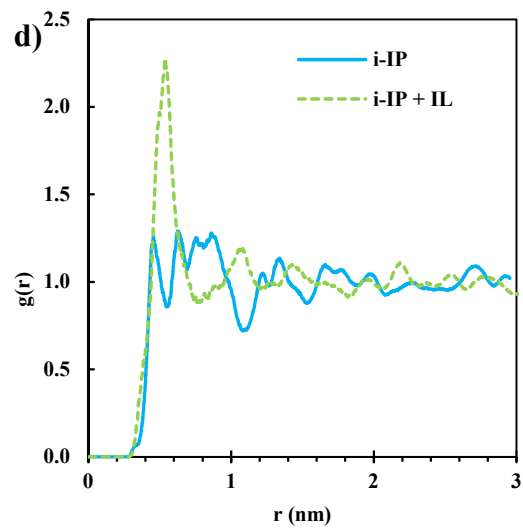
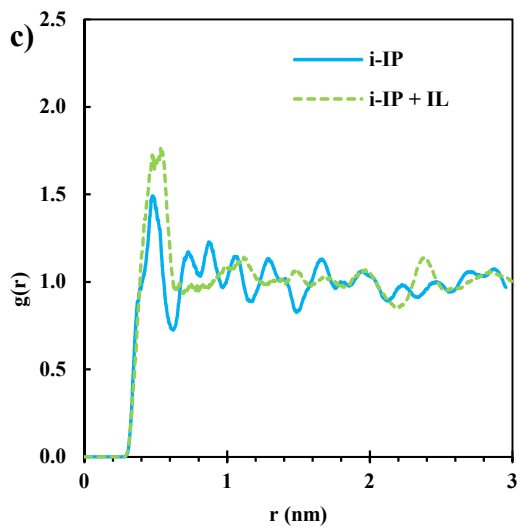
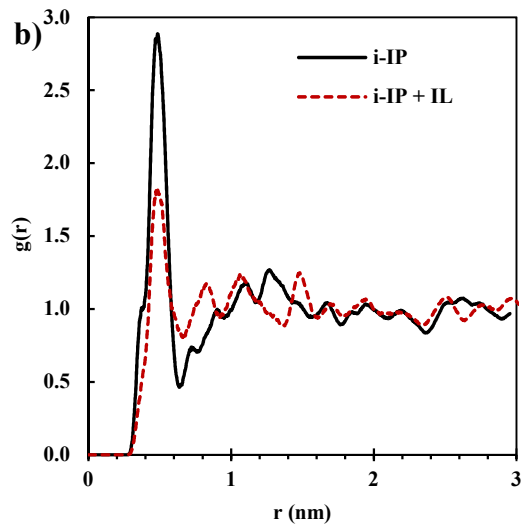
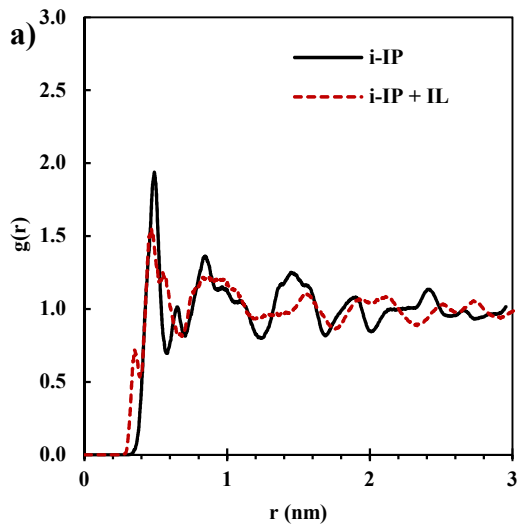
3.6 Analysis of Adsorbate Interactions

Identifying the dominant CO₂ adsorption interactions in our i-IP and i-IP + IL composite models can reveal useful information for understanding the current gas adsorption behavior and also help guide the design for future i-IP-based materials. In particular, it is important to characterize the adsorption site preferences for CO₂ versus CH₄, since it is difficult to anticipate the balance of adsorption enthalpy and site accessibility in our amorphous structures. To help identify the site selectivity for CO₂ and CH₄, we analyzed the RDFs of the gases with specific sites of the i-IP. In order to calculate the RDFs, we extracted 10 different configurations at each stage (each separated by 0.5×10^6 steps). Each of these extracted samples was further relaxed with MD simulations for 10 ns, and the reported RDFs are the average of these 10 samples. We have labeled six different nitrogen atoms in the monomer structure: N1 and N2 represent the ligand nitrogen atoms while N3 to N6 represent the imidazolium ring nitrogen atoms in the monomer structure (see **Figure 3.1**). As **Figure 3.7** shows, the ligand nitrogen atoms in the i-IP have strong interactions with the adsorbed CO₂ gas. After the addition of the IL, this interaction is weakened and the adsorbed CO₂ molecules are located mostly around the imidazolium ring of the polymer. Since the polymer structure is fairly symmetric, the adsorbed CO₂ may move to either the right or left side of the ligand. However, as **Figure 3.7 b** shows, CO₂ molecules are

likely attracted to the N2 atom of the ligand. Thus, it is more probable that CO₂ molecules were moved toward the first imidazolium ring containing N3 and N4. As **Figure 3.7 c,d** show, the interaction intensity of the adsorbed gas molecules with N3 and N4 is higher in the i-IP + IL composite, while the intensity of the CO₂ interactions with N5 and N6 remains unchanged (**Figure 3.7 e and f**).

Methane shows very different interactions with the adsorbent structures. As **Figure 3.8** shows, CH₄ molecules are mostly located at N5 and more specifically at N6 sites of the imidazole ring of the polymer. Adding the IL to the i-IP changes the preferred CH₄ locations. Composite structures of i-IP + IL have strong interactions between the CH₄ and the N1 atom, since it is the closest nitrogen atom to the N6 in the monomer structure (**Figure 3.8 a**). The interaction strength between the N3 site and CH₄ will increase upon the addition of the IL (**Figure 3.8 c**). Overall, CO₂ molecules are most likely located at the ligand site of the i-IP and adding IL moves them toward the imidazolium ring of the monomer. However, CH₄ molecules are mostly located near the imidazolium ring site of the monomer, and adding the IL to the i-IP moves the CH₄ molecules toward the ligand site of the monomer.

This work reports pure gas adsorption simulations. However, competition of CO₂/CH₄ to occupy the active sites of the composite structure in different concentrations of CO₂/CH₄ may reveal more information about the selectivity of this structure. This will be investigated in future work. As **Figures 3.7 and 3.8** show, the interaction of the i-IP + IL composite with CO₂ is stronger and well distributed along the nitrogen sites of the polymer than its interaction with CH₄. To support this idea, **Figure 3.9** compares the interaction of CO₂ and CH₄ with [Tf₂N⁻] in the i-IP and composite structure. While the CO₂ interaction remains constant in both structures, the CH₄ interaction with [Tf₂N⁻] decreases significantly in the composite structure.



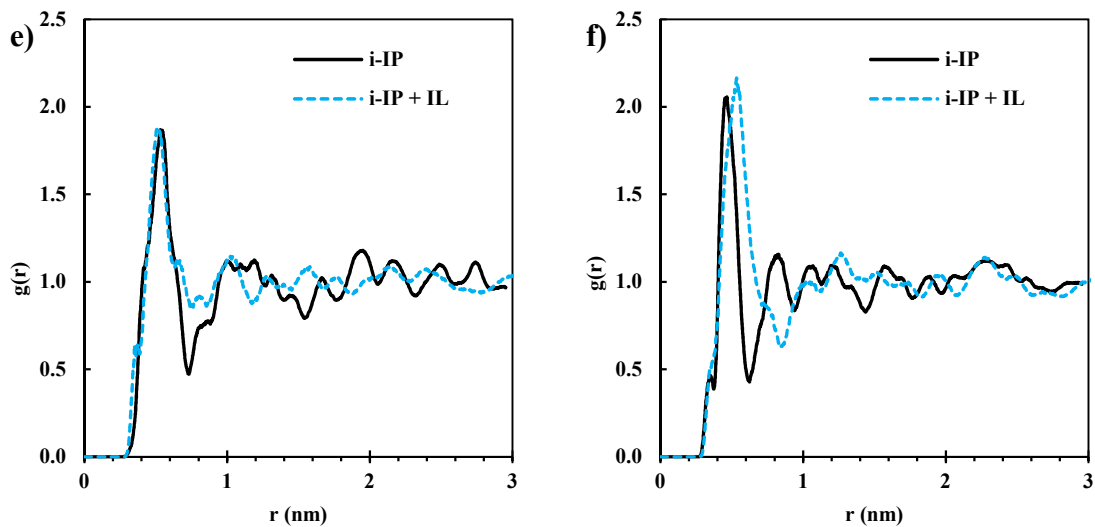
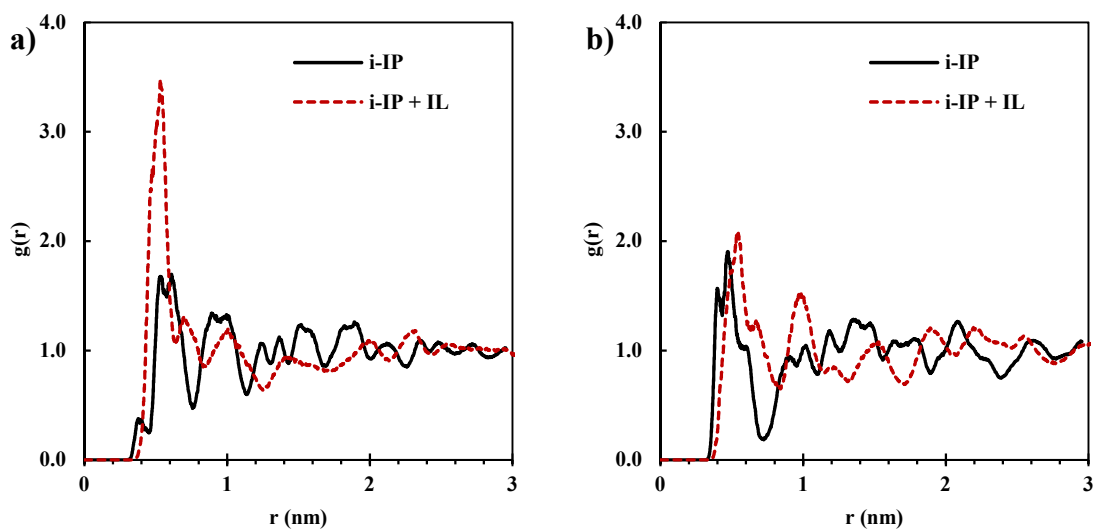


Figure 3.7. Radial distribution function between the carbon atom of CO_2 and the i-IP sites: a) N1; b) N2; c) N3; d) N4; e) N5; and f) N6 (see Figure 3.1 for site labels).



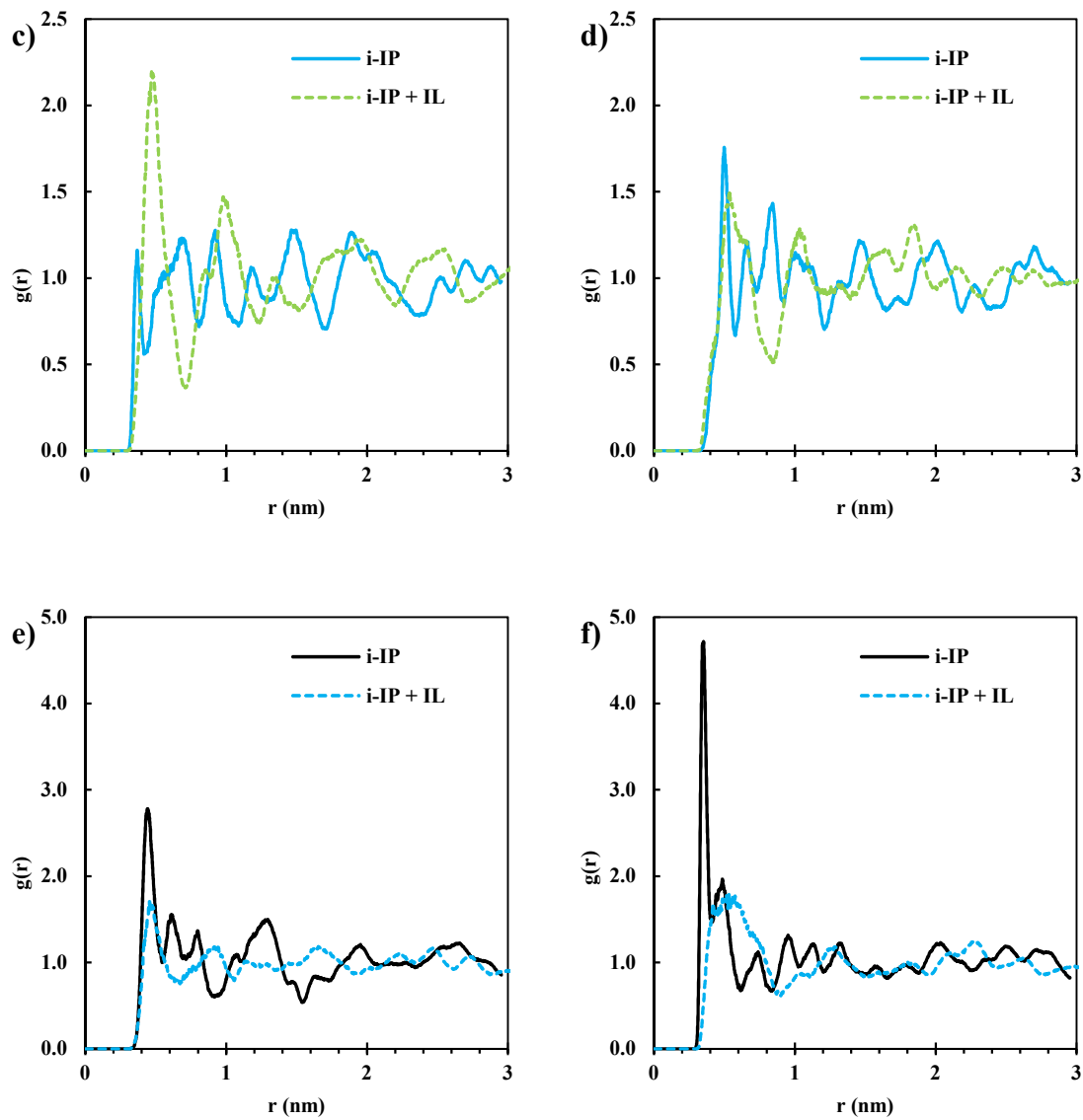


Figure 3.8. Radial distribution functions of the carbon atom of CH₄ with the i-IP sites: a) N1; b) N2; c) N3; d) N4; e) N5; and f) N6 (see Figure 3.1 for site labels).

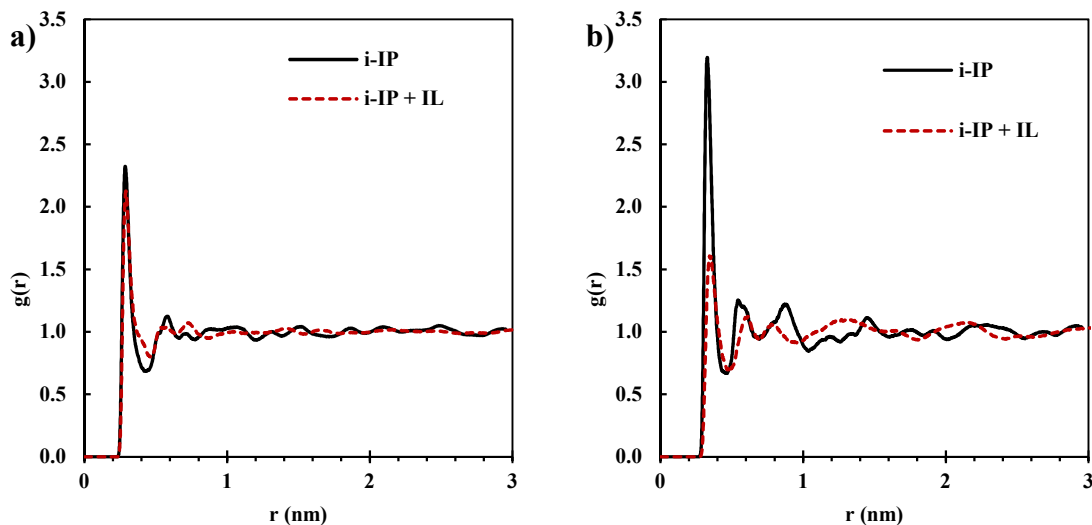


Figure 3.9. Radial distribution function of the oxygen atoms of the $[\text{Tf}_2\text{N}^-]$ anions with the carbon atoms of: a) CO_2 ; and b) CH_4 (see Figure 3.1 for site labels).

3.7 Conclusion

In this study, the solubility of CO_2 and CH_4 in an i-IP and an i-IP + $[\text{C}_4\text{mim}][\text{Tf}_2\text{N}]$ composite was predicted and benchmarked against experimental values. In addition, the structural details of the adsorbents and the molecular-level interaction with the gas molecules were identified. Several different aspects were highlighted. First, the cyclical relaxation between MD and GCMC was found to have a significant effect on the adsorption capacity. Even though the adsorbents were thoroughly relaxed prior to the initial GCMC stage, further relaxation with MD in the presence of the CO_2 was found to significantly increase the gas adsorption. Second, by tracing the structural relaxation of the system, we found that the exposed surface area of the adsorbent is a fairly sensitive measure of the adsorption performance (while the density, PSD, and FFV remain essentially constant). Finally, although the addition of the IL to the i-IP matrix has a negligible effect on the relative adsorption of CO_2 and CH_4 , it has a dramatic effect on the nature of the gas adsorption. We predict that the preferred adsorption sites

of the CO₂ and CH₄ shift among the ligand nitrogens and imidazolium nitrogens, depending upon the presence of the IL in the i-IP material. Overall, this information is expected to provide important molecular-level details for the design of future i-IP and i-IP + IL composites for optimizing the transport rates and selectivity of different adsorbates. While the permeability can be significantly enhanced in the i-IP + IL composites, specific functionalization of the i-IP or IL selection can be used to further increase the selectivity.

In regards to the simulation procedure, a moderate densification of the systems (up to 10%) was required to capture the experimental adsorption data. While this approach may not be transferrable to other systems or to other temperature and pressure conditions, future work will test the generality of such an approach for other i-IP and i-IP + IL composites. For instance, it is recognized that there are other potential sources for the initial quantitative disagreement with the experiments, such as shortcomings in the intermolecular potential (including the assignment of partial charges). Regardless, we find that a thorough analysis of the system relaxation is necessary, since subtle changes in the system can impart large changes in the predicted adsorption behavior.

Acknowledgements

Support for this work was provided by the National Science Foundation (CBET-1605411) and computer resources were provided by the Alabama Supercomputer Center.

Supporting Information

The Supporting Information is available in Appendix B. It includes i-IP monomer equilibration analysis, additional illustrations of the molecular models, tests of the influence of the NMP solvent, and Henry's constants.

Appendix B, Supporting Information for Chapter 3

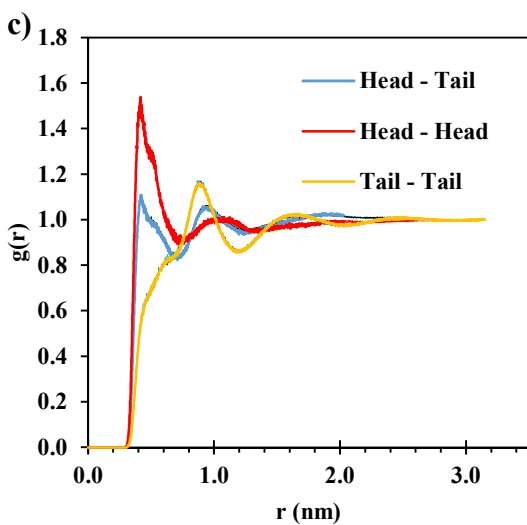
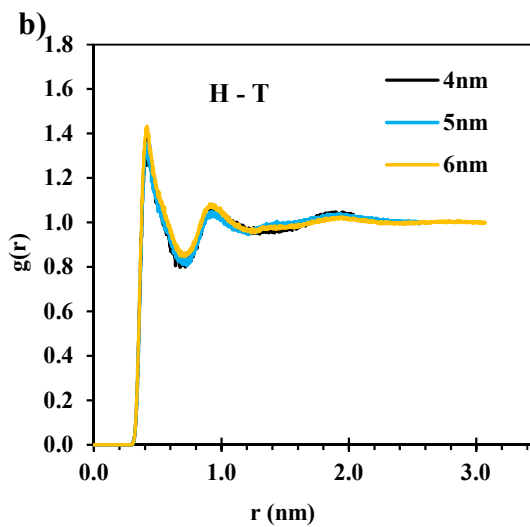
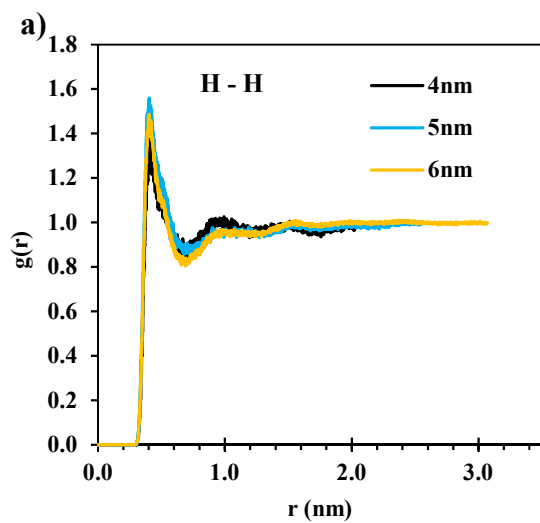


Figure B3.10. Radial distribution function of i-IP monomers for different box sizes and 10 ns of runtime at 550 K and 1 bar: a) head-head, b) head-tail c) all box sizes of 50 ns runtime. Head and tail carbons are labeled in Figure 3.1 and Figure B3.11.

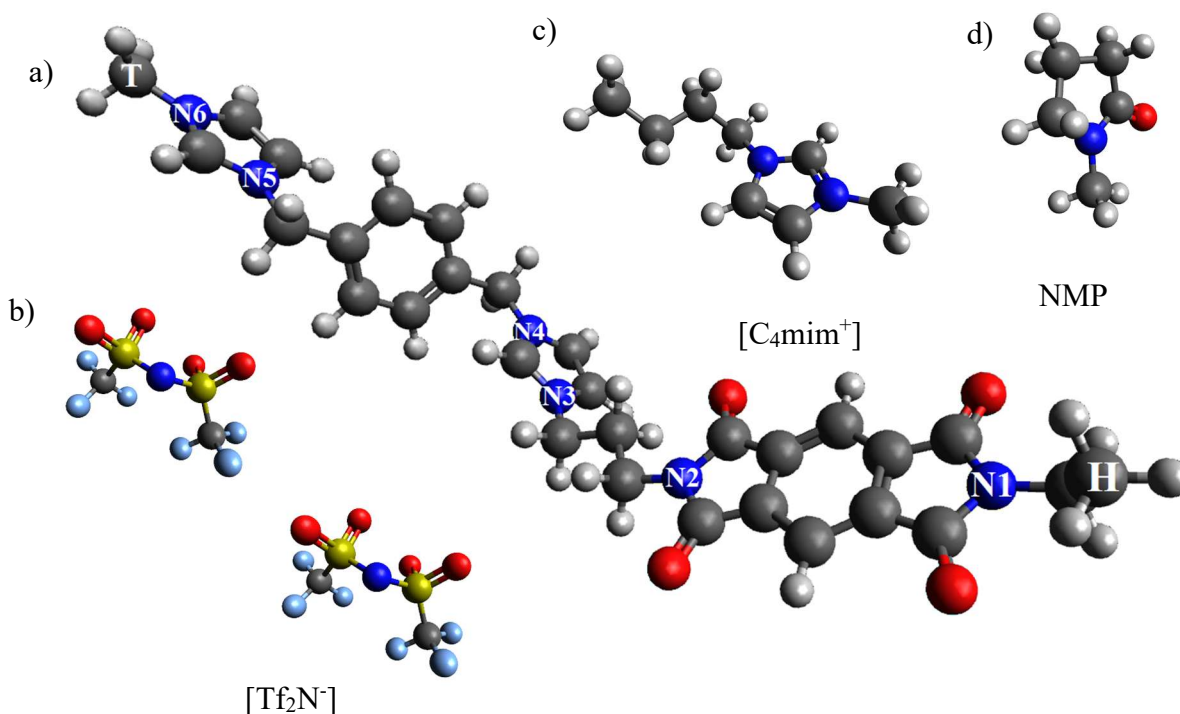


Figure B3.11. Illustration of: a) i-IP monomer; b) [Tf₂N⁻] molecules (2 per i-IP monomer); c) [C₄mim⁺]; and d) NMP structures. Atoms are colored according to their type (N = navy, O = red, S = yellow, C = grey, H = white, and F = light blue). Specific nitrogen sites of the i-IP are labeled for reference, as well as the head (H) and tail (T) designation.

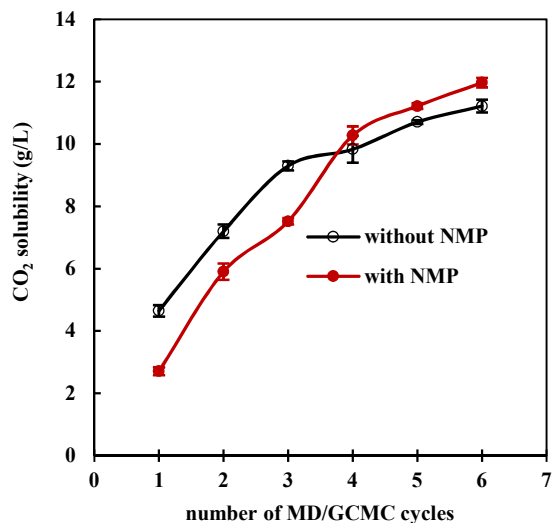


Figure B3.12. Gas solubility comparison for structure preparing without NMP (hollow symbols) and with NMP (filled symbols) in polymerization. All samples contain 200 monomers and the fixed density for both samples is 1.577 g/cm³.

Table B3.2. Henry's law constant for different IL and polymer structures (mol/(L·atm)).^{1,25,59,60}

	[C ₄ mim ⁺][Tf ₂ N ⁻]	i-IP	i-IP + [C ₄ mim ⁺][Tf ₂ N ⁻]	1-ethyl-2- methylimidazole	2-Methyl-1- pentyl-1H- imidazole
CO ₂	0.066 ± 0.002	0.075 ± 0.001	0.066 ± 0.0004	0.090	0.103
CH ₄	0.010 ± 0.0003	0.012 ± 0.001	0.009 ± 0.001	0.008	0.012

Table B3.3. Solubility values for CO₂ and CH₄ from Figure 3.6.

CO ₂ [gr/L]			CH ₄ [gr/L]		
Pressure [bar]	Sim. i-IP	Sim. i-IP + IL	Pressure [bar]	Sim. i-IP	Sim. i-IP + IL
1.569	5.162 ± 0.18	4.227 ± 0.131	1.170	0.203 ± 0.004	0.164 ± 0.009
1.040	4.366 ± 0.067	4.069 ± 0.104	0.777	0.035 ± 0.036	0.092 ± 0.013
0.457	3.420 ± 0.355	3.147 ± 0.343	0.516	0.009 ± 0.007	0.036 ± 0.001
0.202	2.235 ± 0.129	1.675 ± 0.281	0.343	0.002 ± 0.002	0.015 ± 0.001
0.089	1.030 ± 0.289	0.789 ± 0.061	0.227	0.001 ± 0.000	0.009 ± 0.001
0.011	0.203 ± 0.001	0.389 ± 0.191	0.151	0.001 ± 0.001	0.005 ± 0.002
0.001	0.056 ± 0.076	0.159 ± 0.091	0.100	-	0.001 ± 0.000
0.000	0.000 ± 0.001	0.001 ± 0.091	0.020	-	-

References

- (1) Budhathoki, S.; Shah, J. K.; Maginn, E. J. Molecular Simulation Study of the Solubility, Diffusivity and Permselectivity of Pure and Binary Mixtures of CO₂ and CH₄ in the Ionic Liquid 1-n-Butyl-3-methylimidazolium bis(trifluoromethylsulfonyl)imide. *Ind. Eng. Chem. Res.* **2015**, *54*, 8821-8828.
- (2) Aparicio, S.; Atilhan, M. Computational Study of Hexamethylguanidinium Lactate Ionic Liquid: A Candidate for Natural Gas Sweetening. *Energy & Fuels* **2010**, *24*, 4989-5001.
- (3) Chang, H.; Shih, C. M. Simulation and optimization for power plant flue gas CO₂ absorption-stripping systems. *Separ. Sci. Technol.* **2005**, *40*, 877-909.
- (4) Liu, Y. D.; Zhang, L. Z.; Watanasiri, S. Representing vapor-liquid equilibrium for an aqueous MEA-CO₂ system using the electrolyte nonrandom-two-liquid model. *Ind. Eng. Chem. Res.* **1999**, *38*, 2080-2090.
- (5) Dupart, M. S.; Bacon, T. R.; Edwards, D. J. Understanding Corrosion in Alkanolamine Gas Treating Plants. *Hydrocarb. Process* **1993**, *72*, 75-80.
- (6) Peng, X.; Wang, W.; Xue, R.; Shen, Z. Adsorption separation of CH₄/CO₂ on mesocarbon microbeads: Experiment and modeling. *AIChE J.* **2006**, *52*, 994-1003.
- (7) Bai, B. C.; Cho, S.; Yu, H.-R.; Yi, K. B.; Kim, K.-D.; Lee, Y.-S. Effects of aminated carbon molecular sieves on breakthrough curve behavior in CO₂/CH₄ separation. *J. Ind. Eng. Chem.* **2013**, *19*, 776-783.
- (8) Heymans, N.; Alban, B.; Moreau, S.; De Weireld, G. Experimental and theoretical study of the adsorption of pure molecules and binary systems containing methane, carbon monoxide, carbon dioxide and nitrogen. Application to the syngas generation. *Chem. Eng. Sci.* **2011**, *66*, 3850-3858.
- (9) García, E. J.; Mowat, J. P. S.; Wright, P. A.; Pérez-Pellitero, J.; Jallut, C.; Pirngruber, G. D. Role of Structure and Chemistry in Controlling Separations of CO₂/CH₄ and CO₂/CH₄/CO Mixtures over Honeycomb MOFs with Coordinatively Unsaturated Metal Sites. *J. Phys. Chem. C* **2012**, *116*, 26636-26648.
- (10) Li, S.; Chung, Y. G.; Snurr, R. Q. High-Throughput Screening of Metal-Organic Frameworks for CO₂ Capture in the Presence of Water. *Langmuir* **2016**, *32*, 10368-10376.
- (11) Morishige, K. Adsorption and Separation of CO₂/CH₄ on Amorphous Silica Molecular Sieve. *J. Phys. Chem. C* **2011**, *115*, 9713-9718.
- (12) Slater, A. G.; Cooper, A. I. Porous materials. Function-led design of new porous materials. *Science* **2015**, *348*, aaa8075-8010.
- (13) McKeown, N. B.; Budd, P. M. Polymers of intrinsic microporosity (PIMs): organic materials for membrane separations, heterogeneous catalysis and hydrogen storage. *Chem. Soc. Rev.* **2006**, *35*, 675-683.
- (14) Xiao, Y. C.; Zhang, L. L.; Xu, L.; Chung, T. S. Molecular design of Troger's base-based polymers with intrinsic microporosity for gas separation. *J. Membrane Sci.* **2017**, *521*, 65-72.
- (15) Hart, K. E.; Colina, C. M. Estimating gas permeability and permselectivity of microporous polymers. *J. Membrane Sci.* **2014**, *468*, 259-268.
- (16) Tocci, E.; De Lorenzo, L.; Bernardo, P.; Clarizia, G.; Bazzarelli, F.; McKeown, N. B.; Carta, M.; Malpass-Evans, R.; Friess, K.; Pilnáček, K.; Lanč, M.; Yampolskii, Y. P.; Strarannikova, L.; Shantarovich, V.; Mauri, M.; Jansen, J. C. Molecular Modeling and Gas Permeation Properties of a

Polymer of Intrinsic Microporosity Composed of Ethanoanthracene and Tröger's Base Units. *Macromolecules* **2014**, *47*, 7900-7916.

- (17) Swaidan, R.; Ghanem, B.; Litwiller, E.; Pinnau, I. Physical Aging, Plasticization and Their Effects on Gas Permeation in "Rigid" Polymers of Intrinsic Microporosity. *Macromolecules* **2015**, *48*, 6553-6561.
- (18) Heuchel, M.; Fritsch, D.; Budd, P. M.; McKeown, N. B.; Hofmann, D. Atomistic packing model and free volume distribution of a polymer with intrinsic microporosity (PIM-1). *J. Membrane Sci.* **2008**, *318*, 84-99.
- (19) Budd, P.; Msayib, K.; Tattershall, C.; Ghanem, B.; Reynolds, K.; McKeown, N.; Fritsch, D. Gas separation membranes from polymers of intrinsic microporosity. *J. Membrane Sci.* **2005**, *251*, 263-269.
- (20) Hart, K. E.; Abbott, L. J.; McKeown, N. B.; Colina, C. M. Toward Effective CO₂/CH₄ Separations by Sulfur-Containing PIMs via Predictive Molecular Simulations. *Macromolecules* **2013**, *46*, 5371-5380.
- (21) Chen, Y.-R.; Chen, L.-H.; Chang, K.-S.; Chen, T.-H.; Lin, Y.-F.; Tung, K.-L. Structural characteristics and transport behavior of triptycene-based PIMs membranes: A combination study using ab initio calculation and molecular simulations. *J. Membrane Sci.* **2016**, *514*, 114-124.
- (22) Otani, A.; Zhang, Y.; Matsuki, T.; Kamio, E.; Matsuyama, H.; Maginn, E. J. Molecular Design of High CO₂ Reactivity and Low Viscosity Ionic Liquids for CO₂ Separative Facilitated Transport Membranes. *Ind. Eng. Chem. Res.* **2016**, *55*, 2821-2830.
- (23) Anthony, J. L.; Maginn, E. J.; Brennecke, J. F. Solubilities and thermodynamic properties of gases in the ionic liquid 1-n-butyl-3-methylimidazolium hexafluorophosphate. *J. Phys. Chem. B* **2002**, *106*, 7315-7320.
- (24) Kerle, D.; Ludwig, R.; Geiger, A.; Paschek, D. Temperature Dependence of the Solubility of Carbon Dioxide in Imidazolium-Based Ionic Liquids. *J. Phys. Chem. B* **2009**, *113*, 12727-12735.
- (25) Ramdin, M.; Balaji, S. P.; Vicent-Luna, J. M.; Gutiérrez-Sevillano, J. J.; Calero, S.; de Loos, T. W.; Vlugt, T. J. H. Solubility of the Precombustion Gases CO₂, CH₄, CO, H₂, N₂, and H₂S in the Ionic Liquid [bmim][Tf₂N] from Monte Carlo Simulations. *J. Phys. Chem. C* **2014**, *118*, 23599-23604.
- (26) Finotello, A.; Bara, J. E.; Camper, D.; Noble, R. D. Room-temperature ionic liquids: Temperature dependence of gas solubility selectivity. *Ind. Eng. Chem. Res.* **2008**, *47*, 3453-3459.
- (27) Turner, C. H.; Cooper, A.; Zhang, Z.; Shannon, M. S.; Bara, J. E. Molecular simulation of the thermophysical properties of N-functionalized alkylimidazoles. *J. Phys. Chem. B* **2012**, *116*, 6529-6535.
- (28) Babarao, R.; Dai, S.; Jiang, D. E. Understanding the high solubility of CO₂ in an ionic liquid with the tetracyanoborate anion. *J. Phys. Chem. B* **2011**, *115*, 9789-9794.
- (29) Kerle, D.; Namayandeh Jorabchi, M.; Ludwig, R.; Wohlrab, S.; Paschek, D. A simple guiding principle for the temperature dependence of the solubility of light gases in imidazolium-based ionic liquids derived from molecular simulations. *Phys. Chem. Chem. Phys.* **2017**, *19*, 1770-1780.
- (30) Tomé, L. C.; Gouveia, A. S. L.; Ab Rani, M. A.; Lickiss, P. D.; Welton, T.; Marrucho, I. M. Study on Gas Permeation and CO₂ Separation through Ionic Liquid-Based Membranes with Siloxane-Functionalized Cations. *Ind. Eng. Chem. Res.* **2017**, *56*, 2229-2239.
- (31) Carlisle, T. K.; Wiesenauer, E. F.; Nicodemus, G. D.; Gin, D. L.; Noble, R. D. Ideal CO₂/Light Gas Separation Performance of Poly(vinylimidazolium) Membranes and Poly(vinylimidazolium)-Ionic Liquid Composite Films. *Ind. Eng. Chem. Res.* **2013**, *52*, 1023-1032.
- (32) Mittenthal, M. S.; Flowers, B. S.; Bara, J. E.; Whitley, J. W.; Spear, S. K.; Roveda, J. D.; Wallace, D. A.; Shannon, M. S.; Holler, R.; Martens, R.; Daly, D. T. Ionic Polyimides: Hybrid Polymer

Architectures and Composites with Ionic Liquids for Advanced Gas Separation Membranes. *Ind. Eng. Chem. Res.* **2017**, *56*, 5055-5069.

(33) Kupgan, G.; Liyana-Arachchi, T. P.; Colina, C. M. Pore size tuning of poly(styrene-co-vinylbenzyl chloride-co-divinylbenzene) hypercrosslinked polymers: Insights from molecular simulations. *Polymer* **2016**, *99*, 173-184.

(34) Larsen, G. S.; Lin, P.; Hart, K. E.; Colina, C. M. Molecular Simulations of PIM-1-like Polymers of Intrinsic Microporosity. *Macromolecules* **2011**, *44*, 6944-6951.

(35) Tian, Z.; Mahurin, S. M.; Dai, S.; Jiang, D. E. Ion-Gated Gas Separation through Porous Graphene. *Nano Lett.* **2017**, *17*, 1802-1807.

(36) Vicent-Luna, J. M.; Luna-Triguero, A.; Calero, S. Storage and Separation of Carbon Dioxide and Methane in Hydrated Covalent Organic Frameworks. *J. Phys. Chem. C* **2016**, *120*, 23756-23762.

(37) Raeissi, S.; Peters, C. J. Carbon Dioxide Solubility in the Homologous 1-Alkyl-3-methylimidazolium Bis(trifluoromethylsulfonyl)imide Family. *J. Chem. Eng. Data* **2009**, *54*, 382-386.

(38) Carvalho, P. J.; Álvarez, V. H.; Marrucho, I. M.; Aznar, M.; Coutinho, J. A. P. High pressure phase behavior of carbon dioxide in 1-butyl-3-methylimidazolium bis(trifluoromethylsulfonyl)imide and 1-butyl-3-methylimidazolium dicyanamide ionic liquids. *J. Supercrit. Fluid.* **2009**, *50*, 105-111.

(39) Aki, S. N. V. K.; Mellein, B. R.; Saurer, E. M.; Brennecke, J. F. High-pressure phase behavior of carbon dioxide with imidazolium-based ionic liquids. *J. Phys. Chem. B* **2004**, *108*, 20355-20365.

(40) Carvalho, P. J.; Coutinho, J. o. A. P. On the Nonideality of CO₂ Solutions in Ionic Liquids and Other Low Volatile Solvents. *J. Phys. Chem. Letters* **2010**, *1*, 774-780.

(41) Singh, R.; Marin-Rimoldi, E.; Maginn, E. J. A Monte Carlo Simulation Study To Predict the Solubility of Carbon Dioxide, Hydrogen, and Their Mixture in the Ionic Liquids 1-Alkyl-3-methylimidazolium bis(trifluoromethanesulfonyl)amide ([C_nmim⁺][Tf₂N⁻], n= 4, 6). *Ind. Eng. Chem. Res.* **2015**, *54*, 4385-4395.

(42) Becke, A. D. Density-functional thermochemistry. III. The role of exact exchange. *J. Chem. Phys.* **1993**, *98*, 5648-5652.

(43) Frisch, M. J.; Trucks, G. W.; Schlegel, H. B.; Scuseria, G. E.; Robb, M. A.; Cheeseman, J. R.; Scalmani, G.; Barone, V.; Mennucci, B.; Petersson, G. A.; Nakatsuji, H.; Caricato, M.; Li, X.; Hratchian, H. P.; Izmaylov, A. F.; Bloino, J.; Zheng, G.; Sonnenberg, J. L.; Hada, M.; Ehara, M.; Toyota, K.; Fukuda, R.; Hasegawa, J.; Ishida, M.; Nakajima, T.; Honda, Y.; Kitao, O.; Nakai, H.; Vreven, T.; Montgomery Jr., J. A.; Peralta, J. E.; Ogliaro, F.; Bearpark, M. J.; Heyd, J.; Brothers, E. N.; Kudin, K. N.; Staroverov, V. N.; Kobayashi, R.; Normand, J.; Raghavachari, K.; Rendell, A. P.; Burant, J. C.; Iyengar, S. S.; Tomasi, J.; Cossi, M.; Rega, N.; Millam, N. J.; Klene, M.; Knox, J. E.; Cross, J. B.; Bakken, V.; Adamo, C.; Jaramillo, J.; Gomperts, R.; Stratmann, R. E.; Yazyev, O.; Austin, A. J.; Cammi, R.; Pomelli, C.; Ochterski, J. W.; Martin, R. L.; Morokuma, K.; Zakrzewski, V. G.; Voth, G. A.; Salvador, P.; Dannenberg, J. J.; Dapprich, S.; Daniels, A. D.; Farkas, Ö.; Foresman, J. B.; Ortiz, J. V.; Cioslowski, J.; Fox, D. J.: Gaussian 09. Gaussian, Inc.: Wallingford, CT, USA, 2009.

(44) Lopes, J. N. C.; Padua, A. A. H. Molecular force field for ionic liquids composed of triflate or bistriflylimide anions. *J. Phys. Chem. B* **2004**, *108*, 16893-16898.

(45) Lopes, J. N. C.; Deschamps, J.; Padua, A. A. H. Modeling ionic liquids using a systematic all-atom force field. *J. Phys. Chem. B* **2004**, *108*, 2038-2047.

(46) Aparicio, S.; Alcalde, R.; Davila, M. J.; Garcia, B.; Leal, J. M. Measurements and predictive models for the N-methyl-2-pyrrolidone/water/methanol system. *J. Phys. Chem. B* **2008**, *112*, 11361-11373.

- (47) Potoff, J. J.; Siepmann, J. I. Vapor-liquid equilibria of mixtures containing alkanes, carbon dioxide, and nitrogen. *AIChE J.* **2001**, *47*, 1676-1682.
- (48) Trinh, T. T.; Vlugt, T. J.; Kjelstrup, S. Thermal conductivity of carbon dioxide from non-equilibrium molecular dynamics: a systematic study of several common force fields. *J. Chem. Phys.* **2014**, *141*, 134504-134507.
- (49) Martinez, L.; Andrade, R.; Birgin, E. G.; Martinez, J. M. PACKMOL: a package for building initial configurations for molecular dynamics simulations. *J. Comput. Chem.* **2009**, *30*, 2157-2164.
- (50) Van Der Spoel, D.; Lindahl, E.; Hess, B.; Groenhof, G.; Mark, A. E.; Berendsen, H. J. GROMACS: fast, flexible, and free. *J. Comput. Chem.* **2005**, *26*, 1701-1718.
- (51) Essmann, U.; Perera, L.; Berkowitz, M. L.; Darden, T.; Lee, H.; Pedersen, L. G. A smooth particle mesh Ewald method. *J. Chem. Phys.* **1995**, *103*, 8577-8593.
- (52) Hoover, W. G. Canonical dynamics: Equilibrium phase-space distributions. *Phys. Rev. A* **1985**, *31*, 1695-1697.
- (53) Parrinello, M.; Rahman, A. Crystal Structure and Pair Potentials: A Molecular-Dynamics Study. *Phys. Rev. Lett.* **1980**, *45*, 1196-1199.
- (54) Abbott, L. J.; Hart, K. E.; Colina, C. M. Polymatic: a generalized simulated polymerization algorithm for amorphous polymers. *Theor. Chem. Acc.* **2013**, *132*, 1334/1331-1334/1319.
- (55) Karayiannis, N. C.; Mavrantzas, V. G.; Theodorou, D. N. Detailed atomistic simulation of the segmental dynamics and barrier properties of amorphous poly(ethylene terephthalate) and poly(ethylene isophthalate). *Macromolecules* **2004**, *37*, 2978-2995.
- (56) Theodorou, D. N.; Suter, U. W. Detailed Molecular-Structure of a Vinyl Polymer Glass. *Macromolecules* **1985**, *18*, 1467-1478.
- (57) Shah, J. K.; Maginn, E. J. A general and efficient Monte Carlo method for sampling intramolecular degrees of freedom of branched and cyclic molecules. *J. Chem. Phys.* **2011**, *135*, 134121-134111.
- (58) Gelb, L. D.; Gubbins, K. E. Pore size distributions in porous glasses: A computer simulation study. *Langmuir* **1999**, *15*, 305-308.
- (59) Raeissi, S.; Peters, C. J. High pressure phase behaviour of methane in 1-butyl-3-methylimidazolium bis(trifluoromethylsulfonyl)imide. *Fluid Phase Equilibr.* **2010**, *294*, 67-71.
- (60) Liu, H.; Zhang, Z.; Bara, J. E.; Turner, C. H. Electrostatic potential within the free volume space of imidazole-based solvents: insights into gas absorption selectivity. *J. Phys. Chem. B* **2014**, *118*, 255-264.

4. MOLECULAR ANALYSIS OF SELECTIVE GAS ADSORPTION WITHIN COMPOSITES OF IONIC POLYIMIDES AND IONIC LIQUIDS AS GAS SEPARATION MEMBRANES³

4.1 Introduction

Carbon dioxide is one of the most well-known greenhouse gases with many industrial emission sources contributing to the detriment of the atmosphere. To reduce and control this greenhouse gas emission, carbon capture during pre-combustion has been successfully applied in multiple natural gas sweetening processes.¹ Although amine-based solvents, such as monoethanolamine (MEA) exhibit multiple disadvantages including corrosion, volatility, toxicity, and high-energy demand for recovery, carbon capture processes still heavily depend on typical MEA solvents during CO₂ absorption due to the high cost or low efficiency of other alternatives.² The design of alternative materials for CO₂ capture is of high importance due to a growing need for control of CO₂ emissions to the atmosphere and for increasing the efficiency of energy supply lines by reducing CO₂ in pre-combustion gases. Several different adsorbents such as activated carbons,³ zeolites,⁴ metal organic frameworks (MOFs),⁵ and covalent organic frameworks (COFs)⁶ have been widely studied for CO₂ adsorption. These materials provide a high capacity for gas adsorption, but they typically suffer from other limitations (selectivity, cost, or stability).

In addition to these porous materials, different types of ionic liquid (IL) solvents have also been studied and proposed as effective alternatives for CO₂ absorption.⁷ These IL solvents

³ This work was submitted to the Chemical Physics with submission number of CHEMPHYS_2018_387.

have previously been shown to be effective at dissolving CO₂, and they tend to possess high thermal and physical stability and low vapor pressure. In particular, imidazolium-based ILs have received a great deal of attention, due to their high solubility and selectivity for CO₂ in post-combustion capture and natural gas sweetening.⁸⁻¹⁴ However, their high cost and high viscosity as well as their limited adsorption capacity for CO₂ render them to be uncompetitive with traditional gas absorbents used in industrial scale applications.^{8,9}

There have been some previous efforts to circumvent the inherent IL performance limitations. For instance, dissolving ILs in an amorphous structure of polymers and crystal structures consisting of MOFs¹¹ and COFs¹⁵ can alleviate the low capacity of ILs by providing more void volume.¹⁴ Recently, to explore the directed orientation of IL molecules and the resulting effect on gas separation, others have investigated the properties of ILs confined within solid pores.^{5,8,14,16-18} In this work, a thick layer of IL solvent was confined between solid surfaces,¹⁹ and gas diffusion in that confined layer was studied as well as the influence of confinement on CO₂ solubility.^{14,20,21} Budhathoki, et al. used molecular dynamics simulations to study CO₂ solubility selectivity, diffusion selectivity, and permselectivity from binary mixtures of CO₂/CH₄ and CO₂/H₂ within a [C₄mim⁺][Tf₂N⁻] confined IL solvent.⁸ The IL was confined within graphite nanopores of 2 to 5 nm in diameter. The ILs confined within the pores demonstrated enhanced permselectivity of CO₂ (compared to the empty nanopores), but the diffusivity of all gas species decreased, relative to bulk ILs. Expelling captured CO₂ during adsorption and absorption and recycling the adsorbent and absorbent liquids is already a cost effective process in separation columns. However, membrane separation mitigates the need for frequent adsorbent replacement and absorbent recovery by providing continuous gas separation and purification.²²⁻²⁴

Porous organic polymers²⁵⁻²⁷ have been considered in gas separation studies due to their stability,^{28,29} large surface area,^{30,31} and fine-tuned microporosity resulting from the voids created in their rigid molecular structure (due to frustrated polymer chain packing).³²⁻³⁵ Supported ionic liquid membranes (SILMs)³⁶ and polymers of intrinsic microporosity (PIMs)^{23,37} are now receiving much attention due to the combined advantages of both ILs and membranes in gas separation.^{24,38-41} For instance, CO₂ mass transfer can be significantly enhanced when ILs are dissolved into polymers and porous solid structures.^{5,42} Also, nitrogen-rich polymer building blocks can help promote CO₂ uptake within amorphous microporous polymers (AMPs) by increasing the heat of adsorption.^{33,43}

Ionic polyimides (i-IPs) are one of these promising polymers for membrane-based CO₂ separations (pre-combustion, gas sweetening, and CO₂ post-combustion capture).^{42,44} This novel class of materials, like poly(ionic liquids)s (PILs),^{45,46} contain ionic liquid species in the monomer unit. However, the i-IP monomer structure is composed of an IL segment and an organic linker to provide an additional degree of structural and chemical design. In the i-IP structure, the 1-n-butyl-3-methylimidazolium ([C₄mim⁺]) molecules are connected to the pyromellitic dianhydride (PMDA) as an organic linker to construct the monomer of the ionic polyimide molecule. PMDA was chosen as an organic ligand because of its low cost and ability to form helical nanostructures.⁴⁷ Positively charged sites in the monomer, due to the [C₄mim⁺] units, are compensated by a balance of anions. Each monomer contains two cations in the backbone, along with two balancing anion molecules, as illustrated in **Figure 4.1**. The neat polymer molecule structure is prepared by repeating the mentioned monomer, and the chemistry prevents any additional crosslinking among neighboring chains. Composite structures were prepared by dispersing IL molecules inside the i-IP polymer in different concentrations.

The previous experimental work of the Bara group reports the significantly enhanced CO₂ permeability (up to 2200%) by adding [C₄mim⁺][Tf₂N⁻] to the neat i-PI system. The high permeability in the composite system (i-IP + IL) was responsible for the diffusivity enhancement of CO₂ (up to 2300%), while the adsorption selectivity was found to be slightly decreased. In order to characterize the molecular-level behavior of different gas adsorbents (CO₂, CH₄, N₂) in this system, our previous work⁴⁴ focused on pure gas solubility in [Tf₂N⁻]-based structures. However, due to the intriguing potential for creating different composites by combining different ILs with the i-PI backbone, the current work explores the selective adsorption behavior of binary gas mixtures with a range of different i-PI + IL composite materials. For instance, adding bulkier anions may increase the void volume of the composite and specific interactions with different anions may be used to tune the selectivity. In the current study, the prepared composite structures contain i-IPs and different ILs with [C₄mim⁺] as the cation in combination with one of the following anions: bis(trifluoromethylsulfonyl)imide ([Tf₂N⁻]), tetrafluoroborate ([BF₄⁻]), and hexafluorophosphate ([PF₆⁻]). Molecular dynamic (MD) calculations and grand canonical Monte Carlo (GCMC) simulations are used to study structural changes of the ionic polyimides and their composites during binary mixtures of CO₂/CH₄ and CO₂/N₂ adsorption by analyzing the fractional free volume (FFV), pore size distribution (PSD), and the surface area.

The neat i-IP with [BF₄⁻] as the counter ion shows high CO₂/CH₄ selectivity at 1 bar and 294 K, and this is also observed when additional [C₄mim⁺][BF₄⁻] is added to generate the composite material. A high CO₂ solubility is found with the [PF₆⁻]-based i-IP and i-IP + IL composites. The high solubility is accompanied by a large calculated surface area within the materials and a larger fraction of wider pores, while the FFV is not a very sensitive indicator of

the solubility. Among the three different types of anions studied in this work, the $[\text{PF}_6^-]$ -based structures showed the strongest interaction with gas molecules, regardless of gas type.

4.2 Simulation Details

Our simulation procedure is comprised of several different steps in order to generate the initial configurations, relax the system, perform gas adsorption, and analyze the dominant molecular-level interactions. First, quantum mechanical calculations are used to assign partial charges on the atom sites of the i-IP monomer units (illustrated in **Figure 4.1**) using the B3LYP functional⁴⁸ and a 6-31G(d,p) basis set in Gaussian09.⁴⁹ Then molecular dynamics (MD) simulations are used to prepare the relaxed initial structure of the neat i-IP and i-IP + IL composite. This involves a polymerization scheme followed by several stages of structural relaxation. The initial system also contains an N-methyl-2-pyrrolidone (NMP) solvent, which is eventually removed and replaced with the IL species following polymerization. This is intended to mimic the experimental synthesis procedure during the polymerization and prepare enough vacant space for IL molecules by deleting NMP molecules.⁴² Finally, using an iterative combination of molecular dynamics and GCMC simulations, the selectivity of CO_2/CH_4 and CO_2/N_2 is modeled over a wide range of concentrations within the neat i-IP and different combinations of i-IP + IL composite materials. The details of each stage are described below, which follows our previous approach.⁴⁴

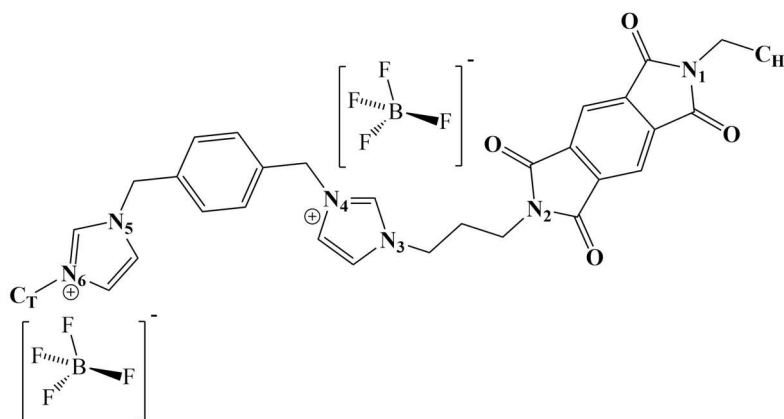


Figure 4.1. Representative monomer structure of a neat i-IP. The anion shown is $[\text{BF}_4]^-$. Specific nitrogen sites of the i-IP are labeled for reference, as well as the head (C_H) and tail (C_T) designation.

The details of the electronic structure calculations and geometric optimization of the monomers, as well as the partial charge calculation and polymerization were provided in our previous work.⁴⁴ Force field parameters for $[\text{C}_4\text{mim}^+]$, $[\text{Tf}_2\text{N}^-]$, $[\text{BF}_4^-]$, and $[\text{PF}_6^-]$ were taken from Lopez, et al,⁵⁰⁻⁵² while parameters for NMP molecules were extracted from Aparicio, et al.⁵³ The TraPPE⁵⁴ force fields for CO_2 , CH_4 , and N_2 were used, based on the previous experience of others modeling gas adsorption in ILs.⁵⁴⁻⁵⁷ The Lorentz-Berthelot mixing rules were used for cross-term interactions.

Following the assignment of the force fields, the i-IP and i-IP + IL systems were constructed and conditioned according to the following default procedure (with specific variations noted later in the text):

- g) Ionic polyimide monomers were inserted into the simulation box using PACKMOL,⁵⁸ followed by energy minimization using the steepest descent algorithm.⁵⁹
- h) In addition to the monomers, NMP molecules were also inserted at three different ratios: 1:4, 1:6, and 1:8 (monomer:NMP) in order to produce more replica of the polymer

structure. The experiments used a ratio of approximately 1:60 during polymerization.⁴²

The solvent effect on porous structure has been studied in our previous work.⁴⁴

- i) The monomer + NMP molecules were relaxed with MD simulations using a cycle of canonical ensemble (NVT) simulations to increase temperature up to 2000 K, followed by isothermal-isobaric (NPT) ensemble simulations at high temperature and pressure. After, the systems were slowly quenched to 294 K.
- j) The monomer units were polymerized, using a nearest-neighbor algorithm (described in previous work),⁴⁴ followed by additional relaxation with MD.
- k) The NMP was then removed from the system, and the i-IP + IL samples were generated by inserting the IL molecules in the cavities left by the NMP molecules, again using PACKMOL.
- l) A neat i-IP and a composite with the [Tf₂N⁻] anion from the previous step were used to produce [BF₄⁻] and [PF₆⁻] anion based i-IP and i-IP + IL composites. In this step, all [Tf₂N⁻] anions were replaced with the desired anions, while keeping the polymer structure intact. This approach ensures that the i-PI backbone is consistent (same number of polymers and chain lengths), and only the anion composition is changed.
- m) Both neat i-IP and i-IP + IL systems were further equilibrated and relaxed via NVT and NPT cycles as mentioned in step (c), until a final temperature of 294 K and a pressure of 1 bar were reached.

All of the MD simulations were performed with the GROMACS 5.0 simulation package.⁶⁰ The Lennard-Jones potential and electrostatic interactions were calculated with a cut-off distance of 14.0 Å, and the smooth particle mesh Ewald sum (SPME)⁶¹ method was implemented to calculate long-range electrostatic interactions, with a Fourier spacing of 1.6 Å.

The Nose-Hoover thermostat⁶² was used to maintain the temperature and the Parrinello-Rahman⁶³ barostat was used to maintain the pressure, and the time step was 1 fs. In the MD simulations, periodic boundary conditions were implemented in all three dimensions.

In order to estimate the reproducibility of our results, three different independent replicates were separately simulated and evaluated in our structural and adsorption property analysis. A summary of the different i-IP systems is described in Table 1.

Table 4.1. Summary of different i-IP systems (a → h) simulated.

description (including approximate box length)	# monomers	# NMP	polymer chain lengths*	Average M_w (g/mol)
(a) neat, 6 nm (sample 1)	200	0	17, 8(2), 5(2), 4(6), 3(11), 2(18), 1(64)	5484.3
(b) neat, 6 nm (sample 2)	200	0	76, 56, 29, 20, 15, 2(2)	31338.9
(c) neat, 6 nm (sample 4)	200	0	131, 32, 19, 18	54843.1
(d) neat, 6 nm (sample 5)	200	0	94, 30, 28, 16, 15, 8, 5, 4	27421.6
(e) neat, 6 nm (sample 3)	200	800	80, 41, 40, 20, 13, 6	36562.1
(f) composite, 6.8 nm (sample 1)	200 (+ 200 IL)	800	80, 41, 40, 20, 13, 6	36562.1
(g) composite, 6.8 nm (sample 2)	200 (+ 200 IL)	1200	81, 58, 57, 2(2)	43747.5
(h) composite, 6.8 nm (sample 3)	200 (+ 200 IL)	1600	178, 14, 8	73124.1

*Numbers inside the parentheses represent the number of different chains with the same polymer chain length.

The density of each sample (designated as (a) through (h) from Table 1) is reported in Table 2. For instance, the (a) sample of the $[\text{Tf}_2\text{N}^-]$ -based neat polymer has the same polymer chain length as the (a) sample in both the $[\text{BF}_4^-]$ -based and the $[\text{PF}_6^-]$ -based neat polymer as well. The only difference is the type of the anion used to create the neutral monomer (**Figure 4.1**).

Table 4.2. Density (g/cm³) of neat i-IP and composite of i-IP + IL samples at 1 bar and 294 K. The columns #1 to #5 indicate different independent replicates.

	Mol% IL	#1	#2	#3	#4	#5	Average density
[Tf ₂ N ⁻]-based	neat i-IP	1.643 (a)*	1.605 (b)	1.603(e)	1.602 (c)	1.604 (d)	1.612 ± 0.018
	i-IP + 50% IL	1.584 (f)	1.583 (g)	1.585 (h)	-	-	1.584 ± 0.001
	i-IP + 30% IL	1.594 (f)	1.593 (g)	1.595 (h)	-	-	1.594 ± 0.001
	i-IP + 10% IL	1.600 (f)	1.599 (g)	1.599 (h)	-	-	1.600 ± 0.001
[BF ₄]-based	neat i-IP	1.386 (a)	1.369 (b)	1.372 (e)	1.369 (c)	1.368 (d)	1.373 ± 0.008
	i-IP + 50% IL	1.325 (f)	1.322 (g)	1.326 (h)	-	-	1.324 ± 0.002
	i-IP + 30% IL	1.347 (f)	1.347 (g)	1.346 (h)	-	-	1.347 ± 0.001
	i-IP + 10% IL	1.363 (f)	1.361 (g)	1.362 (h)	-	-	1.362 ± 0.001
[PF ₆]-based	neat i-IP	1.489 (a)	1.474 (b)	1.474 (e)	-	-	1.479 ± 0.009
	i-IP + 50% IL	1.446 (f)	1.444 (g)	1.447 (h)	-	-	1.446 ± 0.001
	i-IP + 30% IL	1.458 (f)	1.465 (g)	1.460 (h)	-	-	1.461 ± 0.003
	i-IP + 10% IL	1.466 (f)	1.470 (g)	1.478 (h)	-	-	1.471 ± 0.006

**the letter in the parentheses corresponds to the polymer system in Table 1.*

Once the neat i-IP and i-IP + IL samples were prepared, we used the Cassandra simulation package to run GCMC simulations of gas adsorption.⁶⁴ Each single sample after preparation was followed by 15 MD/GCMC simulation cycles at 1 bar and 294 K. These relaxation cycles are important, since the adsorbed gas leads to changes in the polymer structure that shift (increase) the predicted equilibrium adsorption. During the GCMC simulations, the polymer and IL molecules were held rigid, while the adsorbate molecules were subject to at least 3×10^6 MC steps (33% insertion, 33% deletion, 17% translation, and 17% rotation). In order to improve sampling, these GCMC simulations were iteratively combined with MD simulations to further relax the system configuration. For instance, after finishing one stage of GCMC

simulations, the resulting structure (including the gas molecules) was subjected to a short NVT MD relaxation process of 1 ns at the same temperature (294 K). The final structure after these 15 MD/GCMC cycles of equilibration was used for calculating gas selectivity with production runs of 20×10^6 GCMC steps used to calculate averages and error bars. Additional tests were performed with increased MD/GCMC cycles to ensure adequate equilibration and structural relaxation (see **Figure C4.10 to C4.12**), and 15 cycles were generally found to be sufficient.

Gas selectivity was calculated for two binary gas mixtures (CO_2/CH_4 and CO_2/N_2), each corresponding to four different gas-phase concentrations (0.5/0.5, 0.2/0.8, 0.1/0.9, 0.05/0.95) and a total pressure of 1 bar and 294 K. The adsorption selectivity is defined as $S = (x_A/y_A)/(x_B/y_B)$, where x_i is the mole fraction of component i in the adsorbed phase and y_i is the mole fraction in the gas phase. Two extra samples (#4 and #5) were generated and tested only for $[\text{Tf}_2\text{N}^-]$ and $[\text{BF}_4^-]$ anions, since the $[\text{Tf}_2\text{N}^-]$ -based structure showed very high variability for the CO_2/N_2 mixture selectivity, and the $[\text{BF}_4^-]$ -based structure showed very high selectivity for CO_2/CH_4 , so these extra samples were used to improve confidence.

In order to connect the i-IP and i-IP + IL composite adsorption properties to the underlying molecular configurations, several different structural analyses were performed, which were originally applied to characterize solid adsorbents. Using the approaches of Gelb and Gubbins,⁶⁵ we calculated the theoretical FFV, PSD⁶⁶, and exposed surface area for our i-IP and i-IP + IL composite models. Similar information could be generated from publicly available analysis tools like Poreblazer from the Sarkisov group.⁶⁷ The structural analyses was performed by including all atomic sites during the analyses, with the Lennard-Jones diameters used to define the molecular surfaces, and in the case of the surface area, the probe diameter is 4.0 Å. Also, the radial distribution function (RDF) of key interaction sites in the system are analyzed.

4.3 Results and Discussion

4.3.1 Gas Solubility

Gas solubility results for different i-IP + IL combinations are reported in **Figure C4.10** to **C4.12**, corresponding to different stages along the MD/GCMC relaxation steps. As mentioned previously, selected systems were run for 15 additional MD/GCMC cycles (also included in **Figures C4.10** to **C4.12**) to confirm equilibrium saturation values. As **Figure 4.2** shows, the composite structures of the i-PI + ILs show lower gas solubility, regardless of the anion, as compared to the neat polymer (and this is similar to the experimental systems). In the experimental [Tf₂N⁻]-based i-IP + IL tests, the CO₂ solubility decreases by 7% and N₂ solubility decreases by 24%, while the CH₄ solubility is relatively constant, as compared to the neat i-IP.⁴² Although not experimentally tested, the simulated CO₂ solubility for the different anion derivatives show the following order: [PF₆⁻] > [BF₄⁻] > [Tf₂N⁻]. This trend is also observed for the other gases (N₂ and CH₄) studied in this work. However, the bulk ILs (no i-PI present) show a different trend for CO₂ solubility, as shown in Tables S-1 and S-2 (which compares the solubility and selectivity of several different types of porous adsorbents and ILs from the literature). The CO₂ solubility of the bulk [Tf₂N⁻]-based ILs is highest among our selected group of three anions. To explore the origin of the IL effect on solubility in the i-PI + IL composite, several different structural analyses were implemented and discussed in the following.

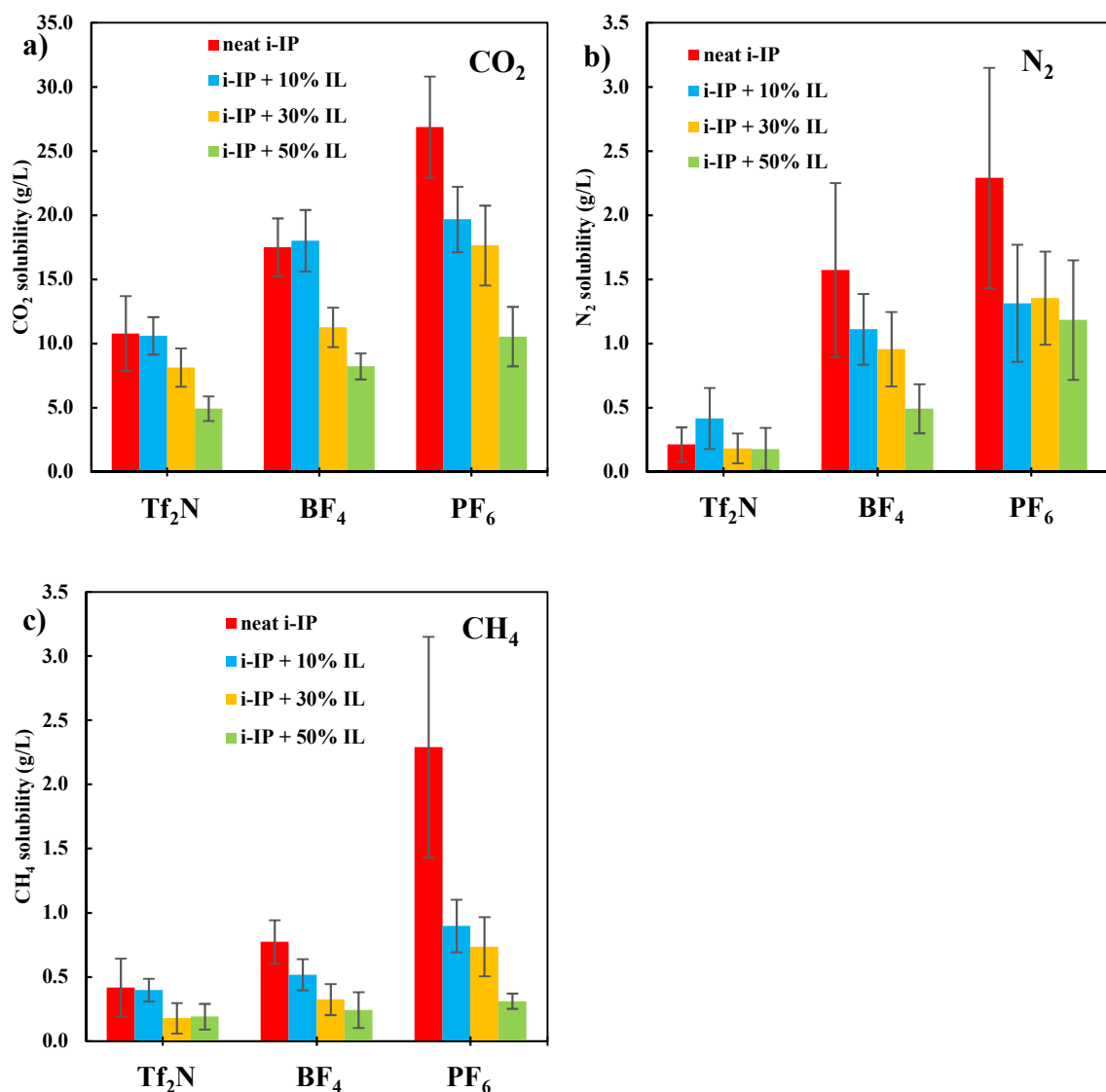


Figure 4.2. Calculated pure gas solubility at 294 K and 1 bar within neat i-IP and i-IP+IL composites. a) CO₂, b) N₂, and c) CH₄. It should be noted that the scale for CO₂ solubility is ten times higher than the other gases.

4.3.2 Gas Selectivity

The results of gas selectivity for CO₂/CH₄ and CO₂/N₂ mixtures are reported in **Figures 4.3** and **4.4**. While [PF₆⁻]-based structures showed higher gas solubility for both neat i-IP and i-IP + IL systems, the [BF₄⁻]-based structures show the highest CO₂/CH₄ gas selectivity, which is most relevant to natural gas sweetening applications. To further evaluate [BF₄⁻]-based structures

and check the reproducibility of the extracted results, two extra samples were prepared. The $[\text{PF}_6^-]$ -based structures showed the second best results for CO_2/CH_4 gas selectivity (adding IL in the i-PI enhances the selectivity, while in $[\text{Tf}_2\text{N}^-]$ -based structures, adding the IL reduces the gas selectivity of CO_2/CH_4 . **Figure 4.3** shows a different pattern for gas selectivity in $[\text{BF}_4^-]$ -based structures. Neat $[\text{BF}_4^-]$ -based i-PI polymers show higher selectivity than composite structures with 10% and 30% IL addition. From neat polymer to 10% of IL composite, the selectivity sharply decreases in $[\text{BF}_4^-]$ -based composites. However, upon increasing IL concentration the selectivity will rise back to the neat polymer selectivity value, which occurs at 50% IL concentration.

The gas selectivity calculations of CO_2/N_2 mixtures (**Figure 4.4**) show higher uncertainty in comparison to the CO_2/CH_4 results, and this is primarily due to the small number of N_2 species present in the system. The high uncertainty for CO_2/N_2 persists even after doubling the number of GCMC simulation steps. In almost all of the different anion based structures, adding IL does not have a significant positive effect on the gas selectivity for CO_2/N_2 mixtures.

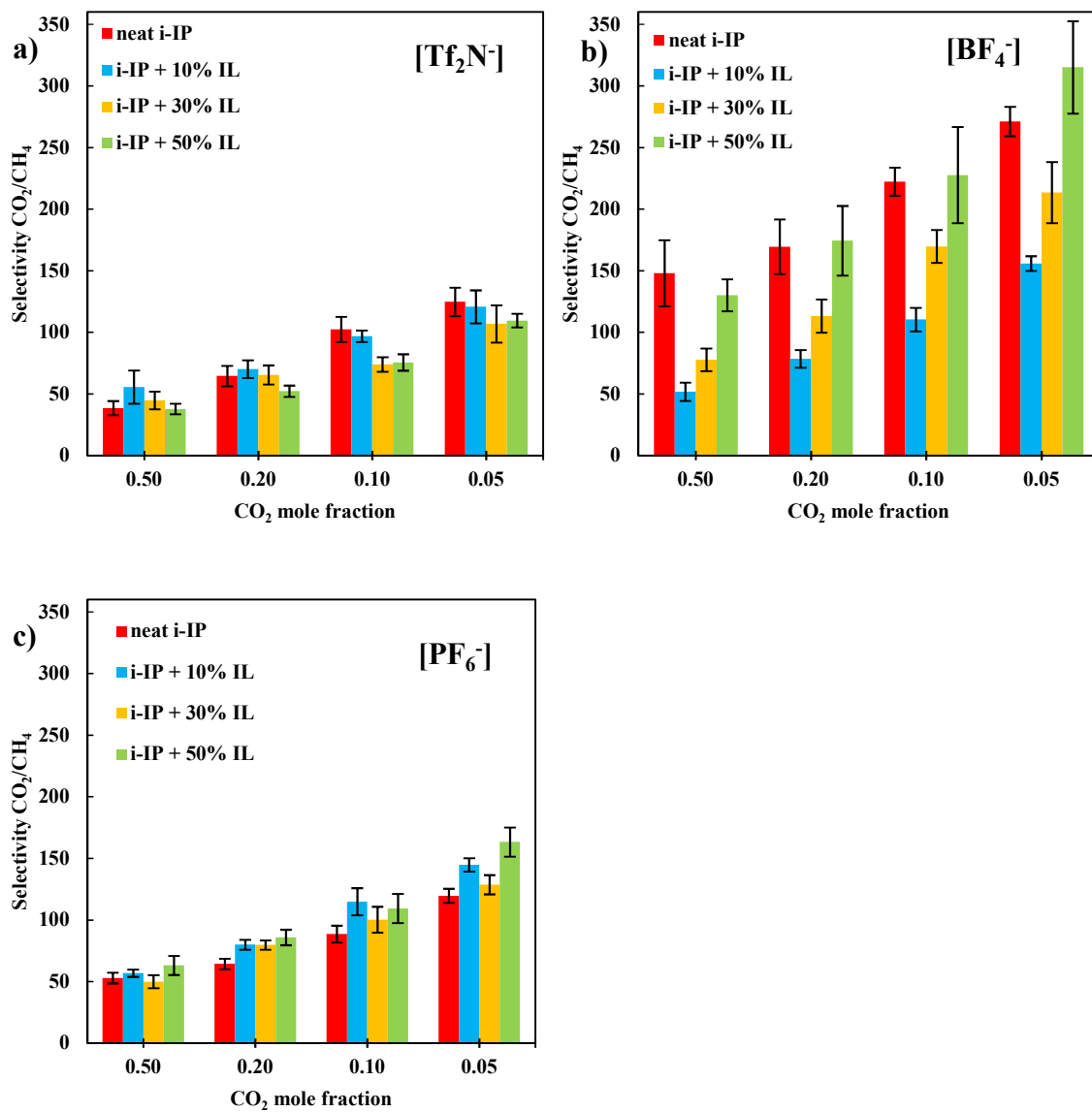


Figure 4.3. Predicted CO₂/CH₄ selectivity for: a) [Tf₂N⁻], b) [BF₄⁻], and c) [PF₆⁻] at 294 K and 1 bar.

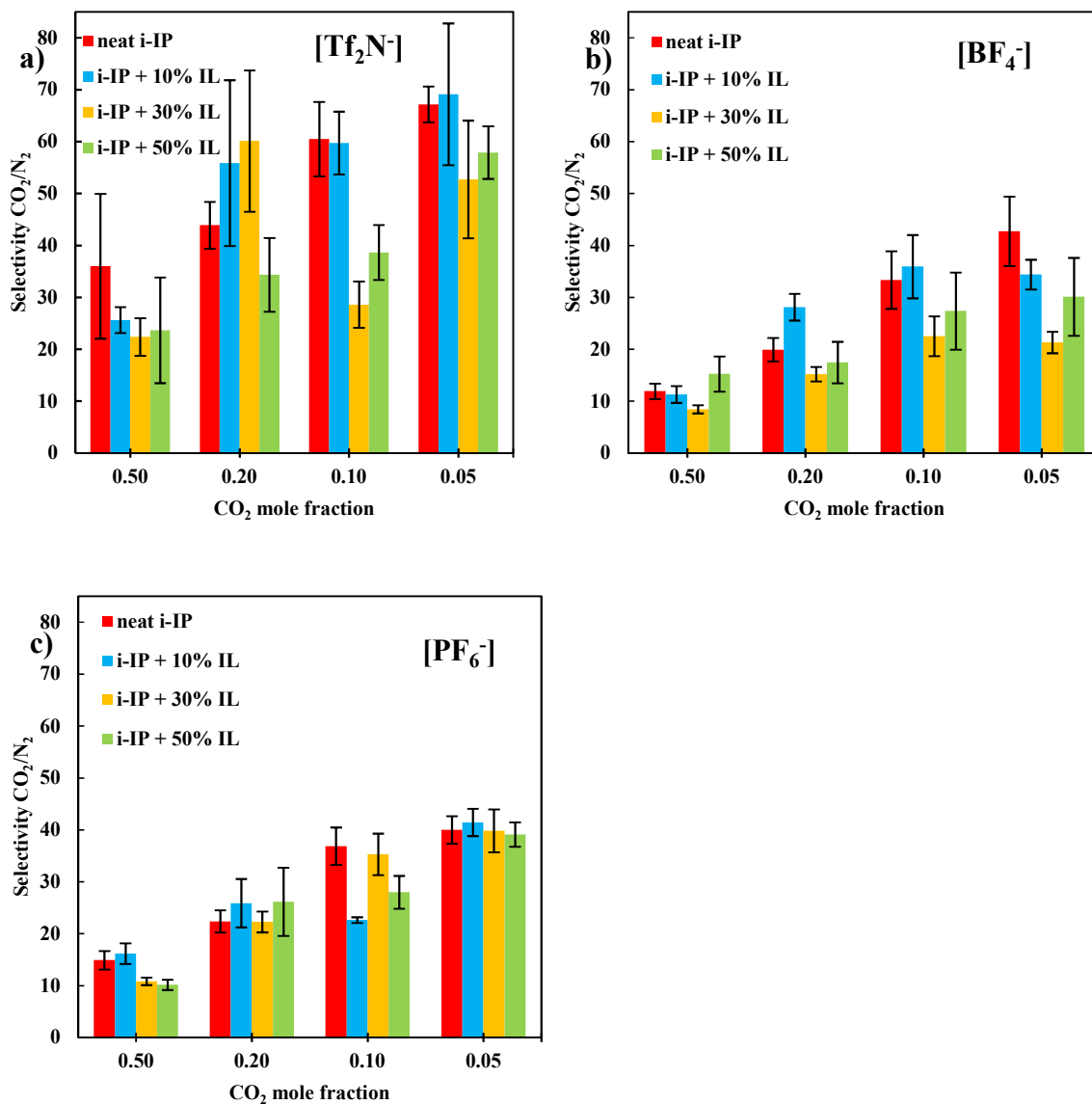


Figure 4.4. Predicted CO₂/N₂ selectivity for: a) [Tf₂N⁻], b) [BF₄⁻], and c) [PF₆⁻] at 294 K and 1 bar.

4.3.3 Structural Analysis

A series of structural analyses were used to examine the different i-PI + IL composite compositions and different IL concentrations, in order to establish clearer correlations with the predicted gas solubility. The resulting structure after CO₂ saturation was printed using a 3D printing tool and presented in **Figure C4.13**. As **Figure 4.5** shows, the pore size distributions

demonstrate the high probability of small pores in all systems (radii generally $< 1.5 \text{ \AA}$). However, the $[\text{PF}_6^-]$ -based materials are consistently found to have a slight shift from the smaller pore sizes to the higher end of the size spectrum ($> 1.5 \text{ \AA}$ nm). In tandem, **Figure 4.6a** shows that the $[\text{PF}_6^-]$ -based structures also have an elevated surface area, in comparison to other anion-based structures. These structural features (e.g., a higher probability of larger pores and a larger surface area) allow for increased gas adsorption. When comparing all of the different i-PI systems and i-PI + IL composites (**Figure 4.6**), we find that gas solubility is strongly correlated with the theoretical surface area of these materials: $[\text{PF}_6^-] > [\text{BF}_4^-] > [\text{Tf}_2\text{N}^-]$. The surface areas of all composite i-IP + IL structures are less than those of the neat i-IP structures, and this trend mimics the solubility results.

The impact of detailed structural features on the solubility and selectivity of other polymeric materials has been evaluated in some previous computational studies.^{68,69} For instance, Wood, et al. previously performed two separate simulation studies on the uptake of both CH_4 ⁷⁰ and H_2 ⁷¹ in hypercrosslinked organic polymers and compared results with experimental data. The simulated adsorption data, in agreement with experiment, was shown to strongly correlate with the surface area of the material. The two main factors that were determined to govern adsorption in these materials were the micropore volume and surface area. Also, a high correlation between surface area and permeability of PIMs has been previously reported by Madkour and Mark.⁶⁸

Surprisingly, the FFV values in our study do not provide a consistent indication of gas solubility for i-IPs, while it has shown to be a sufficient indicator for permeability in previous studies of PIMs.^{68,72} As **Figure 4.6b** shows, the FFV very slightly increases with respect to the IL addition, but this trend is not mimicked by the solubility. For instance, the $[\text{Tf}_2\text{N}^-]$ -based

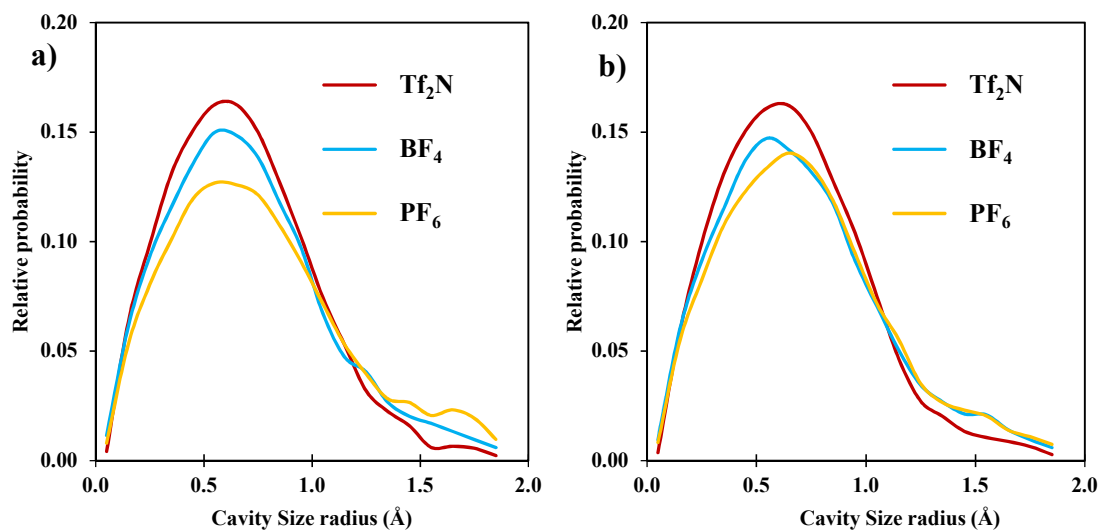
structures show the highest FFV, and the $[\text{BF}_4^-]$ -based structures show the lowest FFV (similar to the density trend in Table 2). However, the $[\text{BF}_4^-]$ -based structures are predicted to have higher gas solubility. In addition, while the $[\text{BF}_4^-]$ -based structures have a lower density than the $[\text{PF}_6^-]$ -based structures, the gas solubility of $[\text{PF}_6^-]$ -based structures is higher. As a result, the density and FFV are not found to correlate well with gas solubility in the present study. While these metrics may be useful for identifying larger differences in other systems, we find that they are not able to adequately capture the subtle structural features and of our i-PI and i-PI + IL systems.

Figure 4.7 shows the structural changes (surface area and FFV) before and after performing the MD/GCMC cycles, in order to map the simultaneous evolution of these system properties. Positive changes in the surface area between the initial and final structures show that adsorbed CO_2 imparts increases in the surface area, (while the density is constant throughout all of the MD/GCMC cycles). The small increases in the surface area ($\sim 1\text{-}4\%$) correlate with large impacts on the CO_2 solubility (by up to 200%), as shown in **Figure 4.7b**. However, the FFV does not show significant changes. In fact, the FFV decreases in half of the cases, indicating a clear inconsistency with respect to the CO_2 solubility.

The accessible surface area calculation is strongly dependent upon the probe size used, and this can potentially be a major factor in our analysis and comparison. In particular, we are working with three different gases (CO_2 , N_2 , and CH_4 with kinetic diameters of 3.30, 3.64, 3.80 Å, respectively).⁷³⁻⁷⁵ To explore this issue, a range of different probe sizes were tested in the surface area calculation, with the resulting surface areas shown in **Figure 4.8** (a default value of 4.0 Å was used in **Figure 4.6**). Regardless of the probe size used, the $[\text{PF}_6^-]$ -based structures show the highest surface area, and the $[\text{Tf}_2\text{N}^-]$ -based structures show the lowest. Using a probe diameter of 1.0 Å, the calculated surface area of the composite structures is higher than that of

the neat polymer. Also when using this small probe size, the surface area is predicted to increase as the concentration of the IL increases (in contrast to the trend predicted with the larger probes). However, a probe diameter of 1.0 Å is able to explore large regions of the material that are likely inaccessible and irrelevant to our adsorbates.

Another interesting result is the surface area of the i-PI + 10% IL in $[\text{Tf}_2\text{N}]^-$ -based and $[\text{BF}_4]^-$ -based systems, as there is a large probe-size dependency. As **Figures 4.8c** and **4.8d** show, with a probe size larger than 3.0 Å, the surface area of the i-PI + 10% IL composite is larger than the neat i-PI. With a probe diameter of 2.0 Å, the surface areas of the neat and composite (10% IL) structures are almost overlapping. However, as the probe size grows from 3.0 to 4.0 Å, the gap between neat and composite (10% IL) increases in favor of the composite structure. This surface area analysis indicates that the composite structures have a higher probability of smaller pore sizes, and this further corroborates the PSD analysis in **Figure 4.5**.



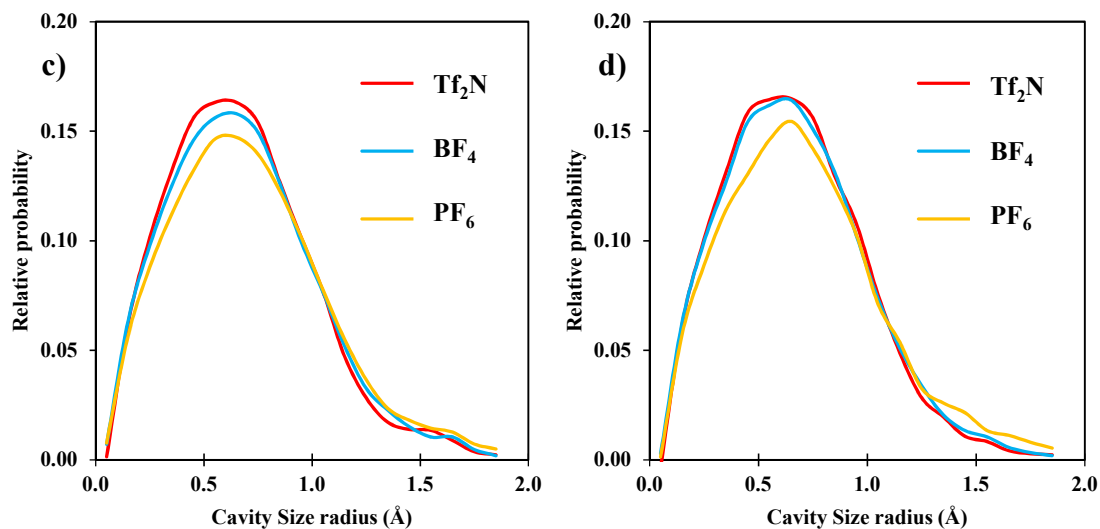


Figure 4.5. Pore size distribution for: a) neat i-IP, b) composite structure of i-IP + 10% IL, c) i-IP + 30% IL, and d) i-IP + 50% IL at 294 K and 1 bar (specifically, sample #2 of Table 2 after CO₂ saturation).

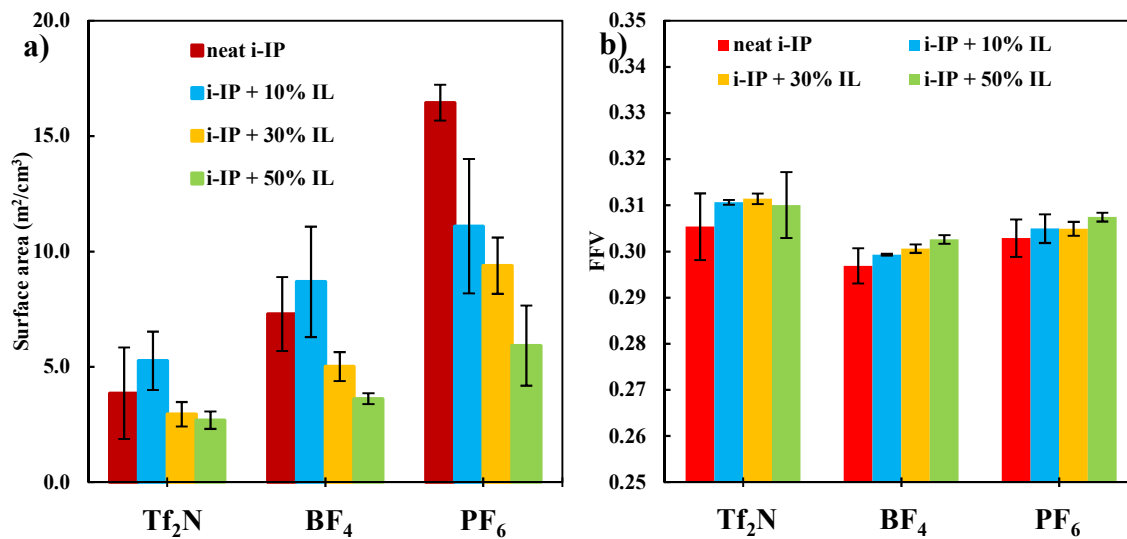


Figure 4.6. Comparison of: a) the surface area and b) the FFV at 294 K and 1 bar for CO₂ saturated structures.

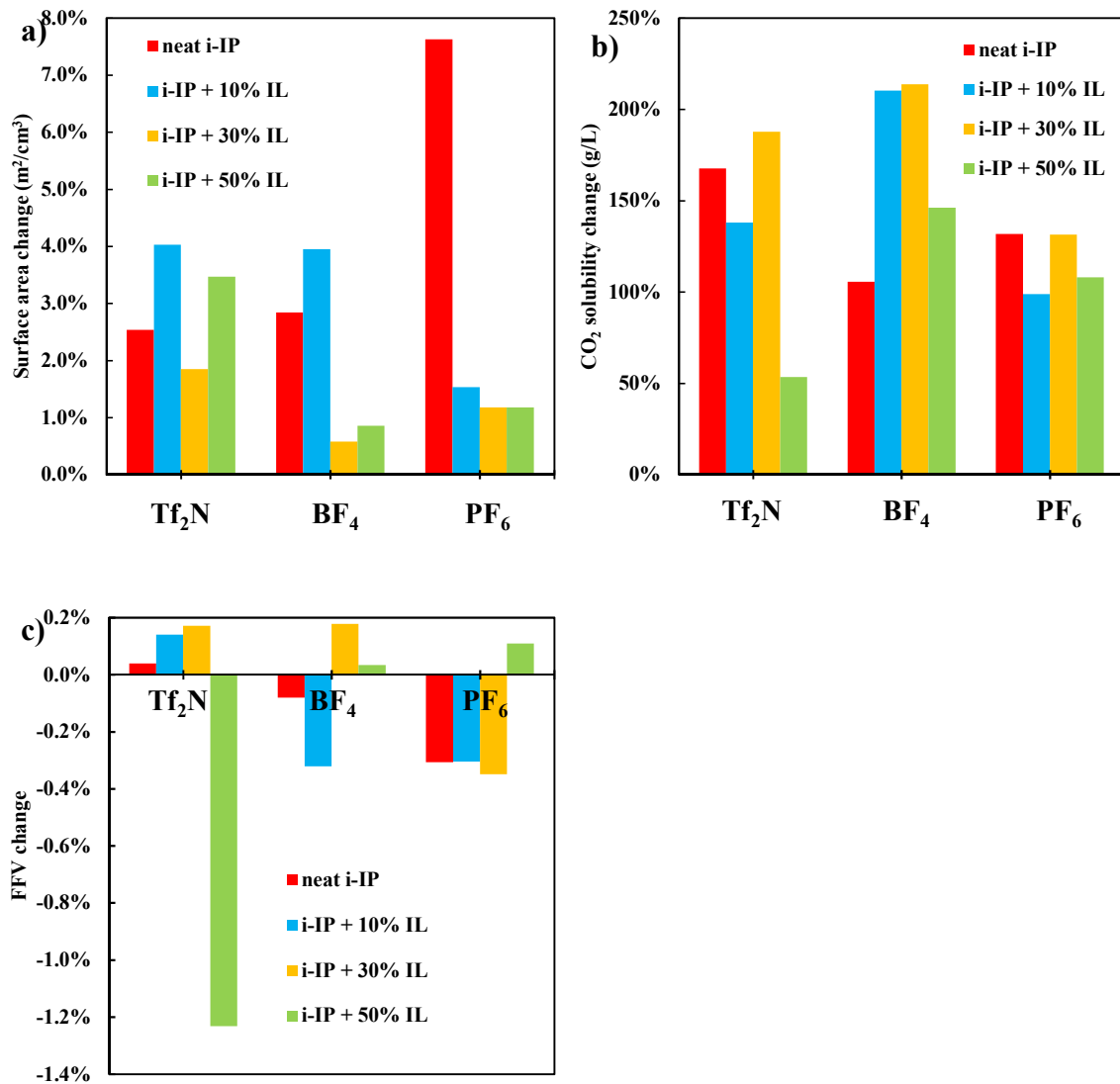


Figure 4.7. Comparison of the average: a) surface area, b) solubility, and c) FFV change before and after the MD/GCMC cycles involving CO₂ adsorption.

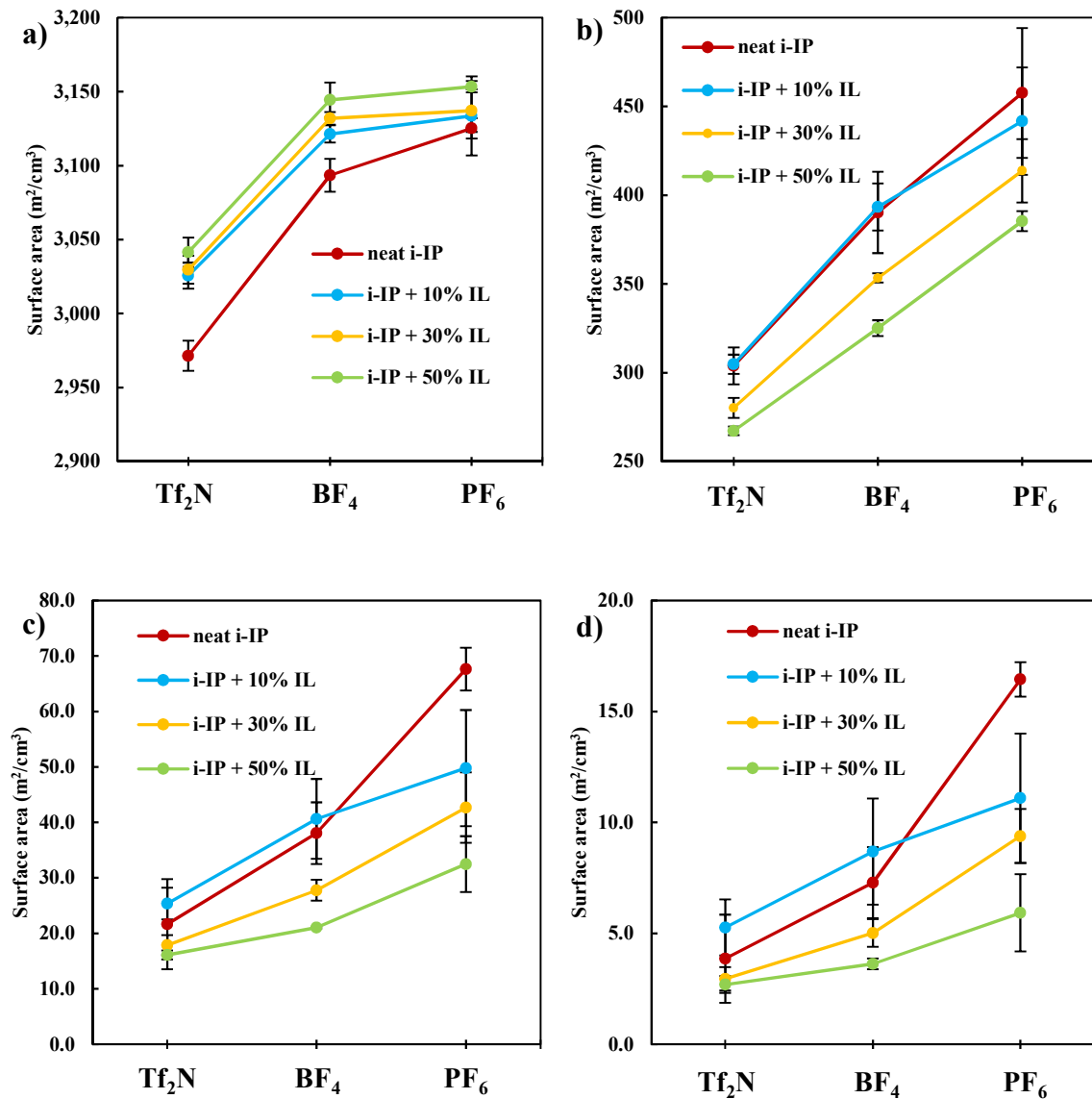
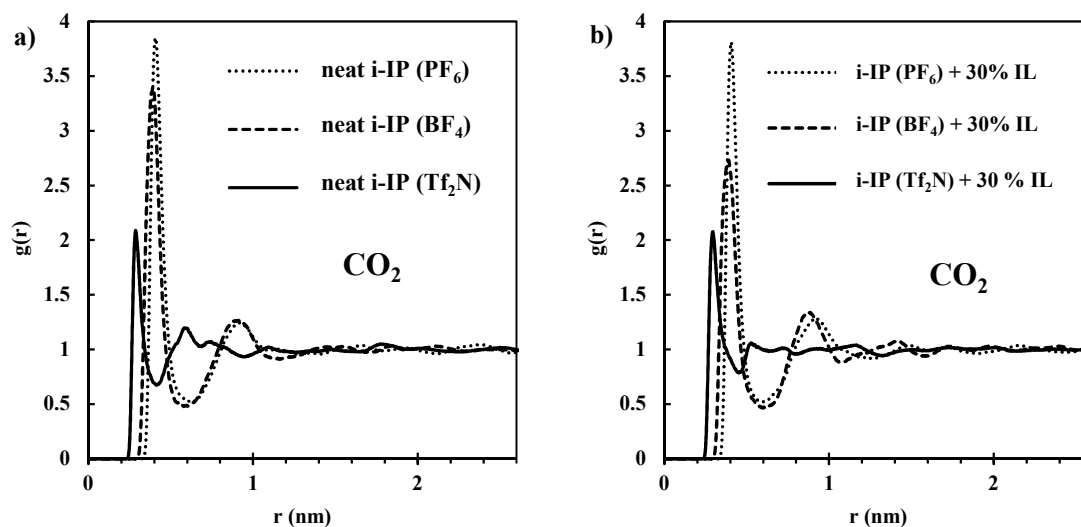


Figure 4.8. Probe diameter size sensitivity analysis for the CO₂ saturated structures: a) 1.0 Å, b) 2.0 Å, c) 3.0 Å, and d) 4.0 Å.

4.3.4 Adsorbate/Adsorbent Interaction Analysis

To identify the dominant molecular-level interactions involved with the gas adsorption, radial distribution functions were calculated for key sites in our i-IP and i-IP+IL systems. In general, the RDF represents the average of three samples from 10 ns of NVT MD simulation at

294 K. The carbon atoms of CO₂ and CH₄ molecules and the nitrogen atoms of N₂ gas molecules were chosen to represent the molecular adsorbate interactions with different sites of the adsorbents. With respect to the different anions, the boron (B) atoms in [BF₄⁻], the phosphorus (P) atoms in [PF₆⁻], and the oxygen (O) atoms in [Tf₂N⁻] molecules were selected to represent the anions in the RDF calculation since CO₂ molecules show a strong interaction with the oxygen sites of the [Tf₂N⁻]. The different nitrogen sites of the monomer are identified in **Figure 4.1**. The N1 and N2 nitrogen on the monomer represent the ligand sites of the polymer and N3 to N6 were identified as imidazolium ring nitrogen atoms in the polymer structure.



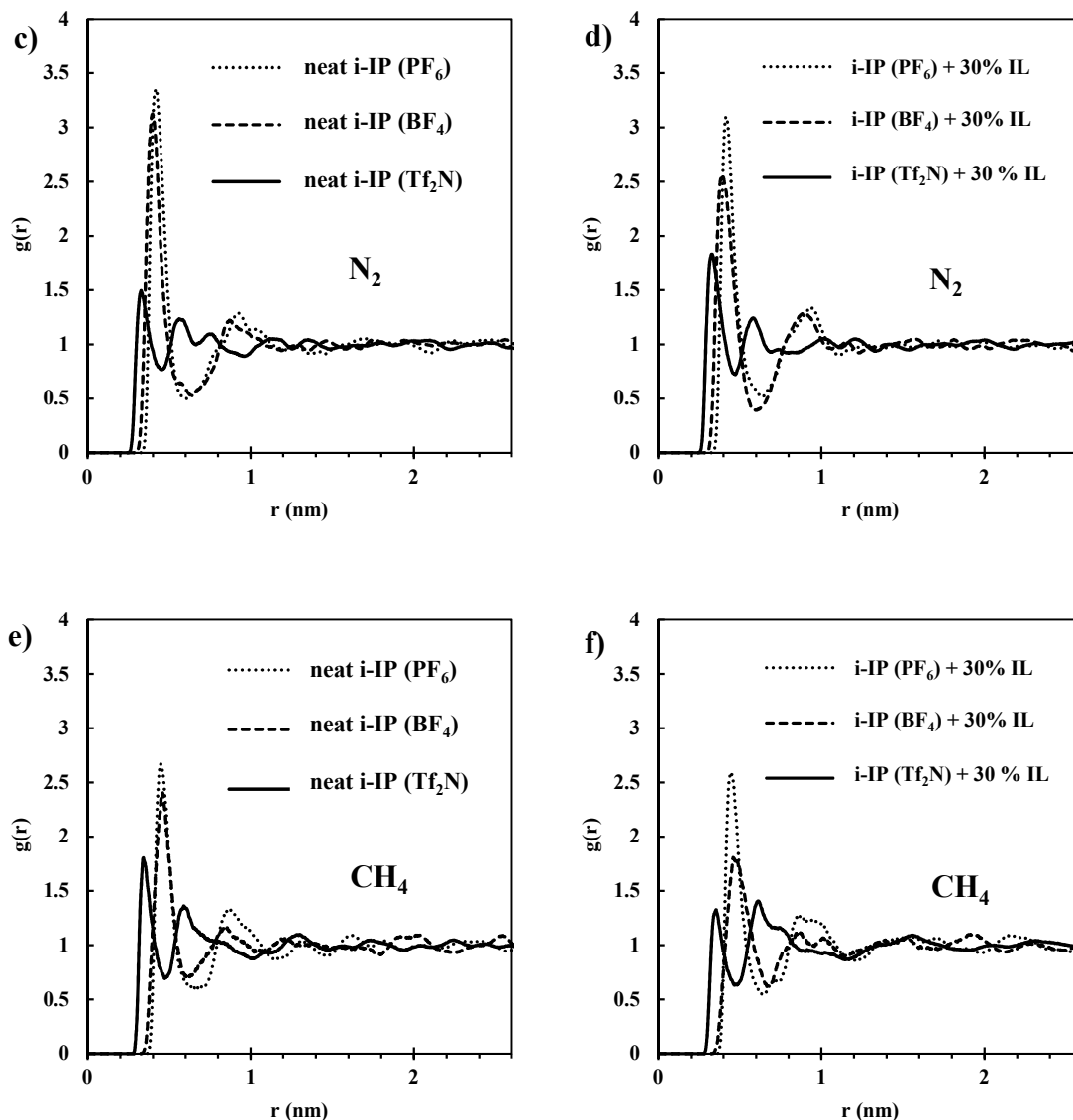


Figure 4.9. Radial distribution functions of gas interactions with different anion species: a and b) carbon site of CO₂; c and d) nitrogen sites of N₂ ; e and f) carbon site of CH₄.

Figure 4.9 represents the adsorbed gas interactions with different anions. In general, the interaction intensity (height of the first peak in the RDF) of different anions with the adsorbed gases shows the following trend: $[\text{PF}_6^-] > [\text{BF}_4^-] > [\text{Tf}_2\text{N}^-]$. The strongest gas interaction was observed with the $[\text{PF}_6^-]$ anions, and this is consistent, regardless of the different gas types and

different IL concentrations within the polymer + IL composites. With respect to the different gas species, the height of the first RDF peak follows the trend: $\text{CO}_2 > \text{N}_2 > \text{CH}_4$ in almost all concentrations of polymer + IL.

The interaction of the adsorbed CO_2 with $[\text{Tf}_2\text{N}^-]$ and $[\text{PF}_6^-]$ remains constant in the neat i-PI structure and in the i-PI + IL composites (**Figures C4.14 to C4.16**). The interaction of CO_2 with $[\text{BF}_4^-]$ is reduced in the i-PI + 10% and i-PI + 30% IL, while the interactions increases back to the original value in the i-PI + 50% IL.

The N_2 molecules show very similar behavior to the CO_2 molecules, with respect to their interaction with the anions. Adding IL to the i-IP does not significantly change the N_2 gas molecule interactions within the $[\text{Tf}_2\text{N}^-]$ and $[\text{PF}_6^-]$ -based structures. However, the N_2 gas molecules within the $[\text{BF}_4^-]$ -based structures show a weakened interaction with the $[\text{BF}_4^-]$ anions from the addition of 10% and 30 % IL. In the polymer + 50% IL samples, the interaction rises back to the value observed in the neat i-PI.

The interactions of CH_4 with the anions are characteristically different from those of the CO_2 and N_2 gas molecules. In the $[\text{Tf}_2\text{N}^-]$ and $[\text{BF}_4^-]$ -based structures, the CH_4 interaction with the anions decreases with the addition of the IL. In the i-IP + 50% IL in $[\text{BF}_4^-]$ -based structures, the CH_4 and anion interaction returns to the value found within the neat polymer. In the $[\text{PF}_6^-]$ -based structures, the CH_4 interaction with the anions remains constant, despite IL addition to the polymer.

While the changes in adsorption and site-site specificity are moderate, these details provide fundamental insight into further tuning the gas selectivity of mixed i-PI + IL composite systems. While other site-site interactions were investigated (such as different sites of i-IP backbone and

[C₄mim⁺] species), our primary focus of this investigation and the largest changes are found to be associated with the anions.

4.4 Conclusion

In this study, the gas selectivity of different combinations of anions in a composite i-IP + IL materials are evaluated, the performance is analyzed with respect to detailed structural changes and specific molecular interactions. The positive charge of the monomer backbone is compensated by pairing with different anions ([PF₆⁻], [BF₄⁻], and [Tf₂N⁻]) to yield a charge neutral i-IP structure. Additionally, different composite structures of the i-PI + of IL ([C₄mim⁺] with [PF₆⁻], [BF₄⁻], and [Tf₂N⁻]) were investigated to evaluate the effect of the IL on gas solubility and selectivity for each structure.

While [PF₆⁻]-based structures (neat i-PI and i-PI + IL composites) showed the highest CO₂ solubility, [BF₄⁻]-based structures showed the highest selectivity for CO₂ from the CO₂/CH₄ mixture. Comparing the initial and equilibrated structures of the prepared samples reveals that the CO₂ adsorption leads to notable changes in the structure. A high surface area as well as a high probability of larger pore sizes increases the gas solubility, while adding IL to the neat polymer system reduces the surface area and decreases the gas solubility, and this is consistent with experiments. The surface area follows the same trend for three different anion based structures: [PF₆⁻] > [BF₄⁻] > [Tf₂N⁻]. The composite structure of neat i-IP + IL also switches the adsorption sites in the polymer structure for the CO₂/CH₄ gas mixture from ligand to imidazolium sites.

In our previous work,⁴⁴ pure CH₄ displays a stronger interaction with the neat [Tf₂N⁻]-based i-PI in comparison to the CO₂ gas. However, upon adding IL, the CH₄-anion interaction showed a sharp decrease in the i-IP + IL composite structure. This current study supports the

previous work and explains the competitive occupation and interaction between mixed gas adsorption. The CO₂ has a stronger interaction with the anion in all of the neat i-PI and i-PI + IL composites. Although the [PF₆⁻]-based structure has higher gas solubility (due to larger pores and surface area), the selectivity remains a challenging issue. Experimental investigations are currently underway to corroborate the trends found in the current study, in addition to other IL additives that may further increase the capacity and selectivity for CO₂ separation applications.

Acknowledgements

Support for this work was provided by the National Science Foundation (CBET-1605411) and computer resources were provided by the Alabama Supercomputer Center.

Supporting Information

The Supporting Information is available in Appendix C. It includes MD/GCMC cycles of the CO₂ solubility, 3D printed structure, CO₂ solubility capacity comparison with other polymers and porous materials, RDF calculation of anion and adsorbed gas (CO₂, CH₄, and N₂) interactions for all concentrations of i-IP + IL composite structures.

Appendix C, Supporting Information for Chapter 4.

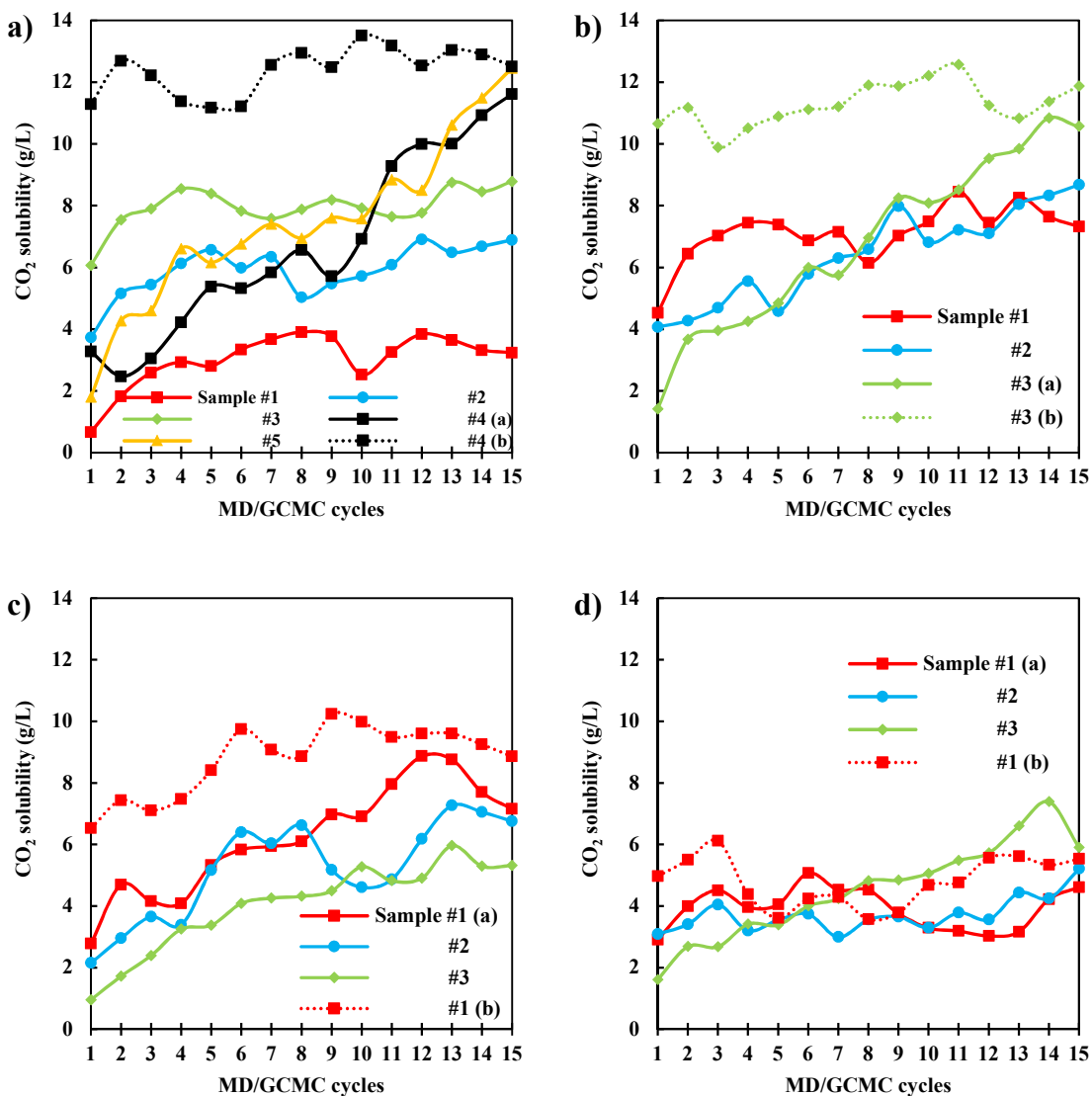


Figure C4.10. CO₂ solubility calculation at 294 K and 1 bar for [Tf₂N⁻]-based structure. a) neat polymer, b) polymer + 10% IL composite, c) polymer + 30% IL composite, and d) polymer + 50% IL composite. Dashed line represents the second 15 set of MD/GCMC cycles.

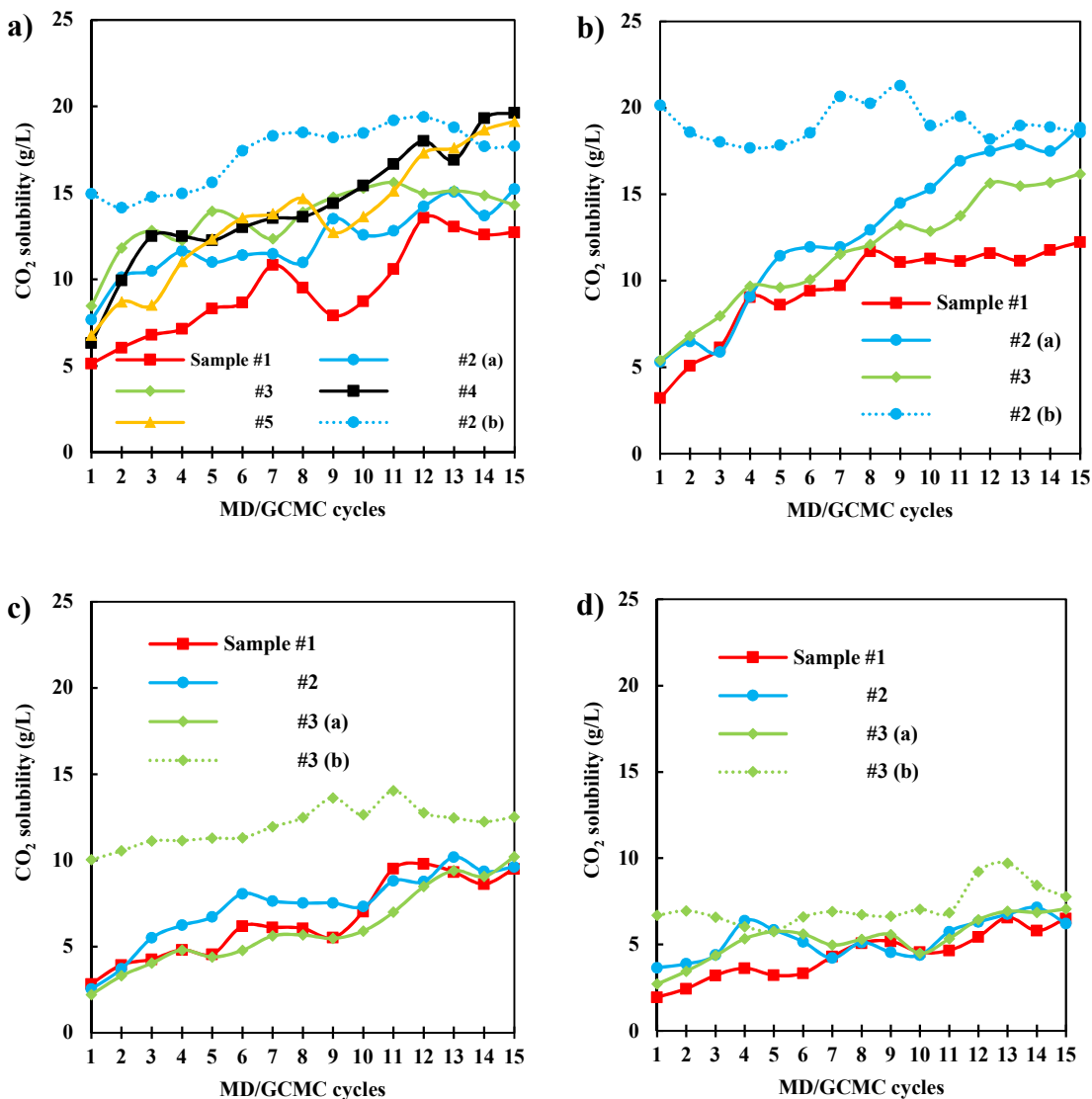


Figure C4.11. CO₂ solubility calculation at 294 K and 1 bar for [BF₄⁻]-based structure. a) neat polymer, b) polymer + 10% IL composite, c) polymer + 30% IL composite, and d) polymer + 50% IL composite. Dashed line represents the second 15 set of MD/GCMC cycles.

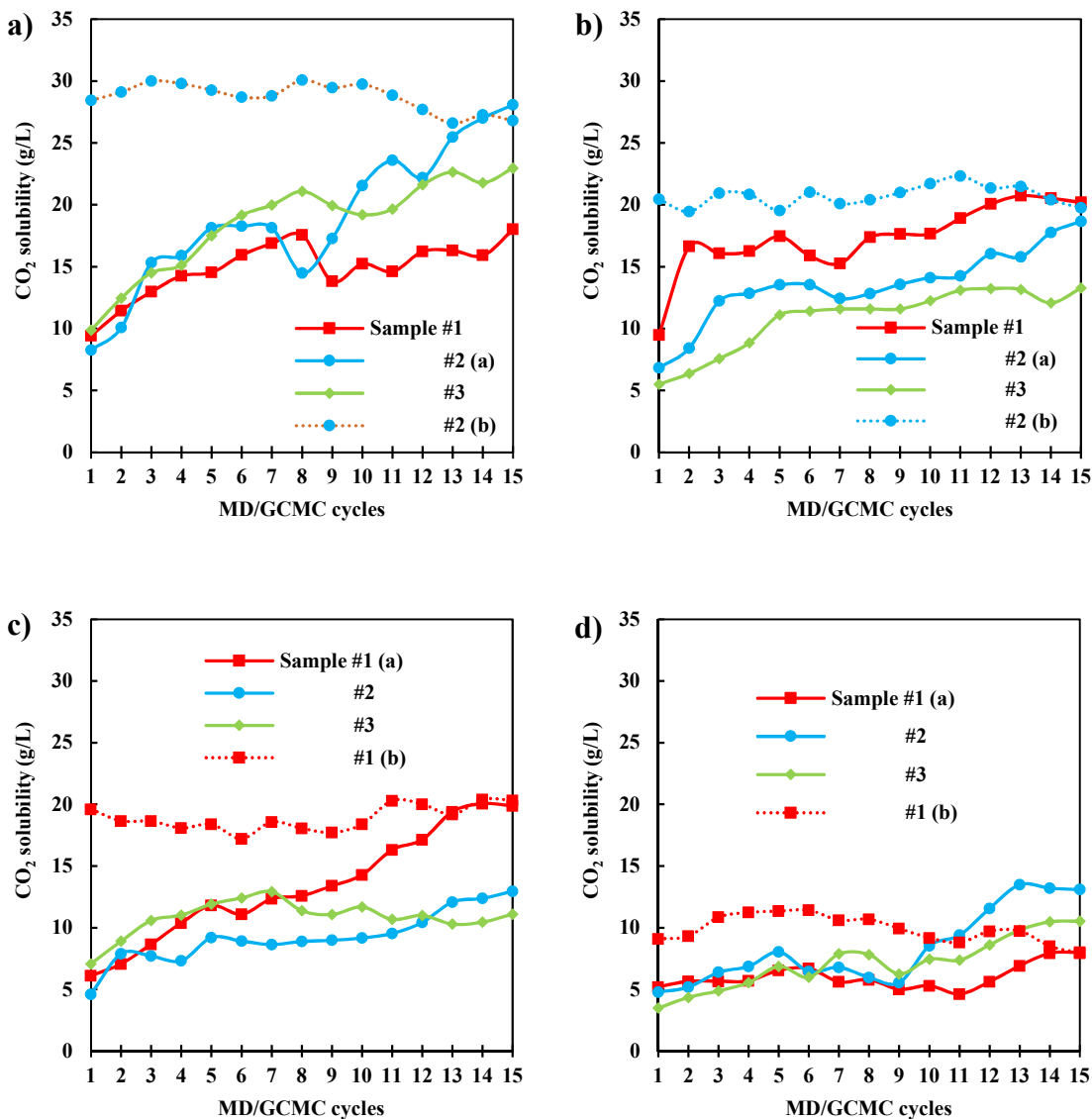


Figure C4.12. CO₂ solubility calculation at 294 K and 1 bar for [PF₆]⁻-based structure. a) neat polymer, b) polymer + 10% IL composite, c) polymer + 30% IL composite, and d) polymer + 50% IL composite. Dashed line represents the second 15 set of MD/GCMC cycles.

The 3D printed structure represents the polymer chain and created porous area in our prepared model. The files are uploaded at <https://makerware.thingiverse.com/thing:2854795> and accessible for everyone free of charge. The prepared polymer model after relaxation was used to

calculate the pore size distribution. During the PSD calculation, the void spaces between the polymer molecules were occupied with imaginary particles. These artificial particles are merged together to create a smooth surface representing void space. The resulting structure was used to prepare the 3D structure representing the void space in the polymer as shown in **Figure C4.13**.

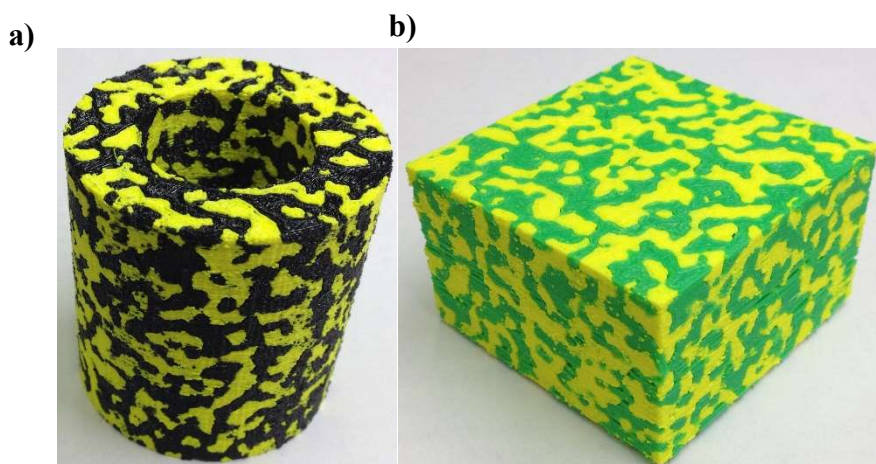


Figure C4.13. 3D printed structure of the polymer in a) cylindrical and b) cube shape to better illustrate the polymer molecules chain and crated porous area.

Table C4.3 Solubility (g/L) and selectivity for more comparison.

Material	Solubility (g/L)	Selectivity	
		CO ₂ /CH ₄	CO ₂ /N ₂
[C ₄ mim][Tf ₂ N] (Bulk IL)	4.70 ⁷⁶	~7.5 (100bar), 59(30bar) ^{8,77}	
[C ₄ mim][BF ₄] (Bulk IL)	4.24 ⁷⁶		
[C ₄ mim][PF ₆] (Bulk IL) (313 K)	3.54 ⁷⁶		
i-IP (exp.)	4.22 ⁴²	14.1	65.2
i-IP + 50% IL (exp.)	3.95 ⁴²	13.1	80.4
[C ₄ mim][Tf ₂ N]-based i-IP (neat) (sim.)	10.78	38.5 ± 5.7	36.0 ± 14.0
[C ₄ mim][BF ₄]-based i-IP (neat) (sim.)	18.09	148.0 ± 26.8	11.9 ± 1.5
[C ₄ mim][PF ₆]-based i-IP (neat) (sim.)	26.87	52.8 ± 4.3	14.9 ± 1.8
PIM-1 (308 K)	2.46 ³⁷		
PIM-EA-TB	92.15 ⁷⁸		
PIL NTf ₂ -60 IL Si NTf ₂	4.42 ⁷⁹		
[C ₈ mim][Tf ₂ N]	4.18 ⁸⁰	9	24.9
[C ₈ H ₄ F ₁₃ mim][NTf ₂]	4.36 ⁸⁰	13	18.7

Table C4.4 Solubility (mg/g) and selectivity for more comparison.

Material	Solubility (mg/g)	Selectivity	
		CO ₂ /CH ₄	CO ₂ /N ₂
i-IP (exp.)	2.54	14.1	65.2
i-IP + 50% IL (exp.)	2.26	13.1	80.4
[C ₄ mim][Tf ₂ N]-based i-IP (neat) (sim.)	6.69	38.5 ± 5.7	36.0 ± 14.0
[C ₄ mim][BF ₄]-based i-IP (neat) (sim.)	13.18	148.0 ± 26.8	11.9 ± 1.5
[C ₄ mim][PF ₆]-based i-IP (neat) (sim.)	18.17	52.8 ± 4.3	14.9 ± 1.8
ZIF-8	19.65 ⁸¹	~3	~8
CuBTC	98.24 ¹⁰	~5.5	~16
TSP-2	110.03 ⁴³		
Tr-NPI	52.81 ⁴³		
soPIM-1 (293 K)	110.03 ^{82,83}	~23.8	~24
VICDOC	176.04 ⁸⁴		
COF-5	110.03 ⁵	~3	
IRMOF-1 + [Bmim] [SCN] (300 K)	15.84 ⁸⁵		~35

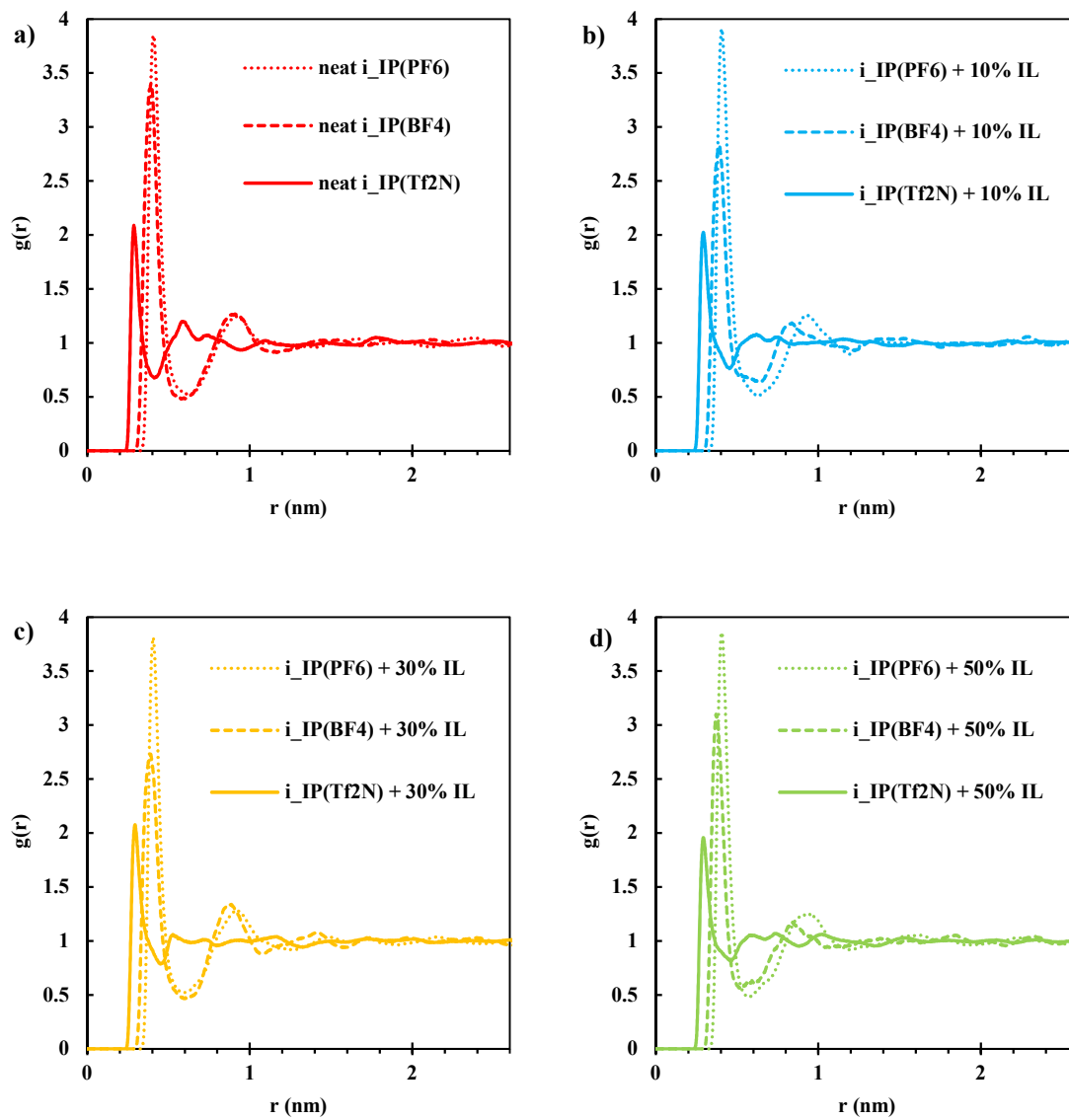


Figure C4.14. Carbon site of CO_2 interaction with anions. (B in BF_4 , P in PF_6 and O in Tf_2N).

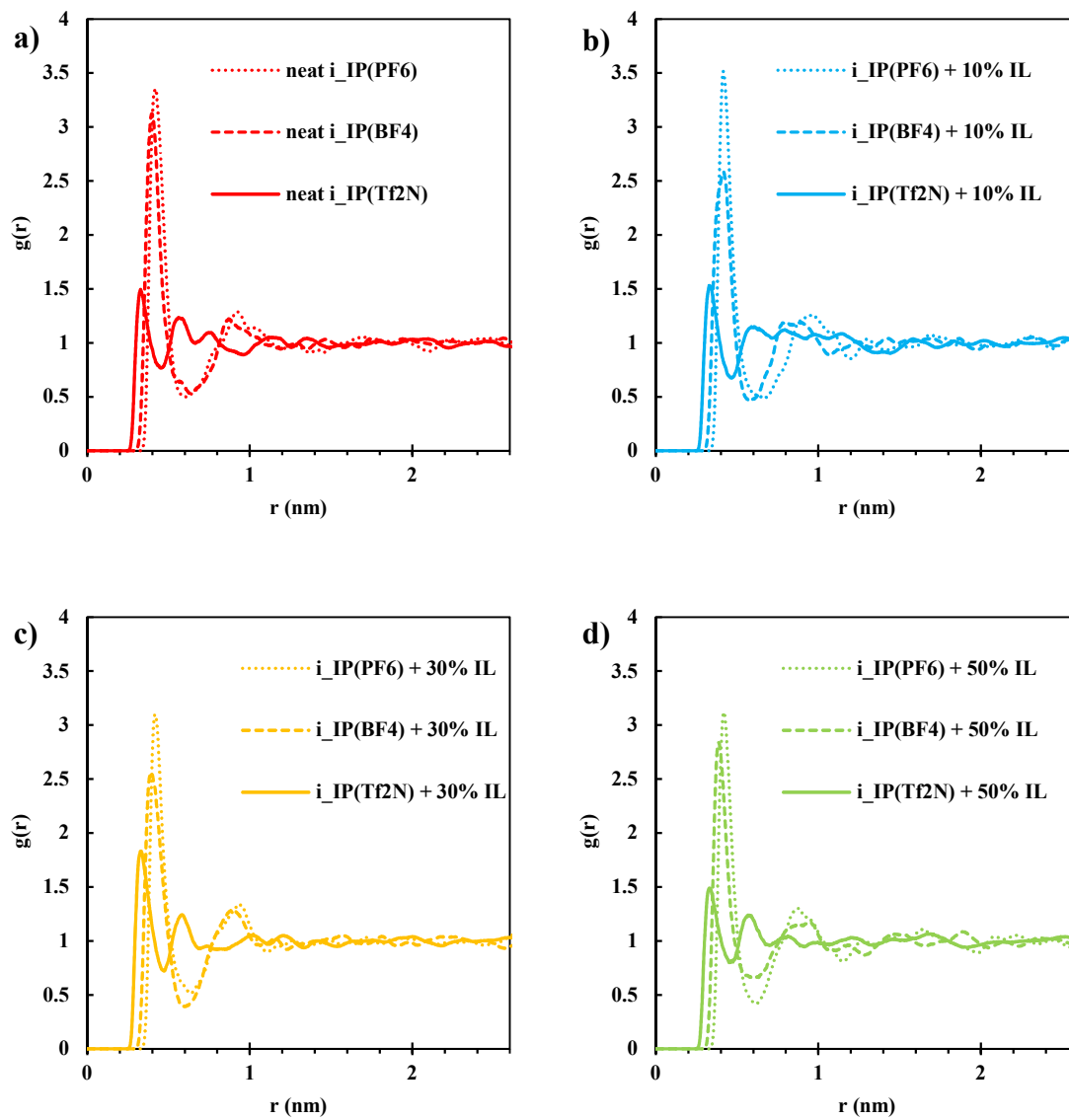


Figure C4.15. Nitrogen site of N_2 gas interactions with anions. (B in BF_4 , P in PF_6 and O in Tf_2N).

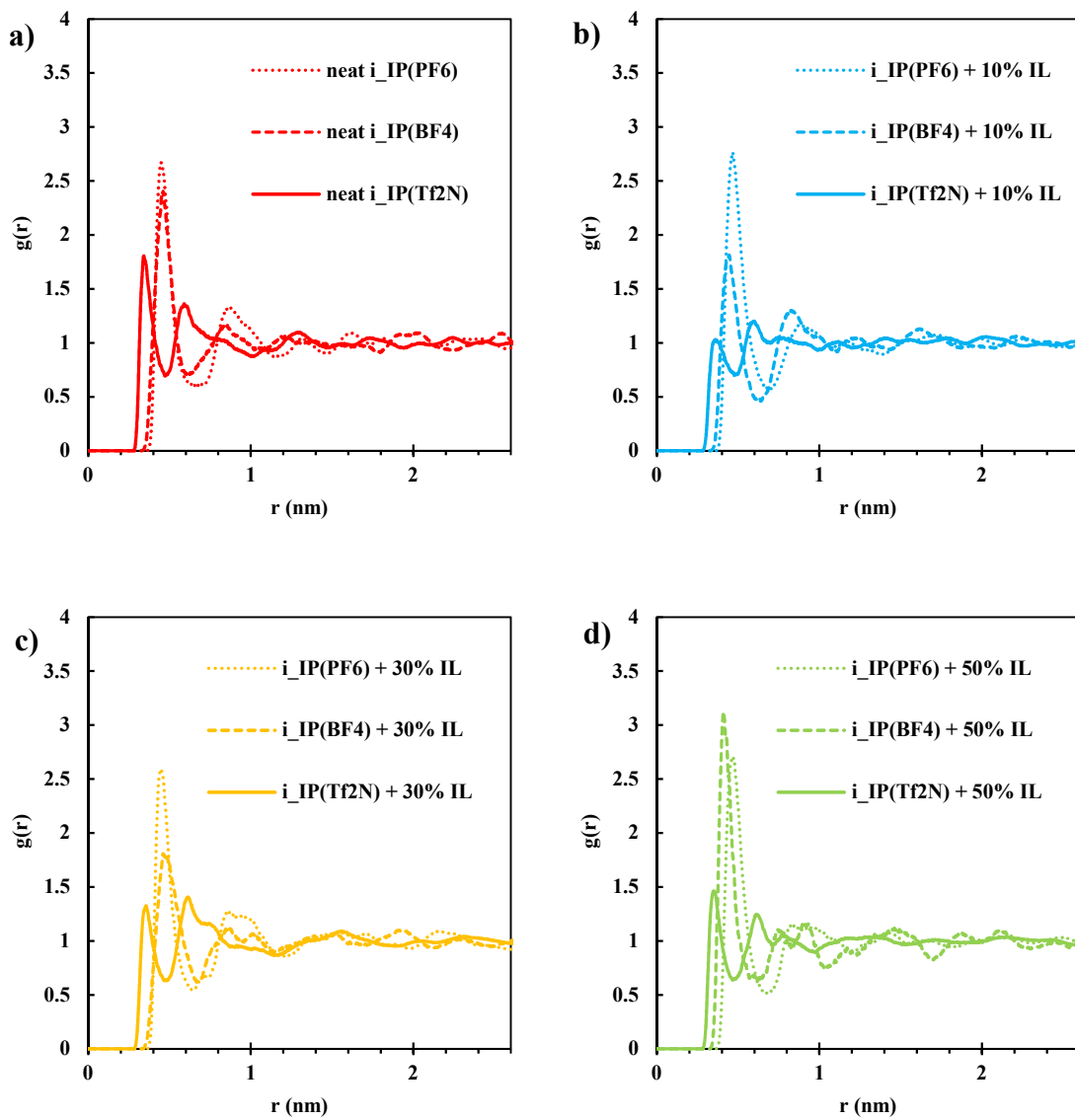


Figure C4.16. Carbon site of CH_4 in interaction with anions. (B in BF_4 , P in PF_6 and O in Tf_2N).

References

- (1) Martín, C. F.; Stöckel, E.; Clowes, R.; Adams, D. J.; Cooper, A. I.; Pis, J. J.; Rubiera, F.; Pevida, C. Hypercrosslinked organic polymer networks as potential adsorbents for pre-combustion CO₂ capture. *J. Mater. Chem.* **2011**, *21*, 5475-5483.
- (2) Abdul Halim, H. N.; M. Shariff, A.; Tan, L. S.; Bustam, M. A. Mass Transfer Performance of CO₂ Absorption from Natural Gas using Monoethanolamine (MEA) in High Pressure Operations. *Ind. Eng. Chem. Res.* **2015**, *54*, 1675-1680.
- (3) To, J. W.; He, J.; Mei, J.; Haghpanah, R.; Chen, Z.; Kurosawa, T.; Chen, S.; Bae, W. G.; Pan, L.; Tok, J. B.; Wilcox, J.; Bao, Z. Hierarchical N-Doped Carbon as CO₂ Adsorbent with High CO₂ Selectivity from Rationally Designed Polypyrrole Precursor. *J. Am. Chem. Soc.* **2016**, *138*, 1001-1009.
- (4) Delgado, J. A.; Águeda, V. I.; Uguina, M. A.; Sotelo, J. L.; Brea, P.; Grande, C. A. Adsorption and Diffusion of H₂, CO, CH₄, and CO₂ in BPL Activated Carbon and 13X Zeolite: Evaluation of Performance in Pressure Swing Adsorption Hydrogen Purification by Simulation. *Ind. Eng. Chem. Res.* **2014**, *53*, 15414-15426.
- (5) Vicent-Luna, J. M.; Luna-Triguero, A.; Calero, S. Storage and Separation of Carbon Dioxide and Methane in Hydrated Covalent Organic Frameworks. *J. Phys. Chem. C* **2016**, *120*, 23756-23762.
- (6) Xiang, Z.; Mercado, R.; Huck, J. M.; Wang, H.; Guo, Z.; Wang, W.; Cao, D.; Haranczyk, M.; Smit, B. Systematic Tuning and Multifunctionalization of Covalent Organic Polymers for Enhanced Carbon Capture. *J. Am. Chem. Soc.* **2015**, *137*, 13301-13307.
- (7) Zeng, S.; Zhang, X.; Bai, L.; Zhang, X.; Wang, H.; Wang, J.; Bao, D.; Li, M.; Liu, X.; Zhang, S. Ionic-Liquid-Based CO₂ Capture Systems: Structure, Interaction and Process. *Chem. Rev.* **2017**, *117*, 9625-9673.
- (8) Budhathoki, S.; Shah, J. K.; Maginn, E. J. Molecular Simulation Study of the Performance of Supported Ionic Liquid Phase Materials for the Separation of Carbon Dioxide from Methane and Hydrogen. *Ind. Eng. Chem. Res.* **2017**, *56*, 6775-6784.
- (9) Cadena, C.; Anthony, J. L.; Shah, J. K.; Morrow, T. I.; Brennecke, J. F.; Maginn, E. J. Why is CO₂ so soluble in imidazolium-based ionic liquids? *J. Am. Chem. Soc.* **2004**, *126*, 5300-5308.
- (10) Sezginel, K. B.; Keskin, S.; Uzun, A. Tuning the Gas Separation Performance of CuBTC by Ionic Liquid Incorporation. *Langmuir* **2016**, *32*, 1139-1147.
- (11) Li, Z.; Xiao, Y.; Xue, W.; Yang, Q.; Zhong, C. Ionic Liquid/Metal–Organic Framework Composites for H₂S Removal from Natural Gas: A Computational Exploration. *J. Phys. Chem. C* **2015**, *119*, 3674-3683.
- (12) Harris, K. R.; Kanakubo, M. Self-diffusion, velocity cross-correlation, distinct diffusion and resistance coefficients of the ionic liquid [BMIM][Tf₂N] at high pressure. *Phys. Chem. Chem. Phys.* **2015**, *17*, 23977-23993.
- (13) Kinik, F. P.; Altintas, C.; Balci, V.; Koyuturk, B.; Uzun, A.; Keskin, S. [BMIM][PF₆] Incorporation Doubles CO₂ Selectivity of ZIF-8: Elucidation of Interactions and Their Consequences on Performance. *ACS Appl. Mater. Inter.* **2016**, *8*, 30992-31005.
- (14) Wu, N.; Ji, X.; Xie, W.; Liu, C.; Feng, X.; Lu, X. Confinement Phenomenon Effect on the CO₂ Absorption Working Capacity in Ionic Liquids Immobilized into Porous Solid Supports. *Langmuir* **2017**, *33*, 11719-11726.

- (15) Xue, W.; Li, Z.; Huang, H.; Yang, Q.; Liu, D.; Xu, Q.; Zhong, C. Effects of ionic liquid dispersion in metal-organic frameworks and covalent organic frameworks on CO₂ capture: A computational study. *Chem. Eng. Sci.* **2016**, *140*, 1-9.
- (16) Shi, W.; Luebke, D. R. Enhanced gas absorption in the ionic liquid 1-n-hexyl-3-methylimidazolium bis(trifluoromethylsulfonyl)amide ([hmim][Tf₂N]) confined in silica slit pores: a molecular simulation study. *Langmuir* **2013**, *29*, 5563-5572.
- (17) Vicent-Luna, J. M.; Gutiérrez-Sevillano, J. J.; Anta, J. A.; Calero, S. Effect of Room-Temperature Ionic Liquids on CO₂ Separation by a Cu-BTC Metal–Organic Framework. *J. Phys. Chem. C* **2013**, *117*, 20762-20768.
- (18) Kohler, F. T. U.; Popp, S.; Klefer, H.; Eckle, I.; Schrage, C.; Böhringer, B.; Roth, D.; Haumann, M.; Wasserscheid, P. Supported ionic liquid phase (SILP) materials for removal of hazardous gas compounds – efficient and irreversible NH₃ adsorption. *Green Chem.* **2014**, *16*, 3560-3568.
- (19) Abedini, A.; Ludwig, T.; Zhang, Z.; Turner, C. H. Molecular Dynamics Simulation of Bismuth Telluride Exfoliation Mechanisms in Different Ionic Liquid Solvents. *Langmuir* **2016**, *32*, 9982-9992.
- (20) Tang, Z.; Lu, L.; Dai, Z.; Xie, W.; Shi, L.; Lu, X. CO₂ Absorption in the Ionic Liquids Immobilized on Solid Surface by Molecular Dynamics Simulation. *Langmuir* **2017**, *33*, 11658-11669.
- (21) Shen, Y.; Hung, F. R. A Molecular Simulation Study of Carbon Dioxide Uptake by a Deep Eutectic Solvent Confined in Slit Nanopores. *J. Phys. Chem. C* **2017**, *121*, 24562-24575.
- (22) Zhang, K.; Kumar, S. K. Molecular Simulations of Solute Transport in Polymer Melts. *ACS Macro Lett.* **2017**, *6*, 864-868.
- (23) Wang, M.; Zhao, J.; Wang, X.; Liu, A.; Gleason, K. K. Recent progress on submicron gas-selective polymeric membranes. *J. Mater. Chem. A* **2017**, *5*, 8860-8886.
- (24) Tome, L. C.; Marrucho, I. M. Ionic liquid-based materials: a platform to design engineered CO₂ separation membranes. *Chem. Soc. Rev.* **2016**, *45*, 2785-2824.
- (25) Rukmani, S. J.; Liyana-Arachchi, T. P.; Hart, K. E.; Colina, C. M. Ionic-Functionalized Polymers of Intrinsic Microporosity for Gas Separation Applications. *Langmuir* **2018**, *34*, 3949-3960.
- (26) Sharma, P.; Chakrabarty, S.; Roy, S.; Kumar, R. Molecular View of CO₂ Capture by Polyethylenimine: Role of Structural and Dynamical Heterogeneity. *Langmuir* **2018**.
- (27) Ma, C.; Urban, J. J. Polymers of Intrinsic Microporosity (PIMs) Gas Separation Membranes: A mini Review. *Proceedings of the Nature Research Society* **2018**, *2*, 02002.
- (28) Saleh, M.; Lee, H. M.; Kemp, K. C.; Kim, K. S. Highly stable CO₂/N₂ and CO₂/CH₄ selectivity in hyper-cross-linked heterocyclic porous polymers. *ACS Appl. Mater. Inter.* **2014**, *6*, 7325-7333.
- (29) Wu, D.; Xu, F.; Sun, B.; Fu, R.; He, H.; Matyjaszewski, K. Design and preparation of porous polymers. *Chem. Rev.* **2012**, *112*, 3959-4015.
- (30) Meng, B.; Li, H.; Mahurin, Shannon M.; Liu, H.; Dai, S. Hyper-crosslinked cyclodextrin porous polymer: an efficient CO₂ capturing material with tunable porosity. *RSC Adv.* **2016**, *6*, 110307-110311.
- (31) Zhang, B.; Li, G.; Yan, J.; Wang, Z. Tetraphenyladamantane-Based Microporous Polybenzimidazoles for Adsorption of Carbon Dioxide, Hydrogen, and Organic Vapors. *J. Phys. Chem. C* **2015**, *119*, 13080-13087.
- (32) Fujii, K.; Ueki, T.; Hashimoto, K.; Kobayashi, Y.; Kitazawa, Y.; Hirose, K.; Matsugami, M.; Ohara, K.; Watanabe, M.; Shibayama, M. Microscopic Structure of Solvated Poly(benzyl methacrylate) in an Imidazolium-Based Ionic Liquid: High-Energy X-ray Total Scattering and All-Atom MD Simulation Study. *Macromolecules* **2017**, *50*, 4780-4786.

- (33) Ashourirad, B.; Sekizkardes, A. K.; Altarawneh, S.; El-Kaderi, H. M. Exceptional Gas Adsorption Properties by Nitrogen-Doped Porous Carbons Derived from Benzimidazole-Linked Polymers. *Chem. Mater.* **2015**, *27*, 1349-1358.
- (34) Errahali, M.; Gatti, G.; Tei, L.; Paul, G.; Rolla, G. A.; Canti, L.; Fraccarollo, A.; Cossi, M.; Comotti, A.; Sozzani, P.; Marchese, L. Microporous Hyper-Cross-Linked Aromatic Polymers Designed for Methane and Carbon Dioxide Adsorption. *J. Phys. Chem. C* **2014**, *118*, 28699-28710.
- (35) Ishiwari, F.; Takeuchi, N.; Sato, T.; Yamazaki, H.; Osuga, R.; Kondo, J. N.; Fukushima, T. Rigid-to-Flexible Conformational Transformation: An Efficient Route to Ring-Opening of a Tröger's Base-Containing Ladder Polymer. *ACS Macro Lett.* **2017**, *6*, 775-780.
- (36) Gouveia, A. S. L.; Tome, L. C.; Lozinskaya, E. I.; Shaplov, A. S.; Vygodskii, Y. S.; Marrucho, I. M. Exploring the effect of fluorinated anions on the CO₂/N₂ separation of supported ionic liquid membranes. *Phys. Chem. Chem. Phys.* **2017**, *19*, 28876-28884.
- (37) Tiwari, R. R.; Jin, J.; Freeman, B. D.; Paul, D. R. Physical aging, CO₂ sorption and plasticization in thin films of polymer with intrinsic microporosity (PIM-1). *J. Membrane Sci.* **2017**, *537*, 362-371.
- (38) Shin, J. Y.; Yamada, S. A.; Fayer, M. D. Carbon Dioxide in a Supported Ionic Liquid Membrane: Structural and Rotational Dynamics Measured with 2D IR and Pump-Probe Experiments. *J. Am. Chem. Soc.* **2017**, *139*, 11222-11232.
- (39) Cao, B.; Yan, W.; Wang, J.; Ding, H.; Yu, Y. Absorption of CO₂ with supported imidazolium-based ionic liquid membranes. *J. Chem. Technol. Biot.* **2015**, *90*, 1537-1544.
- (40) Noble, R. D.; Gin, D. L. Perspective on ionic liquids and ionic liquid membranes. *J. Membrane Sci.* **2011**, *369*, 1-4.
- (41) Wang, X.; Akhmedov, N. G.; Duan, Y.; Luebke, D.; Hopkinson, D.; Li, B. Amino acid-functionalized ionic liquid solid sorbents for post-combustion carbon capture. *ACS Appl. Mater. Inter.* **2013**, *5*, 8670-8677.
- (42) Mittenthal, M. S.; Flowers, B. S.; Bara, J. E.; Whitley, J. W.; Spear, S. K.; Roveda, J. D.; Wallace, D. A.; Shannon, M. S.; Holler, R.; Martens, R.; Daly, D. T. Ionic Polyimides: Hybrid Polymer Architectures and Composites with Ionic Liquids for Advanced Gas Separation Membranes. *Ind. Eng. Chem. Res.* **2017**, *56*, 5055-5069.
- (43) Bonakala, S.; Balasubramanian, S. Structure-Property Relationships in Amorphous Microporous Polymers. *J. Phys. Chem. B* **2016**, *120*, 557-565.
- (44) Abedini, A.; Crabtree, E.; Bara, J. E.; Turner, C. H. Molecular Simulation of Ionic Polyimides and Composites with Ionic Liquids as Gas-Separation Membranes. *Langmuir* **2017**, *33*, 11377-11389.
- (45) Morozova, S. M.; Shaplov, A. S.; Lozinskaya, E. I.; Mecerreyes, D.; Sardon, H.; Zulfiqar, S.; Suárez-García, F.; Vygodskii, Y. S. Ionic Polyurethanes as a New Family of Poly(ionic liquid)s for Efficient CO₂ Capture. *Macromolecules* **2017**, *50*, 2814-2824.
- (46) Qian, W.; Texter, J.; Yan, F. Frontiers in poly(ionic liquid)s: syntheses and applications. *Chem. Soc. Rev.* **2017**, *46*, 1124-1159.
- (47) Lu, X. Q.; Qiao, Y. Q.; He, J. R.; Pan, M.; Kang, B. S.; Su, C. Y. Triple-stranded helical and plywood-like arrays: Two uncommon framework isomers based on the common one-dimensional chain structures. *Cryst. Growth Des.* **2006**, *6*, 1910-1914.
- (48) Becke, A. D. Density-functional thermochemistry. III. The role of exact exchange. *J. Chem. Phys.* **1993**, *98*, 5648-5652.

- (49) Frisch, M. J.; Trucks, G. W.; Schlegel, H. B.; Scuseria, G. E.; Robb, M. A.; Cheeseman, J. R.; Scalmani, G.; Barone, V.; Mennucci, B.; Petersson, G. A.; Nakatsuji, H.; Caricato, M.; Li, X.; Hratchian, H. P.; Izmaylov, A. F.; Bloino, J.; Zheng, G.; Sonnenberg, J. L.; Hada, M.; Ehara, M.; Toyota, K.; Fukuda, R.; Hasegawa, J.; Ishida, M.; Nakajima, T.; Honda, Y.; Kitao, O.; Nakai, H.; Vreven, T.; Montgomery Jr., J. A.; Peralta, J. E.; Ogliaro, F.; Bearpark, M. J.; Heyd, J.; Brothers, E. N.; Kudin, K. N.; Staroverov, V. N.; Kobayashi, R.; Normand, J.; Raghavachari, K.; Rendell, A. P.; Burant, J. C.; Iyengar, S. S.; Tomasi, J.; Cossi, M.; Rega, N.; Millam, N. J.; Klene, M.; Knox, J. E.; Cross, J. B.; Bakken, V.; Adamo, C.; Jaramillo, J.; Gomperts, R.; Stratmann, R. E.; Yazyev, O.; Austin, A. J.; Cammi, R.; Pomelli, C.; Ochterski, J. W.; Martin, R. L.; Morokuma, K.; Zakrzewski, V. G.; Voth, G. A.; Salvador, P.; Dannenberg, J. J.; Dapprich, S.; Daniels, A. D.; Farkas, Ö.; Foresman, J. B.; Ortiz, J. V.; Cioslowski, J.; Fox, D. J.: Gaussian 09. Gaussian, Inc.: Wallingford, CT, USA, 2009.
- (50) Lopes, J. N. C.; Padua, A. A. H. Molecular force field for ionic liquids composed of triflate or bistriflylimide anions. *J. Phys. Chem. B* **2004**, *108*, 16893-16898.
- (51) Lopes, J. N. C.; Deschamps, J.; Padua, A. A. H. Modeling ionic liquids using a systematic all-atom force field. *J. Phys. Chem. B* **2004**, *108*, 2038-2047.
- (52) Resende Prado, C. E.; Gomide Freitas, L. C. Molecular dynamics simulation of the room-temperature ionic liquid 1-butyl-3-methylimidazolium tetrafluoroborate. *J. Mol. Struct-THEOCHEM* **2007**, *847*, 93-100.
- (53) Aparicio, S.; Alcalde, R.; Davila, M. J.; Garcia, B.; Leal, J. M. Measurements and predictive models for the N-methyl-2-pyrrolidone/water/methanol system. *J. Phys. Chem. B* **2008**, *112*, 11361-11373.
- (54) Potoff, J. J.; Siepmann, J. I. Vapor-liquid equilibria of mixtures containing alkanes, carbon dioxide, and nitrogen. *AIChE J.* **2001**, *47*, 1676-1682.
- (55) Trinh, T. T.; Vlugt, T. J.; Kjelstrup, S. Thermal conductivity of carbon dioxide from non-equilibrium molecular dynamics: a systematic study of several common force fields. *J. Chem. Phys.* **2014**, *141*, 134504-134507.
- (56) Budhathoki, S.; Shah, J. K.; Maginn, E. J. Molecular Simulation Study of the Solubility, Diffusivity and Permselectivity of Pure and Binary Mixtures of CO₂ and CH₄ in the Ionic Liquid 1-n-Butyl-3-methylimidazolium bis(trifluoromethylsulfonyl)imide. *Ind. Eng. Chem. Res.* **2015**, *54*, 8821-8828.
- (57) Turner, C. H.; Cooper, A.; Zhang, Z.; Shannon, M. S.; Bara, J. E. Molecular simulation of the thermophysical properties of N-functionalized alkylimidazoles. *J. Phys. Chem. B* **2012**, *116*, 6529-6535.
- (58) Martinez, L.; Andrade, R.; Birgin, E. G.; Martinez, J. M. PACKMOL: a package for building initial configurations for molecular dynamics simulations. *J. Comput. Chem.* **2009**, *30*, 2157-2164.
- (59) Theodorou, D. N.; Suter, U. W. Detailed Molecular-Structure of a Vinyl Polymer Glass. *Macromolecules* **1985**, *18*, 1467-1478.
- (60) Van Der Spoel, D.; Lindahl, E.; Hess, B.; Groenhof, G.; Mark, A. E.; Berendsen, H. J. GROMACS: fast, flexible, and free. *J. Comput. Chem.* **2005**, *26*, 1701-1718.
- (61) Essmann, U.; Perera, L.; Berkowitz, M. L.; Darden, T.; Lee, H.; Pedersen, L. G. A smooth particle mesh Ewald method. *J. Chem. Phys.* **1995**, *103*, 8577-8593.
- (62) Hoover, W. G. Canonical dynamics: Equilibrium phase-space distributions. *Phys. Rev. A* **1985**, *31*, 1695-1697.
- (63) Parrinello, M.; Rahman, A. Crystal Structure and Pair Potentials: A Molecular-Dynamics Study. *Phys. Rev. Lett.* **1980**, *45*, 1196-1199.

- (64) Shah, J. K.; Maginn, E. J. A general and efficient Monte Carlo method for sampling intramolecular degrees of freedom of branched and cyclic molecules. *J. Chem. Phys.* **2011**, *135*, 134121-134111.
- (65) Gelb, L. D.; Gubbins, K. E. Pore size distributions in porous glasses: A computer simulation study. *Langmuir* **1999**, *15*, 305-308.
- (66) Kupgan, G.; Liyana-Arachchi, T. P.; Colina, C. M. Pore size tuning of poly(styrene-co-vinylbenzyl chloride-co-divinylbenzene) hypercrosslinked polymers: Insights from molecular simulations. *Polymer* **2016**, *99*, 173-184.
- (67) Sarkisov, L.; Harrison, A. Computational structure characterisation tools in application to ordered and disordered porous materials. *Mol. Simulat.* **2011**, *37*, 1248-1257.
- (68) Madkour, T. M.; Mark, J. E. Molecular modeling investigation of the fundamental structural parameters of polymers of intrinsic microporosity for the design of tailor-made ultra-permeable and highly selective gas separation membranes. *J. Membrane Sci.* **2013**, *431*, 37-46.
- (69) Del Regno, A.; Gonciaruk, A.; Leay, L.; Carta, M.; Croad, M.; Malpass-Evans, R.; McKeown, N. B.; Siperstein, F. R. Polymers of Intrinsic Microporosity Containing Tröger Base for CO₂ Capture. *Ind. Eng. Chem. Res.* **2013**, *52*, 16939-16950.
- (70) Wood, C. D.; Tan, B.; Trewin, A.; Su, F.; Rosseinsky, M. J.; Bradshaw, D.; Sun, Y.; Zhou, L.; Cooper, A. I. Microporous Organic Polymers for Methane Storage. *Adv. Mater.* **2008**, *20*, 1916-1921.
- (71) Wood, C. D.; Tan, B.; Trewin, A.; Niu, H. J.; Bradshaw, D.; Rosseinsky, M. J.; Khimyak, Y. Z.; Campbell, N. L.; Kirk, R.; Stockel, E.; Cooper, A. I. Hydrogen storage in microporous hypercrosslinked organic polymer networks. *Chem. Mater.* **2007**, *19*, 2034-2048.
- (72) Bisoi, S.; Mandal, A. K.; Padmanabhan, V.; Banerjee, S. Aromatic polyamides containing trityl substituted triphenylamine: Gas transport properties and molecular dynamics simulations. *J. Membrane Sci.* **2017**, *522*, 77-90.
- (73) Espeso, J.; Lozano, A. E.; de la Campa, J. G.; de Abajo, J. Effect of substituents on the permeation properties of polyamide membranes. *J. Membrane Sci.* **2006**, *280*, 659-665.
- (74) Zhuang, Y.; Seong, J. G.; Do, Y. S.; Jo, H. J.; Lee, M. J.; Wang, G.; Guiver, M. D.; Lee, Y. M. Effect of Isomerism on Molecular Packing and Gas Transport Properties of Poly(benzoxazole-co-imide)s. *Macromolecules* **2014**, *47*, 7947-7957.
- (75) Weng, C.-J.; Jhuo, Y.-S.; Huang, K.-Y.; Feng, C.-F.; Yeh, J.-M.; Wei, Y.; Tsai, M.-H. Mechanically and Thermally Enhanced Intrinsically Dopable Polyimide Membrane with Advanced Gas Separation Capabilities. *Macromolecules* **2011**, *44*, 6067-6076.
- (76) Bara, J. E.; Carlisle, T. K.; Gabriel, C. J.; Camper, D.; Finotello, A.; Gin, D. L.; Noble, R. D. Guide to CO₂ Separations in Imidazolium-Based Room-Temperature Ionic Liquids. *Ind. Eng. Chem. Res.* **2009**, *48*, 2739-2751.
- (77) Budhathoki, S.; Shah, J. K.; Maginn, E. J. Molecular Simulation Study of the Solubility, Diffusivity and Permselectivity of Pure and Binary Mixtures of CO₂ and CH₄ in the Ionic Liquid 1-n-Butyl-3-methylimidazolium bis(trifluoromethylsulfonyl)imide. *Ind. Eng. Chem. Res.* **2015**, *54*, 8821-8828.
- (78) Tocci, E.; De Lorenzo, L.; Bernardo, P.; Clarizia, G.; Bazzarelli, F.; McKeown, N. B.; Carta, M.; Malpass-Evans, R.; Friess, K.; Pilnáček, K.; Lanč, M.; Yampolskii, Y. P.; Strarannikova, L.; Shantarovich, V.; Mauri, M.; Jansen, J. C. Molecular Modeling and Gas Permeation Properties of a Polymer of Intrinsic Microporosity Composed of Ethanoanthracene and Tröger's Base Units. *Macromolecules* **2014**, *47*, 7900-7916.

- (79) Tomé, L. C.; Gouveia, A. S. L.; Ab Rani, M. A.; Lickiss, P. D.; Welton, T.; Marrucho, I. M. Study on Gas Permeation and CO₂ Separation through Ionic Liquid-Based Membranes with Siloxane-Functionalized Cations. *Ind. Eng. Chem. Res.* **2017**, *56*, 2229-2239.
- (80) Almantariotis, D.; Gefflaut, T.; Padua, A. A. H.; Coxam, J. Y.; Gomes, M. F. C. Effect of Fluorination and Size of the Alkyl Side-Chain on the Solubility of Carbon Dioxide in 1-Alkyl-3-methylimidazolium Bis(trifluoromethylsulfonyl)amide Ionic Liquids. *J. Phys. Chem. B* **2010**, *114*, 3608-3617.
- (81) Koyuturk, B.; Altintas, C.; Kinik, F. P.; Keskin, S.; Uzun, A. Improving Gas Separation Performance of ZIF-8 by [BMIM][BF₄] Incorporation: Interactions and Their Consequences on Performance. *J. Phys. Chem. C* **2017**, *121*, 10370-10381.
- (82) Hart, K. E.; Colina, C. M. Ionomers of intrinsic microporosity: in silico development of ionic-functionalized gas-separation membranes. *Langmuir* **2014**, *30*, 12039-12048.
- (83) Hart, K. E.; Colina, C. M. Estimating gas permeability and permselectivity of microporous polymers. *J. Membrane Sci.* **2014**, *468*, 259-268.
- (84) Li, S.; Chung, Y. G.; Snurr, R. Q. High-Throughput Screening of Metal-Organic Frameworks for CO₂ Capture in the Presence of Water. *Langmuir* **2016**, *32*, 10368-10376.
- (85) Gupta, K. M.; Chen, Y.; Hu, Z.; Jiang, J. Metal-organic framework supported ionic liquid membranes for CO₂ capture: anion effects. *Phys. Chem. Chem. Phys.* **2012**, *14*, 5785-5794.

5. SUMMARY

5.1 Bismuth telluride exfoliation

Bismuth telluride (Bi_2Te_3) is a well-known thermoelectric material with potential applications in several different emerging technologies. The bulk structure is composed of stacks of quintuple sheets (with weak interactions between neighboring sheets), and the performance of the material can be significantly enhanced if exfoliated into two-dimensional nanosheets. In this study, eight different imidazolium-based ionic liquids are evaluated as solvents for the exfoliation and dispersion of Bi_2Te_3 at temperatures ranging from 350 K to 550 K. Three distinct exfoliation mechanisms are evaluated (pulling, shearing, and peeling) using steered molecular dynamics simulations, and we predict that the peeling mechanism is thermodynamically the most favorable route. Furthermore, the $[\text{Tf}_2\text{N}^-]$ -based ionic liquids are particularly effective at enhancing the exfoliation, and this performance can be correlated to the unique molecular-level solvation structures developed at the Bi_2Te_3 surfaces. While there are some exceptions, the performance of the $[\text{Tf}_2\text{N}^-]$ -based ILs is ranked highest, while that of the $[\text{Cl}^-]$ -based ILs is ranked lowest, and we find that the molecular features of these two solvent systems are characteristically different. For instance, the $[\text{Tf}_2\text{N}^-]$ anion induces much more tilt in the $[\text{C}_4\text{mim}^+]$ species at the interface (versus a much more planar configuration when paired with the $[\text{Cl}^-]$ anion). In addition, the normalized number density indicates a much higher $[\text{Tf}_2\text{N}^-]$ packing density in the first anion layer at the interface (versus $[\text{Cl}^-]$). Two strong and separate charged layers of the $[\text{Tf}_2\text{N}^-]$ -based ionic liquids with strong positive followed by a negative charges was evaluated at the surface of the Bi_2Te_3 . This information helps provide insight into

the molecular origins of exfoliation and solvation involving Bi_2Te_3 (and possibly other layered chalcogenide materials such as: $(\text{Bi,Sb})_2(\text{Te,Se})_3$, $\text{Pb}(\text{Te,Se,S})$, PbTe-AgSbTe_2 , and GeTe-AgSbTe_2) and ionic liquid solvents.

5.2 CO_2 capture

Polyimides are at the forefront of advanced membrane materials for CO_2 capture and gas purification processes. Recently, “ionic polyimides” (i-IPs) have been reported as a new class of condensation polymers, which combine structural components of both ionic liquids (ILs) and polyimides through covalent linkages. In this study, we report CO_2 and CH_4 adsorption and structural analyses of an i-IP and an i-IP + IL composite containing $[\text{C}_4\text{mim}][\text{Tf}_2\text{N}]$. The combination of molecular dynamics (MD) and grand canonical Monte Carlo (GCMC) simulations are used to compute the gas solubility and the adsorption performance with respect to the density, fractional free volume (FFV), and surface area of the materials. Our results highlight the polymer relaxation process, and its correlation to the gas solubility. In particular, the surface area can provide meaningful guidance with respect to the gas solubility, and it tends to be a more sensitive indicator of the adsorption behavior versus only considering the system density and FFV. For instance, as the polymer continues to relax, the density, FFV, and pore-size distribution remain constant, while the surface area can continue to increase, enabling more adsorption. Structural analyses are also conducted to identify the nature of the gas adsorption once the ionic liquid is added to the polymer. The presence of the IL significantly displaces the CO_2 molecules from the ligand nitrogen sites in the neat i-IP to the imidazolium rings in the i-IP + IL composite. Whereas, the CH_4 molecules move from the imidazolium ring sites in the neat i-IP to the ligand nitrogen atoms in the i-IP + IL composite. These molecular details can provide

critical information for the experimental design of highly selective i-IP materials, as well as provide additional guidance for the interpretation of the simulated adsorption systems.

The CO₂ separation characteristics of ionic polyimides (i-IPs) are modeled using molecular dynamics (MD) simulations in combination with grand canonical Monte Carlo (GCMC) calculations for typical pre-combustion and post-combustion conditions. The performance of both neat i-IP systems are evaluated, as well as composite structures containing both i-IPs and various ionic liquid (IL) solvents, ranging from 10 mol% to 50 mol% IL. The i-IP + IL composites are based on combinations of 1-n-butyl-3-methylimidazolium ([C₄mim⁺]) cation molecules with different anions: bis(trifluoromethylsulfonyl)imide ([Tf₂N⁻]), tetrafluoroborate ([BF₄⁻]), and hexafluorophosphate ([PF₆⁻]). It is found that the 50% IL addition can increase CO₂/CH₄ selectivity by 16% in [BF₄⁻]-based structure and by 36% in [PF₆⁻]-based for 5% of CO₂ in CO₂/CH₄ mixtures. While the [BF₄⁻]-based system shows higher CO₂/CH₄ selectivity, the [Tf₂N⁻]-based system shows higher CO₂/N₂ gas separation performance. A comprehensive structural analysis (fractional free volume, pore size distribution, surface area, etc.) is used to highlight the underlying differences among the different i-IP+IL systems that lead to the different adsorption properties. Structural modification has been explored during CO₂ adsorption, and a strong correlation between structural change and surface area was found. Additionally, high surface area correlates with a high probability of larger pore sizes. These findings are exemplified by high gas solubility of [PF₆⁻]-based structures with a larger surface area.

6. FUTURE WORK

Recent studies have brought forth interest into the development of a possible class of polymer material through combining IL and polyimide properties. Polyimides (PIs), ILs, and polymerized ionic liquids (PILs) have high potential in different industrial applications such as gas separation¹, packaging², sensors³⁻⁵, water treatment^{6,7}, electrolytes⁸, etc. Each of these applications faces some challenges; but there are potential solutions for each. Polyimides showed an outstanding heat resistance, good mechanical strength, as well as chemical resistance to many solvents.⁹ However, in gas separation applications of polyimides, increasing permeability while at the same time maintaining its high selectivity is a great challenge. Compatibility of physical mixing (with graphene oxide⁷) and chemically bonding to thermoelectric materials (graphite⁴) provides unique properties for polyimides to be applicable in water desalination and sensor applications, respectively. On the other hand, considering the high ion conductivity of ILs and PILs as well as potential polyimide applications as an electrolyte in lithium ion batteries⁸ open new possible applications for materials that have the benefits of both polyimide and IL structural features.

To start exploring this new class of polymers, in chapter 3 and 4, PMDA (**Figure 6.1**) was chosen to be used as an organic ligand in an i-IP structure. This organic ligand was used because of its low cost and ability to form a helical nanostructure in MOFs.¹⁰ The prepared neat polymer structure showed a lower gas solubility capacity in comparison to other porous solid materials¹¹⁻¹⁸; however, [BF₄⁻]-based i-IPs of this structure showed very high CO₂/CH₄ selectivity at 294 K and 1 bar. While keeping IL molecules in the backbone of the polymer

chain, a more bulky organic ligand with high disturbance in the polymer chain is the ultimately desired i-IP structure. In addition, a potential bulky organic ligand that can reduce the chain packing is hexafluoroisopropylidene-diphthalic anhydride (6-FDA). In **Figure 6.2** the 6-FDA structure and i-IP monomer composed of 6-FDA is represented. The 6-FDA-based polyimides showed high disturbance in polymer chain packing due to the CF₃ group.¹⁹ An i-IP prepared with imbedding 6-FDA ligands in the backbone could have a considerably higher chain stiffness and reduced the chain packing due to the CF₃ groups in the 6-FDA ligand. In addition, polymers with 6-FDA in the backbone showed an acceptable balance in high CO₂ permeability and CO₂/CH₄ selectivity.^{20,21} In gas separation application of the polymer, chain rigidity determines the permselectivity while the permeability is dominated by inter-chain spacing and chain mobility.¹⁹ It is difficult to increase the inter-chain spacing without losing the backbone stiffness due to the restricted rotation of the linkages in polyimide structures. Due to the increased flexibility of 6-FDA ligand, having imidazolium based ILs ([C₄mim⁺]-based structures) in the backbone of the polyimide to produce an ionic polyimide membrane could potentially produce high inter-chain spacing. Regarding our recent work in chapter 4, high surface area and large pore sizes were observed in [PF₆⁻]-based i-IP with a PMDA ligand. Solubility and solubility-selectivity are the desired factors in designing porous materials in gas separation, especially for CO₂ capturing. As demonstrated in chapter 3 and 4, [BF₄⁻]-based i-IPs with a PMDA ligand showed very high CO₂/CH₄ selectivity (150–300) with a noticeable enhancement in gas solubility in comparison to [Tf₂N⁻]-based i-IPs (62%). There are some disadvantages considering 6-FDA as a potential ligand in i-IP structure. In addition to their relatively high cost, 6-FDA-based polyimides have a tendency to undergo physical aging and plasticizing.²²⁻²⁴ During plasticization, the membrane permeability decreases with increasing pressure. Once passed this

threshold, called the plasticization pressure, the solubility coefficient and the permeability decreases.⁹ Physical aging is the common disadvantage of all polymers of intrinsic microporosity (PIMs). Their high free volume created by great backbone rigidity is considered as a driving force for the rapid physical aging of the polymer.²⁵ Cross-linking techniques in polymerization may be an effective method to produce PIMs that are more resilient against physical aging and plasticization.^{22,26} Gas separation performance of the cross-linked polymers need to be evaluated. The structural changes as well as gas solubility and selectivity enhancement are critical factors to evaluate the most desired polymer. Computational work along with experimental benchmarking provides a comprehensive analysis tool to design an efficient structure for gas separation.

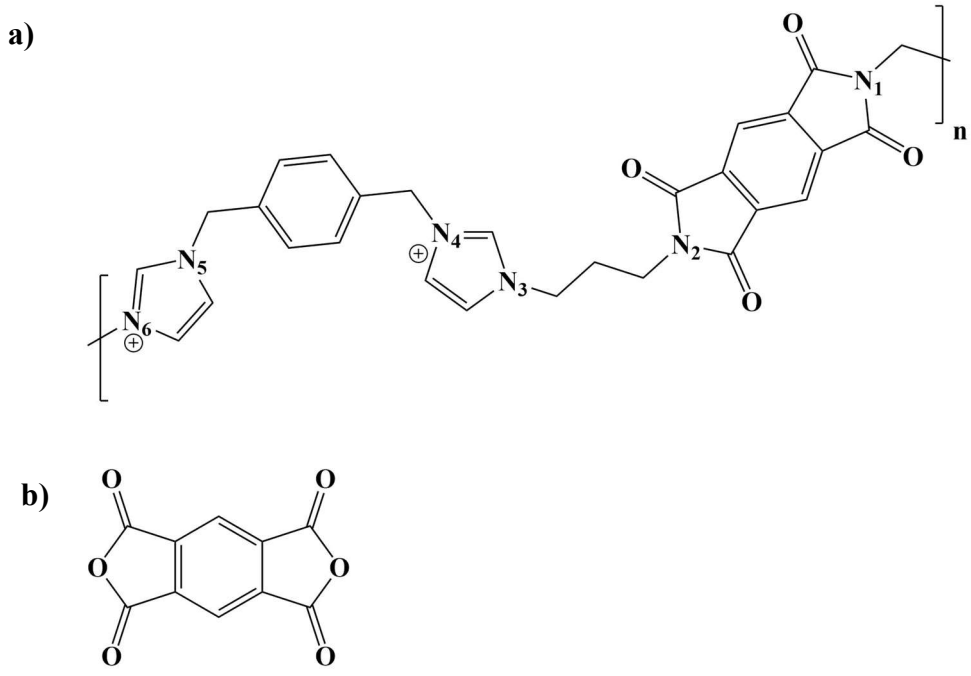


Figure 6.1. a) i-IP structure with PMDA ligand. b) PMDA molecule.

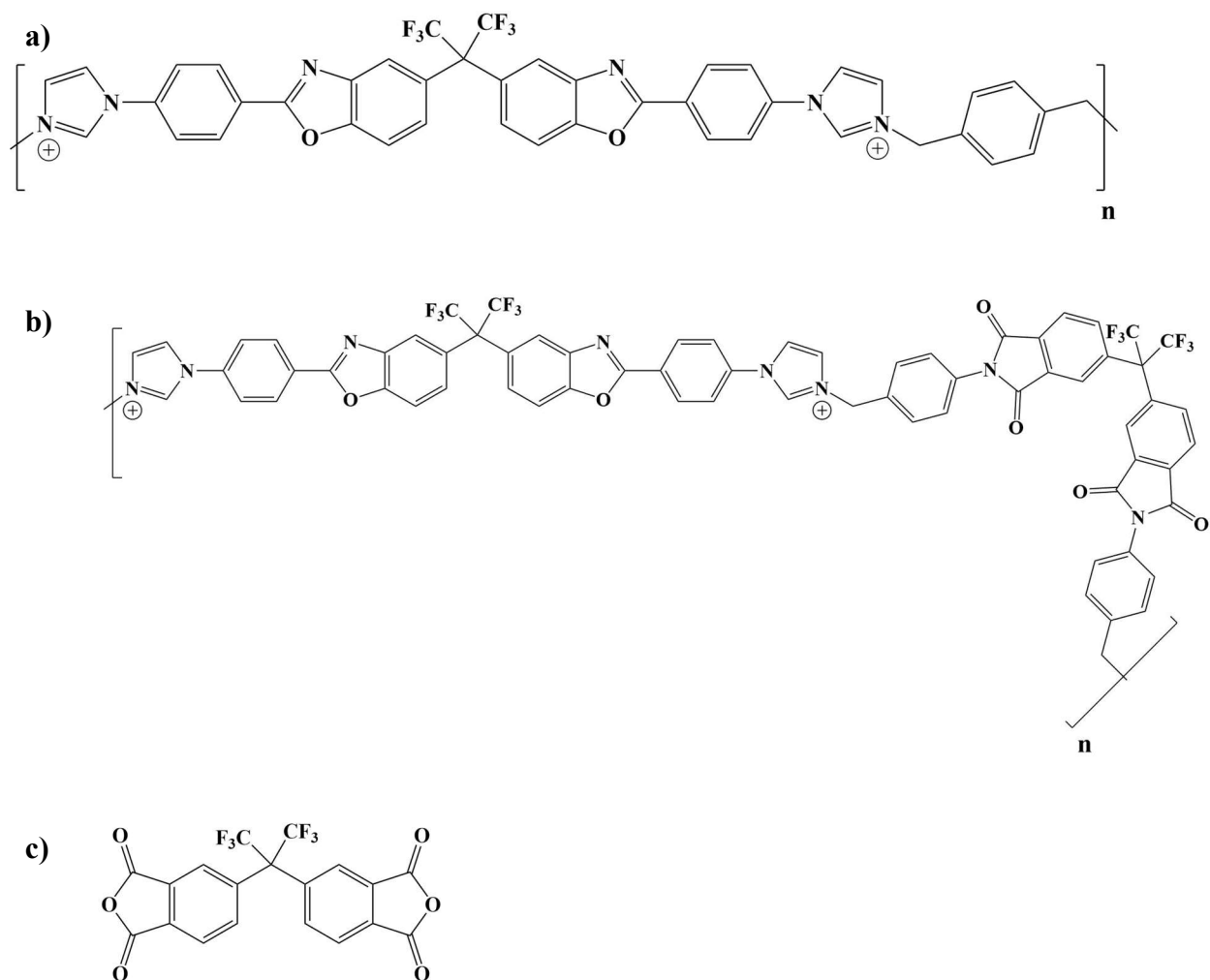


Figure 6.2. a) i-IP structure with 6-FDA ligand. b) the alternative i-IP structure with 6-FDA and c) the 6-FDA structure.

References

- (1) Wang, Z.; Wang, D.; Zhang, F.; Jin, J. Tröger's Base-Based Microporous Polyimide Membranes for High-Performance Gas Separation. *ACS Macro Lett.* **2014**, *3*, 597-601.
- (2) Liu, J.-J.; Tan, J.-H.; Zeng, Y.; Liu, Y.-W.; Zeng, K.-J.; Liu, Y.-J.; Wu, R.-M.; Chen, H. Synthesis and characterization of high-barrier polyimide containing rigid planar moieties and amide groups. *Polym. Test.* **2017**, *61*, 83-92.
- (3) Wang, D. H.; Lee, K. M.; Yu, Z.; Koerner, H.; Vaia, R. A.; White, T. J.; Tan, L.-S. Photomechanical Response of Glassy Azobenzene Polyimide Networks. *Macromolecules* **2011**, *44*, 3840-3846.
- (4) Tsai, M.-H.; Tseng, I. H.; Huang, Y.-C.; Yu, H.-P.; Chang, P.-Y. Transparent Polyimide Film with Improved Water and Oxygen Barrier Property by In-Situ Exfoliating Graphite *Adv. Eng. Mater.* **2016**, *18*, 582-590.
- (5) Chai, J.; Liu, Q.; Liu, J.; Zhang, D. Optical fiber sensors based on novel polyimide for humidity monitoring of building materials. *Opt. Fiber Technol.* **2018**, *41*, 40-47.
- (6) Zhang, Y.; Ou, H.; Liu, H.; Ke, Y.; Zhang, W.; Liao, G.; Wang, D. Polyimide-based carbon nanofibers: A versatile adsorbent for highly efficient removals of chlorophenols, dyes and antibiotics. *Colloids and Surfaces A: Physicochem. Eng.* **2018**, *537*, 92-101.
- (7) Huang, A.; Feng, B. Synthesis of novel graphene oxide-polyimide hollow fiber membranes for seawater desalination. *J. Membrane Sci.* **2018**, *548*, 59-65.
- (8) Lin, C.-E.; Zhang, H.; Song, Y.-Z.; Zhang, Y.; Yuan, J.-J.; Zhu, B.-K. Carboxylated polyimide separator with excellent lithium ion transport properties for a high-power density lithium-ion battery. *J. Mater. Chem. A* **2018**, *6*, 991-998.
- (9) Vanherck, K.; Koeckelberghs, G.; Vankelecom, I. F. J. Crosslinking polyimides for membrane applications: A review. *Prog. Polym. Sci.* **2013**, *38*, 874-896.
- (10) Lu, X. Q.; Qiao, Y. Q.; He, J. R.; Pan, M.; Kang, B. S.; Su, C. Y. Triple-stranded helical and plywood-like arrays: Two uncommon framework isomers based on the common one-dimensional chain structures. *Cryst. Growth Des.* **2006**, *6*, 1910-1914.
- (11) Koyuturk, B.; Altintas, C.; Kinik, F. P.; Keskin, S.; Uzun, A. Improving Gas Separation Performance of ZIF-8 by [BMIM][BF₄] Incorporation: Interactions and Their Consequences on Performance. *J. Phys. Chem. C* **2017**, *121*, 10370-10381.
- (12) Sezginel, K. B.; Keskin, S.; Uzun, A. Tuning the Gas Separation Performance of CuBTC by Ionic Liquid Incorporation. *Langmuir* **2016**, *32*, 1139-1147.
- (13) Bonakala, S.; Balasubramanian, S. Structure-Property Relationships in Amorphous Microporous Polymers. *J. Phys. Chem. B* **2016**, *120*, 557-565.
- (14) Hart, K. E.; Colina, C. M. Ionomers of intrinsic microporosity: in silico development of ionic-functionalized gas-separation membranes. *Langmuir* **2014**, *30*, 12039-12048.
- (15) Hart, K. E.; Colina, C. M. Estimating gas permeability and permselectivity of microporous polymers. *J. Membrane Sci.* **2014**, *468*, 259-268.
- (16) Li, S.; Chung, Y. G.; Snurr, R. Q. High-Throughput Screening of Metal-Organic Frameworks for CO₂ Capture in the Presence of Water. *Langmuir* **2016**, *32*, 10368-10376.
- (17) Vicent-Luna, J. M.; Luna-Triguero, A.; Calero, S. Storage and Separation of Carbon Dioxide and Methane in Hydrated Covalent Organic Frameworks. *J. Phys. Chem. C* **2016**, *120*, 23756-23762.

- (18) Gupta, K. M.; Chen, Y.; Hu, Z.; Jiang, J. Metal-organic framework supported ionic liquid membranes for CO₂ capture: anion effects. *Phys. Chem. Chem. Phys.* **2012**, *14*, 5785-5794.
- (19) Xiao, Y.; Low, B. T.; Hosseini, S. S.; Chung, T. S.; Paul, D. R. The strategies of molecular architecture and modification of polyimide-based membranes for CO₂ removal from natural gas—A review. *Prog. Polym. Sci.* **2009**, *34*, 561-580.
- (20) Cheng, S. X.; Chung, T. S.; Wang, R.; Vora, R. H. Gas-sorption properties of 6FDA-durene/1,4-phenylenediamine (pPDA) and 6FDA-durene/1,3-phenylenediamine (mPDA) copolyimides. *J. Appl. Polym. Sci.* **2003**, *90*, 2187-2193.
- (21) Liu, S. L.; Wang, R.; Chung, T. S.; Chng, M. L.; Liu, Y.; Vora, R. H. Effect of diamine composition on the gas transport properties in 6FDA-durene/3,3'-diaminodiphenyl sulfone copolyimides. *J. Membrane Sci.* **2002**, *202*, 165-176.
- (22) Sanders, D. F.; Smith, Z. P.; Guo, R.; Robeson, L. M.; McGrath, J. E.; Paul, D. R.; Freeman, B. D. Energy-efficient polymeric gas separation membranes for a sustainable future: A review. *Polymer* **2013**, *54*, 4729-4761.
- (23) Kim, J. H.; Koros, W. J.; Paul, D. R. Physical aging of thin 6FDA-based polyimide membranes containing carboxyl acid groups. Part I. Transport properties. *Polymer* **2006**, *47*, 3094-3103.
- (24) Wind, J. D.; Staudt-Bickel, C.; Paul, D. R.; Koros, W. J. Solid-state covalent cross-linking of polyimide membranes for carbon dioxide plasticization reduction. *Macromolecules* **2003**, *36*, 1882-1888.
- (25) Swaidan, R.; Ghanem, B.; Litwiller, E.; Pinnau, I. Physical Aging, Plasticization and Their Effects on Gas Permeation in “Rigid” Polymers of Intrinsic Microporosity. *Macromolecules* **2015**, *48*, 6553-6561.
- (26) Wind, J. D.; Staudt-Bickel, C.; Paul, D. R.; Koros, W. J. The effects of crosslinking chemistry on CO₂ plasticization of polyimide gas separation membranes. *Ind. Eng. Chem. Res.* **2002**, *41*, 6139-6148.